Numerical Modelling of Turbulent Mixing in Connected Nuclear Fuel Subchannels

NUMERICAL MODELLING OF TURBULENT MIXING IN CONNECTED NUCLEAR FUEL SUBCHANNELS

BY

MATTHEW BALLYK, B.Eng.

A THESIS

SUBMITTED TO THE DEPARTMENT OF MECHANICAL ENGINEERING

AND THE SCHOOL OF GRADUATE STUDIES

OF MCMASTER UNIVERSITY

IN PARTIAL FULFILMENT OF THE REQUIREMENTS

FOR THE DEGREE OF

MASTER OF APPLIED SCIENCE

Master of Applied Science (2018) McMaster University

(Mechanical Engineering) Hamilton, Ontario, Canada

TITLE:	Numerical Modelling of Turbulent Mixing in Connected Nuclear Fuel Subchannels
AUTHOR:	Matthew Ballyk B.Eng., (Engineering Physics) McMaster University, Hamilton, Canada
SUPERVISOR:	Dr. M.F. Lightstone, Dr. S. Tullis
NUMBER OF PAGES:	xxi, 151

To my parents

To those who helped along the way

Lay Abstract

The fuel bundle and pressure tube assembly in the core of a CANDU reactor forms an intricate web of subchannels of varying geometries with interconnecting gaps. Heat generated within the fuel bundles is removed by coolant flowing through the pressure tube and within the bundle subchannels. Although flow is nominally axial along the length of the rod bundles, coolant is free to move between subchannels through the gaps by a variety of mechanisms. Detailed fluid flow in these rod bundle geometries is a complex 3D phenomenon, strongly affected by fluid turbulence and flow instabilities associated with the subchannel geometry. This flow is investigated in the current study and extended to include the effect of appendages, which hold the fuel rods in place, to determine their impact on mixing along the length of the bundle.

Particular applications of the results of this study are in the areas of nuclear reactor performance and safety. The extent of coolant exchange between subchannels affects the local subchannel flow and temperature and, as a result, local cooling at the fuel element surfaces. Fuel element cooling is a principal component of reactor analysis under both normal operating conditions and postulated accident scenarios.

Abstract

The effects of appendages on flow characteristics and scalar mixing in gap-connected twin-subchannel geometries has been assessed. The assessment considers a symmetric, rectangular compound channel geometry connected by a single rectangular gap using computational fluid dynamics (CFD). Detailed numerical models (geometry and turbulence), characterizing the full test section from a reference experimental study, are generated and validated against measurements. Time varying details of the gap induced periodic structures and appendage induced vortices are captured through calculations in an unsteady Reynolds averaged Navier-Stokes (RANS) framework coupled with the Spalart-Allmaras (SA) turbulence model closing the RANS equations. Companion simulations are performed at each of two Reynolds numbers (2690 and 7500), one with and one without a gap-centered appendage. The appendage size modelled is representative of CANDU end plates. The appendage effects on flow characteristics and mixing are isolated through comparison of the associated simulations.

In the absence of appendages, fluid exchange between subchannels is dominated by quasi-periodic flow pulsations through the gap formed due to flow instability in the near gap region. Without a gap-centered appendage, the magnitude, frequency, and structure length of the gap flow pulsations are well predicted by the model at both Reynolds numbers. The total tracer transfer between subchannels is reasonably well

predicted for Re = 2690 (within approximately 17% of the experimental value). The model fails to capture the measured increase in scalar transfer through the gap with increased Reynolds number, underpredicting scalar mixing by 55% at Re = 7500. An argument is presented that the use of an isotropic turbulence model in the channel (SA), which precludes the development of channel secondary flows, is the source of the discrepancy between modelled and measured mixing at Re = 7500.

Appendages, such as those introduced by end plates or bearing pads in CANDU fuel bundles, augment the exchange process between subchannels. With an appendage representative of a CANDU fuel bundle end plate introduced into the gap region, crossflow velocity and frequency are predicted to increase immediately downstream of the appendage due to flow diversion and vortex shedding. The higher local frequency is shown to be consistent with the vortex shedding frequency calculated for a stationary rectangular cylinder at the gap conditions. Further downstream, gap induced instabilities begin to re-establish as the dominant contributor to crossflow pulsations although they are not fully recovered by the test section exit. Mixing is augmented more by the appendage with increasing Reynolds number for the range examined.

Acknowledgements

I would like to thank and express my appreciation for my supervisors, Dr. Marilyn Lightstone and Dr. Stephen Tullis, for both their guidance and support throughout the program. I would like to also extend my thanks and acknowledge the financial support of Mitacs through the Mitacs Accelerate Graduate Research Program, Candu Energy, and SNC-Lavilin Nuclear.

Nomenclature

A: flow area [m^2]

C: subchannel scalar concentration

D: rod diameter [m]; gap depth [m]; Strouhal number characteristic length [m]

D_h: hydraulic diameter [m]

f: frequency [Hz]

h: square duct height

k: turbulence kinetic energy $\left[\frac{J}{kg}\right]$

L: domain length [m]

P: rod pitch [m]

p: pressure $[Pa]$

p': pressure fluctuation $[Pa]$

$\overline{p}$: time mean pressure $[Pa]$

Re: Reynolds number

Re_τ: shear velocity based Reynolds number

S: gap spacing [m]

Sc: Schmidt number

Sc_t: turbulent Schmidt number

St: Strouhal number

S_ϕ: source term accounting for production and/or consumption of the species

U: velocity vector $\left[\frac{m}{s}\right]$

u: instantaneous velocity $\left[\frac{m}{s}\right]$

$\overline{u}$: time mean velocity $\left[\frac{m}{s}\right]$

u': velocity fluctuation $\left[\frac{m}{s}\right]$

U_b: bulk velocity $\left[\frac{m}{s}\right]$

u_e: gap edge velocity $\left[\frac{m}{s}\right]$

u_τ: friction or average shear velocity $\left[\frac{m}{s}\right]$

V: volume [m^3]

W: distance between rod and channel wall plus rod diameter [m]

x: spanwise direction [m]

y: streamwise (axial) direction [m]

y^+: dimensionless distance from wall $\left[\frac{yu_\tau}{v}\right]$

z: wall-normal (transverse) direction [m]

Greek Symbols

ϕ: transported scalar

Γ_ϕ: diffusion coefficient for scalar, ϕ

$\Gamma_{\phi t}$: turbulent or eddy diffusivity for scalar, ϕ

ε: turbulent dissipation rate $\left[\frac{W}{kg}\right]$

θ: scalar transfer through the gap

κ: von Kármán constant constant

μ: dynamic viscosity $[Pa{\cdot}s]$ [kg/m·s]

μ_τ: turbulent dynamic viscosity $[Pa{\cdot}s]$ [kg/m·s]

ν: kinematic viscosity $\left[\frac{m^2}{s}\right]$

ν_t: turbulent kinematic viscosity $\left[\frac{m^2}{s}\right]$

ρ: density $\left[\frac{kg}{m^3}\right]$

$\delta_{i,j}$: Kronecker delta function

ε: dissipation rate of k $\left[\frac{W}{kg}\right]$

ω: specific turbulence dissipation rate, $\left[\frac{\varepsilon}{k}\right]$ $\left[\frac{1}{s}\right]$

τ: Shear stress [N/m^2]

Abbreviations

ASSERT-PV: Advanced Solution of Subchannel Equations in Reactor Thermalhydraulics, Pressure-Velocity

BSL: Baseline

CANDU: Canadian Deuterium Uranium

CFD: Computational Fluid Dynamics

DES: Detached Eddy Simulation

DNS: Direct Numerical Simulation

DSM: Dynamic Smagorinsky Model

EARSM: Explicit Algebraic Reynolds Stress Model

FFT: Fast Fourier Transform

LBM: Lattice Boltzmann Method

LDV: Laser-Doppler Velocimetry

LES: Large Eddy Simulation

LHS: Left Hand Side

LWR: Light-Water Reactor

PDE: Partial Differential Equation

PIV: Particle Image Velocimetry

RANS: Reynolds Averaged Navier-Stokes

RHS: Right Hand Side

RKE: Realizable k-ε Model

RMS: Root Mean Square

RNG: Renormalization Group Method

RSM: Reynolds Stress Model

SA: Spalart-Allmaras

SSG: Speziale-Sarkar-Gatski

SST: Shear Stress Transport

SZL: Shih Zhu Lumley model

Contents

List of Tables

List of Figures

Chapter 1

Introduction

1.1 Background and Motivation

Fuel bundles in a CANDU nuclear reactor are made up of an array of cylindrical fuel rods held in place by end plates and spacer pads. The fuel bundles are contained within pressure tubes in the reactor core as shown in Figure 1.1.

The fuel bundle and pressure tube assembly form an intricate web of subchannels of varying geometry with interconnecting gaps as shown in Figure 1.2. Heat generated within the fuel bundles is removed by coolant flowing through the pressure tube and within the bundle subchannels. Although flow is nominally in the axial direction along the length of the rod bundles, the coolant is free to move between subchannels through the gaps by a variety of mechanisms. Detailed fluid flow and heat transfer in these rod bundle geometries is a complex 3D phenomenon as a result of the effects of fluid turbulence, flow instabilities arising from the gap/subchannel geometry, and appendages such as end plates and spacers pads.

In the current work, a computational fluid dynamics (CFD) study on turbulent

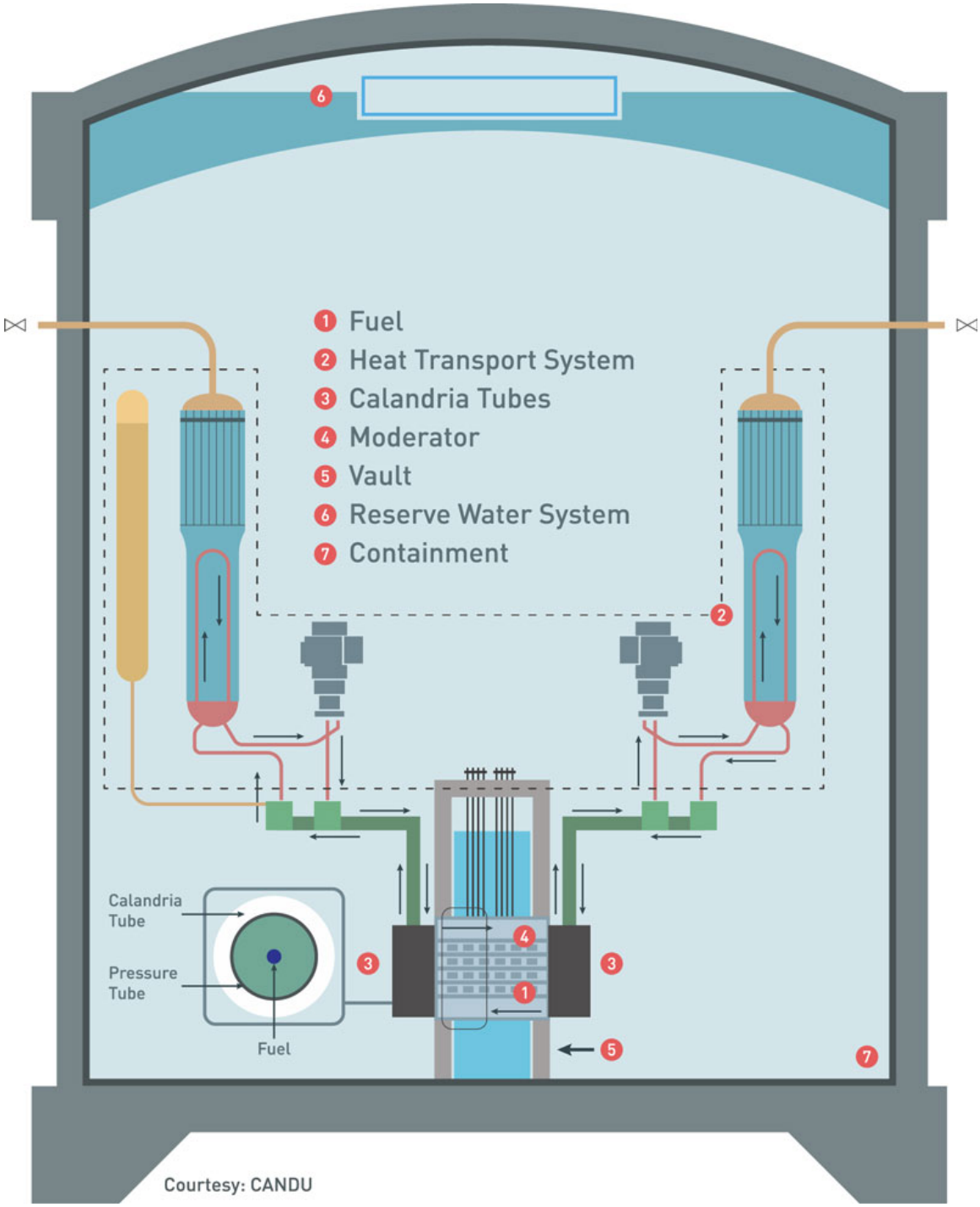

Figure 1.1: Overall CANDU plant flow schematic [4]

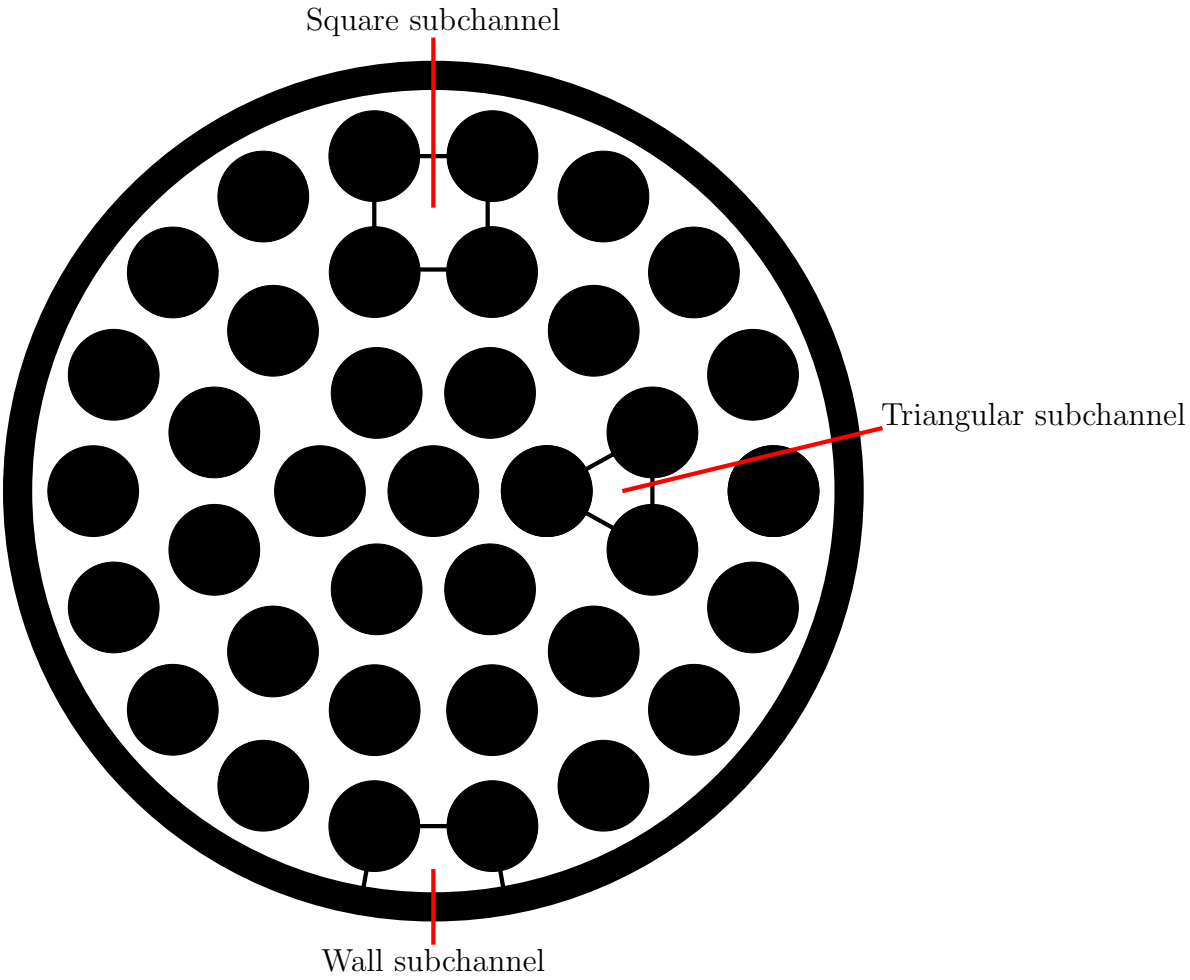

Figure 1.2: 37-element CANDU fuel bundle and subchannel cross section

mixing in a gap-connected twin-subchannel geometry has been carried out. Results from an experimental study were used as the foundation for validating the CFD models. The reference experimental study included measurements of flow velocities through the gap as well as total mixing along the length of a twin-subchannel test section. Consistent with the reference experimental procedure, the CFD modelling of mixing was carried out through the use of a tracer added to the flow.

Previous work on twin-subchannel geometries, in the absence of appendages, has shown that complex quasi-periodic structures are formed due to the flow instability in the near gap region. These flow structures contribute significantly to mixing between subchannels. The effects of appendages in the subchannel flow path have not been broadly studied in the literature. The current study extends the numerical modelling to investigate the effects of appendages in the gap region on mixing characteristics within twin-subchannel geometries.

Particular applications of the results of this study are in the areas of nuclear reactor performance and safety. The extent of coolant exchange between subchannels affects the local subchannel flow and temperature and, as a result, local cooling at the fuel element surfaces. Fuel element cooling is a principal component of reactor analysis under both normal operating conditions and postulated accident scenarios.

1.2 Problem Statement

Predicting fuel element cooling under accident or normal operating conditions relies on accurate modelling of the heat transfer and fluid flow within the fuel rod bundle geometries. Numerical methods applying CFD, when used with an appropriate turbulence model, can provide sufficiently fine resolution of the fluid flow and heat transfer

within a specified geometry and are capable of predicting the flow and heat transfer characteristics. However, these methods require significant computational effort due to the complex geometries of the rod bundles and their appendages coupled with the fine mesh resolutions required to capture the flow details.

Since CFD methods are impractical for broad application in reactor analysis, subchannel methods (such as those used in ASSERT-PV) are often employed. With these methods, fluid properties and the governing equations for heat transfer and fluid flow are integrated over a subchannel and averaged quantities are determined. As a result of this spatial averaging, the fine structures of the flow are not resolved. This approach therefore requires many empirical correlations to represent the complex exchange mechanisms (of mass, momentum and energy) between the subchannels. CFD is a valuable tool for studying these complex flows in rod bundle geometries and for subsequently developing physics-based empirical correlations for use in subchannel codes as well as for code validation.

1.3 Research Objectives

A numerical study of the effects of appendages on subchannel mixing has been carried out. Appendages such those introduced by end plate or bearing pad type obstructions are studied (see Figure 1.3). The assessment considers a simple rectangular compound channel geometry connected by a single gap through the use of CFD. The numerical analysis uses ANSYS CFX, a commercial CFD code, to predict mixing both in the absence and presence of appendages to isolate the effect on the resultant bulk crossflow mixing.

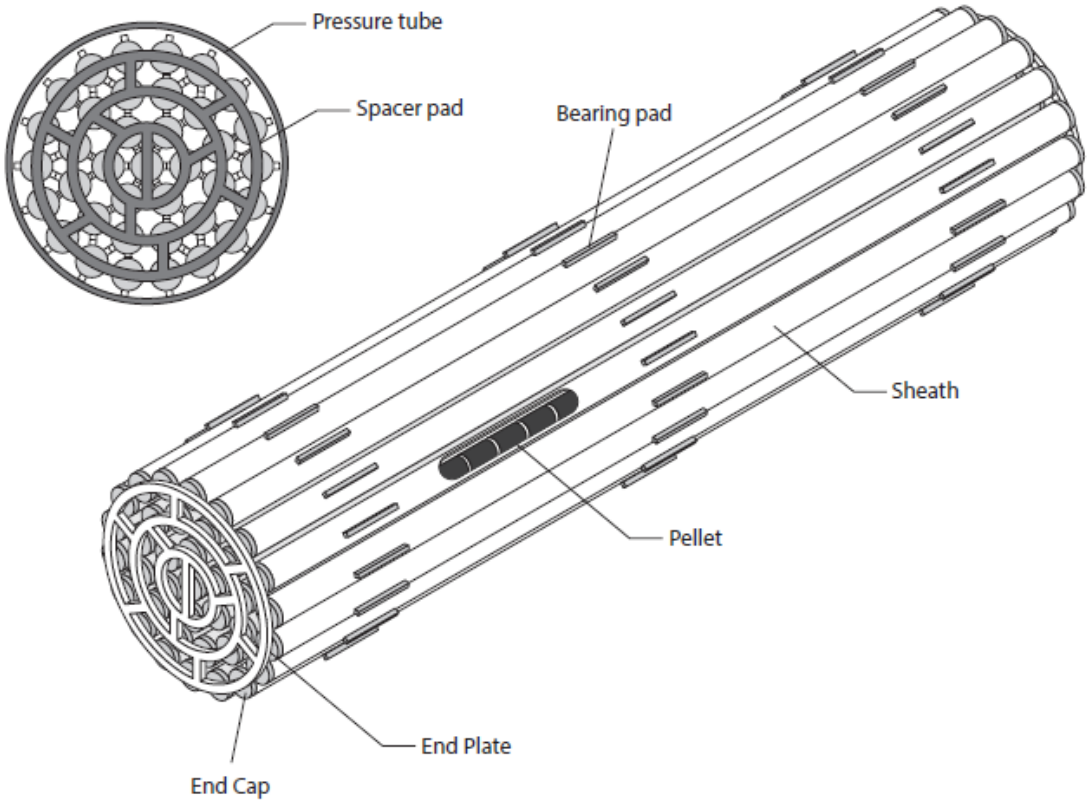

Figure 1.3: Appendages in a CANDU fuel bundle [5]

The CFD based study was developed through consultation with industry professionals at the partner organization's site (Candu Energy). Simulations were performed based on a reference experimental investigation that was used for model validation.

The results of the study provide previously unavailable details of flow structures in subchannel geometries relevant to CANDU reactors particularly under the influence of appendages in the flow field. The research results can be extended and subsequently used to develop physics-based empirical models to predict mixing characteristics in subchannel geometries representative of a nuclear reactor fuel channel. The extended research results can also be used to enhance the modelling and validation base for subchannel computer codes used in reactor analysis (e.g., ASSERT-PV).

1.4 Thesis Structure

This work is presented in six chapters. Chapter 2 presents an overview of previous related research and background information that has informed the current study. The theory and mathematical modelling forming the basis for the calculations are outlined in Chapter 3. Chapter 4 describes the overall methodology, assumptions and modelling details applied in the research program. This includes a description of the reference experimental studies [2], [3] used to define the selected set of CFD simulations in regards to geometry and boundary conditions. An analysis of the computational results is presented in Chapter 5. Chapter 6 draws conclusions based on these results and provides suggestions for further study.

Chapter 2

Literature Review

2.1 Overview

Inter-subchannel mixing in turbulent flow is a complex phenomenon with characteristics influenced by a large number of parameters including Reynolds number, physical geometry and boundary conditions. Due to its complex nature and broad range of applications, a significant amount of research effort has been devoted to inter-subchannel mixing over many years. These research programs have included a variety of experimental as well as numerical studies related to mixing and associated phenomena.

Simultaneous communication between multiple interconnected subchannels is encountered in many engineering applications. A particular case of interest is the flow within the intricate array of subchannels formed by the fuel rods in a CANDU fuel channel as discussed in Chapter 1. Although many studies have involved various rod-based multiple subchannel geometries, a large body of work has also been devoted to pairs of subchannels connected by way of a single gap, typically under fully

developed conditions. It is anticipated that the dominant mechanisms influencing fluid exchange between subchannels can be extracted and characterized from these fundamental studies. The more complex geometries and flow conditions that are encountered in practice can then be analyzed with the understanding derived from these fundamental studies.

2.2 Early Observations

Mass exchange through the gap between inter-connected subchannels occurs by a variety of mechanisms as identified, reassessed and confirmed in numerous studies over several decades. Understanding of the dominant contributors to inter-subchannel mixing has been evolutionary. An early study by Rowe and Angle (1967) [6] considered experimentally a pair of electrically heated subchannels connected by a single gap carrying water under both single-phase and two-phase conditions. Varying boundary conditions of mass flow rate and wall heat flux were considered for two values of simulated rod spacings. A correlation of the experimental data showed that the turbulent crossflow per unit length is independent of rod spacing and is nearly proportional to hydraulic diameter and mass velocity (i.e., Reynolds number). They also point out that actual rod bundles will have higher levels of mixing compared to the experiments due to the presence of rod spacing devices (e.g., end plates and bearing pads).

It was noted early on by several investigators that standard isotropic turbulent diffusion models in isolation could not account for experimentally measured levels of mass transfer through the gap. Skinner et al. (1969) [7] experimentally investigated mixing in two 6-rod clusters (one smooth, one roughened) using a nitrous oxide tracer in air as the working fluid at various Reynolds numbers. They demonstrate

that known correlations for isotropic turbulent diffusion under-predict the measured effective diffusivity in the gap region. Skinner attributes the higher effective diffusivity to secondary flows and shows that a simple secondary flow model with a magnitude of approximately 2% of the centerline velocity results in good agreement with his mixing measurements.

It should be noted that Ingesson and Kjellstrom (1970) [8] point out in response to the paper by Skinner et. al (1969) [7] that the higher mixing rates can also be obtained with a turbulent diffusion model provided a much smaller effective mixing length than the distance between the subchannels is applied. This is in effect applying a steeper scalar or temperature gradient in the model.

Van der Ros and Bogaardt (1970) [9] studied single-phase liquid flow in twin rectangular subchannels with varying gap geometries. The working fluid was water at Reynolds numbers between 5,000 and 30,000. One subchannel was electrically heated thereby imposing a temperature gradient across the gap. The overall mixing is calculated from the enthalpy increase through the non-heated channel. They too report that the transport mechanism for mass and heat exchange through the gap cannot be explained by eddy diffusivity alone. They also noted that thermocouple readings as well as visual observation indicate waves of regular amplitude and frequency for locations inside the gap region. This observation is among the earliest evidence of large-scale periodic structures through the gap.

Ramm et al. (1974) [10] presented a theoretical analysis of molecular and turbulent transport phenomena between subchannels in infinite triangular and square arrays. They extended the theoretical approach of Ramm and Johannsen (1972) [11] for predicting turbulent momentum and heat transfer in rod bundles to evaluate

three-dimensional temperature fields. By comparing with experimental results from earlier investigations, they noted appreciable deviations between calculated and experimentally measured mixing flowrates, often an order of magnitude or more. For fully turbulent flow, they attribute this difference to secondary flow effects which are not considered in their calculations. They declare that subchannel correlations existing at the time were successful in interpolating between existing data because of compensating errors. That is, they contain artificially high transverse eddy diffusivity, which compensate for neglect of secondary flows. At laminar and transition flows, they express concern over the integrity of the experimental data declaring the experimental results suspect, resulting in the discrepancies noted.

2.3 Secondary Flows

The persistent experimental evidence that standard isotropic turbulent diffusion models were incapable of capturing the measured level of mass transfer through the gap had researchers considering adjunct processes that could augment inter-subchannel mixing. One such process that appeared promising at the time was the contribution of secondary flows. Secondary flows manifest as motions in a plane perpendicular to the streamwise flow. For turbulent flows in non-circular ducts, this rotation is generated by the non-uniformity of turbulent stresses through the cross-section. These are known as secondary flows of Prandtl's second kind.

One of the earliest experimental observations attributed to secondary flows in rod bundle geometries was recorded by Tachibana et al. (1969) [12]. A mass transfer technique (Naphthalene sublimation) was applied in determining transport coefficients. Near sinusoidal variations in measured heat transfer coefficient around the center rod

of a seven-rod cluster were observed and attributed to the existence of secondary flows. These were deemed to be important for heat transfer calculations. There was no attempt to quantify the magnitude of secondary flows.

Rowe et al. (1974) [13] carried out an experimental investigation of the effect of flow channel geometry on fully developed turbulent flow in rod bundles arranged in a square array. The experiments were performed in water at Reynolds numbers ranging from 50,000 to 200,000 with pitch-to-diameter (P/D) ratios of 1.125 and 1.25. They showed that decreasing the rod gap spacing resulted in increased turbulence intensity and the dominant frequency of turbulence. Autocorrelations and laser Doppler measurements suggest the presence of significant periodic flow pulsations in the region between the gap and the subchannel center for the smaller pitch-to-diameter ratio (1.125). They conclude that a reduction of rod gap spacing leads to more dominant periodic flow pulsations in the regions adjacent to the rod gap. This, together with secondary flows, increased turbulence intensity and increased longitudinal macroscale, indicate an enhancement of crossflow mixing to help compensate for a decrease in rod gap spacing.

Trupp and Azad (1975) [14] carried out wind tunnel experiments on triangular array rod bundles. Three pitch-to-diameter ratios (1.20, 1.35 and 1.50) were considered over a range of Reynolds numbers (12,000 to 84,000). Data collected included friction factors, local wall shear stresses, the distributions of mean axial velocity, Reynolds stresses and eddy diffusivities. The authors declare secondary flows to be an important factor in inter-subchannel mixing. They infer the existence of secondary flows based on discrepancies noted between measured wall shear stresses and calculations assuming isotropic turbulent diffusivity (thereby neglecting secondary flows).

Although secondary flows could not be directly measured, they were estimated to be less than 0.5% of bulk flow.

Direct measurements of secondary flow velocity were made by Aly et. al (1978) [15] in an open equilateral triangular duct at Reynolds numbers of 53,000, 81,100 and 107,300. The observed secondary flow pattern consists of six counter-rotating cells bounded by the corner bisectors. The maximum secondary velocity measured was about 1.5% of the bulk velocity.

Seale (1979, Part 1) [16] performed wind tunnel experiments investigating mixing between subchannels defined by regularly spaced, single rows of smooth rods enclosed in a horizontally mounted rectangular duct. Measurements were made over a range of Reynolds numbers (approximately 30,000 to 300,000) and pitch-to-diameter ratios of 1.1, 1.375 and 1.833. Measurements confirmed that subchannel mixing rates are considerably higher than predicted by simple turbulent diffusion theory and are relatively insensitive to gap width. The effective diffusivities through the gap are shown to be strongly anisotropic with anisotropy increasing as the gap width decreases.

In a companion publication, Seale (1979, Part2) [17], the author applied the isotropic k-ε turbulence model in calculations to predict the turbulent flow and mixing in models representing the experiments from Seale (1979, Part 1) [16]. The isotropic model produced mixing results up to an order less than measured experimentally. Agreement improved with the more open aspect ratio geometry. The effects of anisotropy were investigated by grafting anisotropy factors onto the computational procedures which augmented the diffusivity in the direction parallel to the wall. To obtain mixing results of the correct order, it was necessary to apply anisotropic effective diffusivities that rose sharply near the walls to very high values. It is concluded

that secondary flows do not play a major role in mixing through the gap.

Seale (1982) [18] performed experiments using air in a duct representing two interconnected subchannels of a rod bundle at a pitch-to-diameter ratio of 1.2. Measurements were made, using pitot tubes and hot wire anemometry, of mean axial-velocity distribution, Reynolds stresses and secondary velocities at a Reynolds number of 200,000. The maximum secondary flow velocities reached in the cells circulating in the square corners of the duct were 1.5% of the bulk axial velocity.

Vonka published a pair of companion documents (1988a [19] and 1988b [20]) examining secondary flows in rod bundles. In Vonka (1988a) [19], laser Doppler velocimetry is used to measure secondary flow velocities in triangular array rod bundles (P/D = 1.3) for Reynolds numbers of 60,000 and 175,000. The average measured tangential secondary velocity was slightly less than 0.1% of the mean bulk velocity. In spite of the secondary vortices being extremely weak, it was concluded that they can contribute to transport processes, primarily within the subchannel as opposed to between subchannels. This conclusion was analysed quantitatively and found to be supported in Vonka (1988b) [20].

2.4 Periodic Flow Pulsations Through the Gap

Secondary flows were identified experimentally and assessed quantitatively for a variety of turbulent subchannel geometries and flow conditions. Attempts to exclusively attribute the enhanced inter-subchannel mixing beyond that associated with isotropic turbulent diffusion to secondary flows were generally unsuccessful. As studies progressed, clear evidence of large scale periodic pulsations through subchannel gaps began to emerge. These pulsations were recognised as a transport process capable of

Table 2.1: Experimental investigations - early and secondary flow observations

Investigator(s)	Geometry	Working Fluid	Reynolds Number	Measured Data	Methodology
Skinner, Freeman, and Lyall (1969)	Six rod cluster	Air	20,000 - 90,000	Velocity, pressure, tracer concentrations	Pitot-static probes, Nitrous oxide tracer
Tachibana, Oyama, Akiyama, and Kondo (1969)	Seven rod cluster (P/D = 1.125)	Air	7,500 - 45,000	Heat transfer factors	Mass transfer (naphthalene sublimation)
Van der Ros and Bogaardt (1970)	Two square channels separated by a gap	Air	5,000 - 30,000	Velocity, pressure, temperature	Pitot tubes, manometer, thermocouples
Ramm, Johannsen, and Todreas (1974)	Triangular and square rod arrays (P/D = 1.05 - 1.30)	Air	28,800 - 104, 800	Parameters such as length scale and flow rate	Theoretical thermal mixing model*
Rowe, Johnson, and Knudsen (1974)	3 × 3 square array (P/D = 1.125 and 1.25)	Water	50,000 - 200,000	Velocity, turbulence intensity, autocorrelation function	Laser-Doppler velocimetry
Trupp and Azad (1975)	Triangular array rod bundle (P/D = 1.20, 1.35 and 1.50)	Air	12,000 - 84,000	Friction factors, local wall shear stresses, mean axial velocity, Reynolds stresses, eddy diffusivities	Pitot tubes, static pressure probe, hot-wire, differential pressure manometer, linearized constant pressure anemometry
Aly, Trupp and Gerrard (1978)	Triangular array	Air	53,000 - 107,000	Friction factors, mean axial velocity distributions, wall shear stress, secondary flows, Reynolds stresses	Pitot tubes, Betz projection manometer, hot-wire anemometry, static pressure taps
Rehme (1978)	Four parallel rods (P/D = 1.071)	Air	87,000	Velocity, wall shear stress, turbulence intensity	Pitot tubes, hot-wire anemometry
Seale (1979)	3 rod (P/D = 1.833), 4 rod (P/D = 1.375), and 5 rod (P/D = 1.1)	Air	34,000 - 300,000	Axial velocity contours, temperature distributions	Pitot-temperature probe, Betz manometer, thermocouple
Hooper (1980)	Square array (P/D = 1.107 and 1.194)	Air	48,000 - 156,000	Velocity distribution, wall shear stress, turbulence intensity, Reynolds stress	Pitot tubes, hot-wire anemometry
Seale (1982)	Two interconnected subchannels (P/D = 1.20)	Air	82,800 - 346,700	Axial velocity, secondary velocity, Reynolds stresses	Pitot tubes, hot-wire anemometry, Betz manometer
Renksizbulut and Hadaller (1986)	Square array (6 rods) (P/D = 1.15, W/D = 0.62)	Water	500,000	Wall shear stress, mean axial velocity, turbulence intensity	Preston tubes, laser Doppler anemometry
Vonka (1988)	Two triangular subchannels (P/D = 1.3)	Diethylether and toluene mixture	60,000 and 175,000	Velocity, secondary flow	Laser Doppler anemomtery,

contributing significantly to mixing between subchannels.

As discussed previously, evidence of periodic flow pulsations associated with turbulent subchannel flows was recorded in some earlier studies. Van Der Ros and Bogaardt (1970) [9] reported regular and visible waves in their thermocouple readings in the gap region. Rowe et al. (1974) [13] reported evidence that macroscopic flow processes exist adjacent to the rod gap. However, it is generally considered that Hooper and Rehme (1984) [21] were the first to experimentally identify and describe large scale turbulent flow pulsations through the gap. They performed detailed experiments in two geometries, a rectangular duct containing a single line of four rods (P/D = 1.026 - 1.118) and a test section characterizing a six-rod cluster (P/D = 1.107). Measurements were made in air at Reynolds numbers ranging from 54,600 to 105,000 and from 22,600 to 207,600 respectively for the two geometries. Techniques for resolving secondary flow velocities to within 1% of the local axial velocity failed to detect significant non-zero mean secondary flow components and secondary flows were dismissed as a mechanism for turbulent mixing between subchannels. Auto and cross-correlation functions of the measured velocity components clearly showed periodic behaviour through the gaps. Frequencies of the large scale flow pulsations were shown to vary linearly with Reynolds number. They considered the flow pulsations to be generated by an incompressible flow parallel-channel instability and that the pulsations are the dominant process for turbulent exchange between subchannels.

Rehme (1987) [22] presented a comprehensive review of previous experimental work as well results from a new systematic experimental study. The experimental geometry was similar to the rectangular duct geometry from Hooper and Rehme (1984) [21] with various P/D (1.036 - 1.40) and W/D (1.026 1.40) ratios. The

working fluid was air at Reynolds numbers between 54,600 and 194,000. He found the azimuthal turbulence intensity to increase from values close to that for pipe flow in the open subchannel region to maximum levels in the gap. He also found the maximum turbulence intensity in the gap to increase as the rod spacing or wall distance is reduced (P/D or W/D ratio). He declared the transfer processes through closely spaced rod arrays are governed by an energetic near periodic azimuthal turbulent velocity component through the gap and proposed a static pressure instability between subchannels as the generating mechanism.

Möller (1991) [23] applied hot wire and microphone techniques to measure turbulence intensity and wall pressure fluctuations in a rectangular duct containing a single line of four rods. Data were reported for P/D ratios between 1.007 and 1.224 and W/D ratios between 1.045 and 1.223. Measurements were made in air and results reported for Reynolds numbers between 25,000 and 110,000. The power spectra of the azimuthal velocity at the center of a rod-to-wall gap showed a very distinct peak. The corresponding spectra of the fluctuating pressure difference across the gap showed a peak at the same frequency as the fluctuating velocities. The peak frequency of gap pulsations (f) was shown to increase with Reynolds number, consistent with the findings of Hooper and Rehme (1984) [21]. He examined the spectra for various gap widths and found an increase in the peak frequency and the maximum value of the power spectra as the gap width was reduced. As such, the non-dimensional peak frequency (i.e., Strouhal number, St = fD/u_τ) defined by the rod diameter (D) and friction velocity (u_τ) was observed to depend only on the gap width and not on the Reynolds number. He likened the motion of the fluid through the gap to a vön Karman vortex street, transported by the main flow, with a stable and ordered pattern.

A phenomenological model of the gap cross-flow was proposed, consisting of alternating coherent large eddies moving through the gaps at a frequency characteristic of the geometry.

Subchannel methods are often employed in reactor analysis for computational efficiency. Fluid properties and the governing equations for heat transfer and fluid flow are spatially integrated over subchannels and averaged quantities established. As a result, the fine structures of the flow are not resolved and the approach requires correlations to define the complex exchange mechanisms of mass, momentum and energy between subchannels. In a follow-up publication, Möller (1992) [24] proposed a correlation for a mixing factor consistent with his phenomenological model described above. The model describes a decrease in mixing with increasing gap width.

Wu and Trupp (1993) [25] measured turbulence intensity and power spectra data in air (21,300 <Re <55,200) for a trapezoidal test section containing a single rod (1.020 <S/D <1.220). They reported the gap turbulence intensity to increase as the gap size is reduced, consistent with Hooper and Rehme (1984) [21] and Möller (1991) [23]. They also reported a lower limit to this trend, for extremely small gaps, cross-gap eddies vanished, presumably due viscous forces dominating the gap flow. Similar trends were reported by Chang and Tavoularis (2008) [26] for simulations of a single rod in a rectangular duct.

In a comprehensive study, Meyer and Rehme (1994) [27] presented experimental measurements including axial mean velocities, wall shear and Reynolds stresses and auto and cross-correlation spectral densities in slot and gap geometries. The gap geometry consisted of two rectangular subchannels connected by a narrow gap. The measurements were used to clearly identify large scale quasi-periodic structures in the

gap region of both subchannels. The frequency of oscillations through the gap was determined by the test section geometry and linearly dependent on the bulk velocity. They characterized these structures as two vortices, one on each side of the gap centerline, rotating in opposite directions. The vortices move downstream, driven by the higher velocities in the subchannels outside of the gap, with a convective velocity equal to the average of the velocities at the gap center and at the gap edge. The axial span of the two vortices was shown to be dependent on the test section geometry and was independent of the Reynolds number.

Subsequent studies have continued to confirm the existence of large scale quasi-periodic structures at the gap edges as well broaden our knowledge of the associated phenomena (e.g., Krauss and Meyer (1998) [28], Guellouz and Tavoularis (2000, Parts 1 [29] and 2 [30]), Baratto et al. (2006) [31]). A retrospective on the evolution of our understanding of inter-subchannel mixing and the role of quasi-periodic structures is provided by Meyer (2010) [32]. By the late-nineteen-nineties, it was reasonably well established that the dominant process contributing to coolant exchange between connected subchannels was the formation of these pulsations through the gap. Accordingly, any CFD methodology intended to model inter-subchannel mixing must be designed to capture the characteristics of the quasi-periodic structures. The following section focuses on findings associated with CFD related studies of relevant phenomena from recent years.

Table 2.2: Experimental investigations - periodic flow pulsations

Investigator(s)	Geometry	Working Fluid	Reynolds Number	Measured Data	Methodology
Hooper and Rehme (1984)	Rectangular duct with four parallel rods (P/D = 1.026 - 1.118), six rod square array (P/D = 1.107)	Air	54,600 - 105,000 and 22,600 - 207,600	Mean velocity, wall shear stress, Reynolds stress, turbulence intensity	Pitot tubes, Preston tubes, hot-wire anemometry
Rehme (1987)	Rectangular duct with four parallel rods (P/D =1.036 - 1.40, W/D = 1.026 - 1.40)	Air	54,600 - 194,000	Reynolds stresses, turbulence intensity, wall shear stress	Preston tubes, hot-wire anemometry
Möller (1991)	Rectangular channel with four parallel rods (P/D = 1.007 - 1.224, W/D = 1.045 - 1.223)	Air	25,000 - 110,000	Axial velocity, wall shear stress, Reynolds stresses, turbulence intensity	Pitot tubes, Preston tubes, hot-wire anemometry, microphones
Möller (1992)	Rectangular channel with four parallel rods (P/D =1.007 - 1.224, W/D = 1.045 - 1.223)	Air	60,880 - 148,100	Axial velocity, wall shear stress, Reynolds stresses, turbulence intensity	Pitot tubes, Preston tubes, hot-wire anemometry
Wu and Trupp (1993)	Trapezoidal duct with single rod (S/D = 1.020 - 1.220)	Air	21,300 - 55,200	Turbulence intensity, turbulence kinetic energy, secondary flow, wall shear stress,	Preston tubes, hot-wire anemometry
Meyer and Rehme (1994)	Compound rectangular channels (W/D = 1.06 - 1.25)	Air	250,000	Axial mean velocity, wall shear stress, Reynolds stress, spectral densities	Pitot tubes, Preston tubes, hot-wire anemometry
Krauss and Meyer (1998)	Central triangular subchannel in 37-rod bundle (P/D = 1.12 and 1.06)	Air	40,000 and 65,000	Mean velocities, temperatures, wall shear stresses, Reynolds stresses, turbulent quantities	Pitot tubes, Preston tubes, thermocouples, hot-wire anemometry
Guellouz and Tavoularis (2000)	Rectangular channel with cylindrical rod (P/D = 1.000 to 1.350)	Air	108,000	Mean velocity, wall shear stress, turbulent stress, flow visualization	Pitot tubes, Preston tubes, hot-wire anemometry
Lexmond, Mudde and van der Hagan (2005)	Two rectangular channels connected by a gap	Water	800 - 10,000	Axial velocity, mass transfer (by way of scalar tracer concentrations), flow visualization	2D particle image velocimetry, acetic acid tracer
Baratto, Bailey and Tavoularis (2006)	Five-rod bundle (P/D = 1.149)	Air	42,000	Mean velocity, wall shear stress, turbulence measurements	Hot-wire anemometry
Gosset and Tavoularis (2006)	Rectangular channel with rod and small gap (δ) (δ/D = 0.025 - 0.70)	Water	388 - 2,223	Flow visualization by dye injection	Dye injection
Mahmood (2011)	Two rectangular channels connected by a gap	Water	900 - 22,000	Axial velocity, mixing (by way of scalar tracer concentrations), flow visualization	Particle image velocimetry, Laser-Doppler anemometry, NaCl tracer

2.5 Summary of Relevant CFD Based Investigations

2.5.1 Steady RANS Based Studies

The earliest attempts to model inter-subchannel mixing by crediting only isotropic turbulent diffusion seriously under predicted measured mixing rates. As discussed above, these studies were important in the evolution to our current understanding of the mixing process, however, they cannot inform in any detail the current study and are not considered further.

Secondary flows are transverse flow components superimposed on the mean axial flow resulting from anisotropy in the normal stresses through the flow cross-section. Trupp and Aly (1979) [33] simulated fully developed flow in an infinite triangular rod array (P/D = 1.12 1.35; Re = 27,000 250,000) applying RANS with a turbulent kinetic energy transport equation and the secondary flow model of Launder-Ying (1973). They reported secondary flows that strengthened with increasing Reynolds number and weakened with increasing P/D ratio.

Rapley and Gosman (1986) [34] applied a finite-volume calculation method in a smooth rod bundle (P/D ratios of 1.06, 1.123 and 1.2) applying RANS, the k-ε turbulence model and the Launder-Ying (1973) secondary flow model. Secondary flow velocity profiles were considered in agreement with measurements of Tahir and Rogers (1979) for P/D = 1.06 at Re = 40,000. Sensitivity simulations showed good agreement with wall shear stress measurements with secondary flows included. Agreement was poor in the absence of secondary flows.

Lee and Jang (1997) [35] simulated fully developed turbulent flow in a bare triangular array rod bundle consistent with the experimental geometry of Carajilescov and Todreas (1976) with P/D = 1.123 and Re = 27,000. They applied a RANS approach with a non-linear k-ε model capturing the inequality of the Reynolds stresses, as required to promote secondary flows in non-circular ducts. Comparison of computed mean axial velocity contours with the corresponding results from Carajilescov and Todreas (1976) showed good agreement in the major part of the subchannel. Based on sensitivity simulations with secondary flow calculations suppressed, the authors concluded that the secondary flow effects are significant for this parameter. Similar calculations for a closely spaced square array consistent with experiments by Hooper (1980) (P/D = 1.107, Re = 48,400) under predicted turbulent stresses in the gap region. They conclude that the secondary flow model is incapable of capturing the high turbulent stresses in the gap which requires modelling of the transport effect of large scale cross-gap eddy motion.

Baglietto and Ninokata (2005) [36] simulated fully developed flow in a triangular array subchannel applying RANS and periodic boundary conditions. They assessed performance of three isotropic turbulence models (k-ε, k-ω and SST) along with a non-linear form of the k-ε model, i.e., the Shih Zhu Lumley model (SZL). Results for velocity distribution and wall shear stress are compared with measurements by Mantlik et al. (1976). The SZL model, which accounts to some extent for the anisotropy and associated secondary flows, performed best compared to the linear models. The SZL model was then modified by adjusting coefficients of the non-linear terms to account for higher anisotropy. Computations with the modified model produced much better agreement with measurements of wall shear stress and axial velocity profiles.

Tóth and Aszódi (2010) [37] assessed two isotropic turbulence models (k-ε and SST) and two anisotropic models (BSL Reynolds stress and SSG Reynolds stress) in application to a triangular array subchannel (P/D = 1.35). A steady RANS approach and periodic boundary conditions were applied. Results are compared with measurements from Trupp and Azad (1975) [14]. The results demonstrate that the Reynolds stress models (BSL and SSG) are able to predict the anisotropy of the normal stresses, which are responsible for secondary motions, whereas the k-ε and SST models of course could not. The BSL Reynolds stress model was deemed to provide the overall best prediction of turbulence quantities including secondary flows and was selected for a subsequent assessment of the effect of a flow obstruction (spacer grid). The fact that unsteady RANS calculations were not required to predict the turbulent quantities was attributed to the rather open lattice geometry as compared to other studies (e.g., Chang and Tavoularis, 2007 [38]). The effect of the spacer grid was to alter the axial velocity distribution and to enhance mixing between subchannels downstream of its location. These effects were seen to diminish with distance from the spacer grid.

2.5.2 Unsteady RANS Based Studies

Steady RANS based calculations accounting for secondary flows (through ad hoc models or anisotropic turbulence models) moved predicted turbulence quantities toward measured values; although they were still generally under predicted. Reasonable agreement with experiments was obtained only in higher aspect ratio lattices where the turbulence intensities attributable to the gap pulsations diminish; or in calculations where anisotropy factors or coefficients were scaled to very high values. As

Table 2.3: Reynolds averaged Navier-Stokes (RANS) based investigations

Investigator(s)	Experimental Validation	Turbulence Model	Secondary Flow Model	Anisotropy Factor
Aly, Trupp and Gerrard (1978)	Aly, Trupp and Gerrard (1978)	k-transport equation model	Launder and Ying (1973)	None
Seale (1979)	Seale (1979)	k-ε transport equation model	Launder and Ying (1973)	Empirical correlations
Trupp and Aly (1979)	Kjellstrom (1971), Carajilescov and Todreas (1976), Trupp and Azad (1975)	Turbulent kinetic energy transport equation	Launder and Ying (1973)	None
Seale (1982)	Seale (1982)	k-ε	Launder and Ying (1973)	Empirical correlations
Rapley and Gosman (1986)	Carajilescov and Todreas (1976), Trupp and Azad (1975)	k-ε	Seale (1982)	None
Lee and Jang (1997)	Carajilescov and Todreas (1976)	non-linear k-ε	Captured in anisotropic turbulence model	None
Rock and Lightstone (2001)	Seale (1979)	k-ε	N/A	None
Baglietto and Ninokata (2005)	Mantlik, Heina and Chervenka	k-ε, k-ω, SST	Captured in non-linear models	None
Tóth and Aszódi (2010)	Trupp and Azad (1975)	k-ε, SST, BSL Reynolds Stress Model, SSG Reynolds Stress Model	N/A	None

more studies carried out unsteady RANS based calculations, it became clear that this approach was capable of capturing the characteristics of periodic oscillations through the gap.

Biemüller et al. (1996) [39] measured time averaged values of axial velocity and wall shear stresses as well as turbulent normal and shear stresses in a gap-connected twin-subchannel geometry. The working fluid was air at atmospheric pressure and room temperature (Re = 200,000). The authors also carried out LES simulations in a sub domain of the test section applying periodic boundary conditions to limit computational effort. Qualitative agreement between predictions and experimental measurement was obtained. In particular, the LES simulations did capture large scale pulsations through the gap which could be characterized by two counter-rotating vortices centered on opposite sides of the gap centerline.

Chang and Tavoularis (2007) [38] performed unsteady RANS calculations with a Reynolds stress model (RSM) to simulate a 60° sector of 37-rod bundle. The computational geometry approximates a subdomain of the experimental geometry of Ouma and Tavoularis (1991a,b) [40] [41] and Baratto et al. (2006) [31], although some physical discrepancies between experiment and model are noted. They applied periodic boundary conditions in the streamwise direction as well as at the two radial boundaries which allowed the 60° sector to be modelled. Simulations demonstrated coherent structures with characteristics similar to the experiments in regards to their distribution and interaction. Time averaged quantities (e.g., streamwise velocity and turbulent shear stresses) showed reasonable agreement with experiments. The predicted average Strouhal number associated with the coherent structures was noted to be almost twice the experimental value. The authors conclude that an unsteady

RANS formulation combined with the RSM is a viable approach for bundle applications.

Chang and Tavoularis (2008) [26] again performed unsteady RANS calculations with a Reynolds Stress Model to simulate flow in a rectangular channel carrying a single suspended rod. The geometry is consistent with the experimental geometry from Guellouz and Tavoularis (2000, Parts 1 and 2) [29] [30] to allow comparison. They considered varying gap dimensions (S/D = 0.10, 0.03 and 0.01) at a Reynolds number of 108,000. Periodic boundary conditions were applied in the streamwise direction. They report that temperature fluctuations and turbulent kinetic energy increased when the gap is reduced from S/D = 0.10 to 0.03. Both parameters decreased with a further reduction to 0.01. They concluded that, for a given geometry and Reynolds number, there is a critical relative gap size (S/D) for which the coherent structure frequency would reach a maximum. As the gap size is reduced, viscous effects begin to damp out flow pulsations until they are eliminated. For larger gap sizes, pulsations are also expected to diminish as the lattice becomes more open.

Merzari et al. (2008) [42] simulated flow in a gap connected twin-subchannel geometry and in a tight-lattice rod bundle geometry. They compared results with related experiments by Lexmond et al. (2005) [3] and by Krauss and Meyer (1998) [28] respectively. LES simulations as well as k-ε based steady and unsteady RANS calculations were carried out. Sensitivity to isotropic versus anisotropic turbulence modelling was also assessed. A steady RANS calculation applying periodic boundary conditions significantly under predicted the averaged axial velocity profile through the gap mid-plane in the twin-subchannel geometry. A corresponding LES calculation agreed very well with the experimental measurements in this regard and was

shown to capture characteristics of the gap flow pulsations. Unsteady RANS calculations for a tight-lattice rod bundle geometry was shown to predict the frequency and amplitude of oscillations although the computed wavelength was significantly larger than determined experimentally. The authors conclude that unsteady RANS calculations are necessary in oscillating conditions to accurately predict even averaged statistics of the flow. They state that although LES and DNS offer higher potential to model the complex unsteady phenomena associated with fuel bundle flow, they are impractical for reactor calculations due to higher computational overhead. They recommend unsteady RANS methods and applying anisotropic turbulence models for these applications.

Abbasian et al. (2009) [43] carried out measurements and simulated flow in a 43-rod CANDU bundle (Re = 21,600 86,400). Calculations were made using large eddy simulation (LES), detached eddy simulation (DES) and the Reynolds stress model (RSM). Predictions of mean flow characteristics compared well with experiments for all three models. The LES results agreed best with measurements in terms of instantaneous quantities (e.g., the peak frequency of flow oscillations), RSM was least accurate. Although LES was the most computationally expensive, the authors recommend its use to predict CANDU fuel bundle flows.

Home et al. (2009) [44] simulated flows in a twin rectangular subchannel geometry consistent with the experimental test section of Meyer and Rehme (1994) [27]. They validated simulation results applying the Spalart - Allmaras (SA) turbulence model and the k-ε model in an unsteady RANS framework against the experimental measurements. The simulations applied periodic boundary conditions in the axial direction. The SA model coupled with a second order accurate in space advection

scheme performed best in regard to prediction of the dynamics of the flow. In particular, the quasi-periodic nature of the velocity time traces and the frequency and wavelength of the flow pulsations. Although this model is isotropic, the authors assess that the anisotropic effects of secondary flows on mixing are not significant due to their low magnitude. As a one equation model, SA is more computationally efficient compared to two equation models or the Reynolds stress model and is concluded to be a promising option for rod bundle arrangements.

Liu and Ishiwatari (2011) [45] simulated turbulent flows in a rectangular duct with a suspended cylindrical rod, and in twin cylindrical subchannels connected by a narrow gap. Simulation results are compared with experimental measurements from Guellouz and Tavoularis (2000a) [29] and Sadatomi et al. (1996) [46] respectively. Periodic boundary conditions were applied in a sub-domain of the experimental test section for the rectangular duct. For the twin-subchannel calculations, the simulation domain was the entire test section with inlet flow and outlet pressure boundary conditions. All simulations use the explicit algebraic Reynolds stress model (EARSM). Results demonstrate that the model predicted reasonably well the peak frequency of the crossflow pulsations and the streamwise structure length in the rectangular channel. Results from the twin-subchannel geometry indicated the formation of vortices on either side of the gap and produced good agreement with mixing measurement. Based on both simulations, they conclude that the explicit algebraic Reynolds stress model can accurately predict quasi-periodic flow between subchannels.

Hong et al. (2011) [47] used LES to study heat transfer characteristics in twin rectangular subchannels separated by a slot (i.e., a gap depth of $D \approx 0.0$). A similar model with a gap connection ($S/D = 0.13$) was first generated in order to validate

their model against the measurements in air from Meyer and Rehme (1994) [27]. Good agreement with experimental mean axial velocity profile measurements through the subchannel was considered adequate to validate the model. For the slot geometry, a uniform heat flux boundary condition was applied to all walls except the internal wall separating the channels, which was adiabatic. Sensitivity assessments considering slot height (h = 0.0, 0.005, 0.01 and 0.015) and Reynolds number (Re = 50,000, 100,000 and 200,000) were carried out to isolate the effects on overall heat transfer characteristics. In the absence of an opening between the channels (i.e., h = 0.0), there are no flow pulsations between the subchannels and wall temperatures monotonically increase through the length of the domain. However, as the slot height is increased, flow pulsations are generated downstream of the inlet and a corresponding decrease in wall temperatures is seen. The enhanced heat transfer from the walls is associated with mixing of the fluid in each subchannel from the cross channel pulsations reducing coolant temperatures at the wall surface. Channel pairs with periodic flow between them showed a 20-35% enhancement in heat transfer over those without it. This is at a cost of approximately a 20% increase in pressure drop.

Yan et al. (2012) [48] modelled heat transfer in a pair of subchannels representing the interior of a rod bundle geometry consistent with the experiments performed by Krauss and Meyer (1996, 1998) [49] [28]. They carried out reference calculations (P/D = 1.06, air at Re = 38,754) applying both steady and unsteady RANS coupled with a RSM. Periodic boundary conditions were applied in both the streamwise and radial directions. The reference model results for unsteady RANS provided satisfactory results compared to the Krauss and Meyer (1996) [49] measurements while steady RANS calculations were unsatisfactory. With the validated unsteady RANS model,

they studied the effects of varying Reynolds number, Prandtl number and P/D ratio. Higher Reynolds numbers were shown to demonstrate larger, more stable coherent structures. For a Reynolds number of 38,754 they found a pitch-to-diameter ratio of 1.03 to be the critical gap size for the quasi-periodic flow as the effective radial velocity was shown to be a maximum. They conclude reactor core design should take into account a critical gap size to maximize mixing and heat transfer while cautioning that tolerances and operational deformation must also be factored into the design.

2.6 Appendage Related Studies

The body of work considering the effects of appendages on inter-subchannel mixing is not as extensive as that without appendages. A larger portion of the related studies have considered bundle geometries as opposed to gap connected subchannel pairs. These studies are often planned and presented in terms of the effect of appendages directly on the bundle design parameters of heat transfer (Nusselt number) and pressure drop as opposed to the contributing parameter of inter-subchannel mixing. Following is a brief overview of relevant experimental and numerical work concerning appendages and inter-subchannel mixing.

An early experimental study by Rowe and Chapman (1973) [50] evaluated the effect of grid spacers on the axial turbulent flow structure in a model rod bundle with a pitch-to-diameter ratio of 1.25. Measurements were performed in water at Reynolds numbers of 50,000, 100,000 and 200,000. Local axial velocity, turbulence intensity and Eulerian time correlations were measured at selected positions downstream from the spacer using laser-Doppler velocimetry. They reported significant local velocity perturbations in the wake of the grid spacer recovering within approximately 18

Table 2.4: Unsteady Reynolds averaged Navier-Stokes (RANS) based investigations

Investigator(s)	Experimental Validation	Turbulence Model
Biemüller, Meyer and Rehme (1996)	Biemüller, Meyer and Rehme (1996)	Large Eddy Simulation
Chang and Tavoularis (2005) (2006)	Guellouz and Tavoularis (2000)	Reynolds Stress Model initialized from RNG k-ε transport equation model
Chang and Tavoularis (2007)	Guellouz and Tavoularis (2000)	Reynolds Stress Model
Arvanitis (2008)	Meyer and Rehme (1994)	Spalart-Allmaras
Chang and Tavoularis (2008)	Guellouz and Tavoularis (2000)	Reynolds Stress Model initialized from RNG k-ε transport equation model
Merzari, Ninokata, and Baglietto (2008)	Krauss and Meyer (1998)	Anisotropic k-ε transport equation model
Abbasian, Yu and Cao (2009)	Abbasian, Yu and Cao (2009)	Large eddy simulation (LES) with dynamic Smagorinsky model (DSM), detached eddy simulation (DES), Reynolds stress model (RSM)
Home, Arvanitis, Lightstone, and Hamed (2009)	Meyer and Rehme (1994)	Spalart-Allmaras
Derksen (2010)	Lexmond et al. (2005)	Lattice Boltzmann method* (LBM)
Liu and Ishiwatari (2011)	Guellouz and Tavoularis (2000a) Sadatomi, Kawahara, Sato (1996)	Explicit algebraic Reynolds stress model (EARSM)
Mahmood (2011)	Mahmood (2011)	Large Eddy Simulation
Hong, Seo, Byun, Choi, and Dhin (2011)	Meyer and Rehme (1994)	LES with Smargorinsky sub-grid scale model
Yan, Gu, and Yu (2012)	Krauss and Meyer (1996, 1998)	Steady and unsteady RANS coupled with RSM

hydraulic diameters downstream. The grid spacer effect on turbulent structure was found to be weakly dependent on Reynolds number with decreasing influence further downstream from the spacer. The spacer effect on mixing could only be inferred from their measurements. This inference indicated reduced crossflow mixing downstream of the spacer which the authors discounted suggesting that an increase in mixing is possible.

Gencay et al. (1984) [51] performed experiments in water on a pair of square channels connected by a narrow slot. The objective was to study the diversion crossflow behaviour when one of the channels is partially or completely blocked. The measured parameters were pressures and mass flow rates in the channels upstream and downstream of the blockage. Variations in blockage severity and geometry were considered. In the region upstream of the blockage, diversion crossflow induced by the blockage takes place over a relatively short distance. Recovery downstream of the blockage is a comparatively slower process with recovery distance increasing with blockage severity. Recovery was noted to be faster for smooth as compared to blunt blockages.

Yang and Chung (1996) [52] measured velocity and turbulence intensity in the axial and crossflow directions as well as axial pressured drop in a 6×6 rod bundle geometry (P/D = 1.33) containing spacer grids. The working fluid was water at 25°C and a Reynolds number of 63,924. The effect of spacers on mixing was deduced from models based on analogies between turbulent heat and momentum transfer. Mixing factors were highest just downstream of the spacer grid, decreasing to stable values at approximately 15 hydraulic diameters downstream. Mixing vane type spacer grids were shown to promote more thermal mixing than those without vanes.

Holloway et al. (2008) [53] performed experiments on a 5×5 heated rod bundle array held in place by way of support grids. Measurements were made in air at Reynolds numbers of 29,000 and 35,000 with four different support grid designs. Measurements included pressure drop and rod surface temperature at various axial locations downstream of the bundle support grids. The support grids were shown to enhance heat transfer locally in the bundle with the maximum heat transfer enhancement at their downstream edge. Most of the enhancement occurs within 10 hydraulic diameters of the support grid. The two split-vane pair type support designs yielded Nusselt numbers slightly below the fully developed value between 10 and 30 hydraulic diameters downstream. Standard and disc designs produced Nusselt numbers slightly above fully developed in this region. All designs returned to fully developed heat transfer characteristics within 35 hydraulic diameters. Normalized Nusselt numbers were found to be independent of Reynolds number in the range tested.

A CFD evaluation of turbulence models applicable to rod bundles with spacer assemblies was carried out by Liu et al. (2012) [54]. A simplified computational geometry representing four interior subchannels of a 5×5 square-array rod bundle was analysed (P/D = 1.33) for two spacer designs (standard and split-vane pair). Periodic boundary conditions were applied at the lateral computational boundaries representing gaps. Uniform inlet flow and constant exit pressure boundary conditions were applied in the streamwise direction. Several different turbulence closure models were investigated; the renormalization group k-ε model (RNG), realizable k-ε model (RKE), low-Re k-ε model, standard k-ω model, shear stress transport k-ω model (SST k-ω) and the Reynolds stress model (RSM). In addition, a sensitivity assessment of steady versus unsteady RANS methodology applying the RKE model

and the RSM is presented. Model predictions of axial and circumferential Nusselt number distributions are compared with the data of Holloway et al. (2004, 2005)[55] [56]. The authors recommend the RKE model with near-wall functions for simulating regions close to support grids. Predictions of axial and circumferential Nusselt number distributions from the steady and unsteady RANS calculations converged by approximately 6.5 hydraulic diameters downstream of the spacer. The unsteady treatment predicted higher Nusselt numbers than the steady treatment within the 6.5 hydraulic diameters.

An international benchmark study was initiated to test the ability of state-of-the-art CFD codes to predict important turbulence parameters downstream of a generic spacer grid design in rod-bundle geometries. The Korea Atomic Energy Research Institute (KAERI) performed a series of experiments for this purpose. The results of the study are presented by Smith et al. (2013) [57].

The test section consisted of a square channel containing a 5×5 rod bundle array. A mixing spacer grid is situated in the rod bundle for enhancing lateral flow mixing. The working fluid was water, the Reynolds number considered was Re $\approx$ 50 000, the tests were adiabatic and scalar mixing between subchannels was not measured. Detailed measurements of the velocity field were taken using a two-dimensional LDA system at four downstream locations from the spacer grid.

In total, 25 participants submitted blind CFD results. Of the 25 submissions, five used RANS turbulence modelling, ten used unsteady RANS, four used a hybrid approach, and the remaining six used LES. The number of control volumes in the submissions spanned 700K to 144M. Of the simulation results submitted, the majority (19) were obtained using the three commercial CFD software packages ANSYS CFX,

FLUENT and STAR-CCM+. Results from the Canadian participation in this exercise are presented in Szymanski et. al (2012) [58]. The contribution from McMaster University is documented in Rashkovan and Novog (2012) [59].

Analysis of calculated results showed that good agreement with experimental data can be achieved with a moderate number of mesh cells and less-sophisticated turbulence models. Generally, LES models and the SAS-SST turbulence model performed well. An improvement in agreement was noted with isotropic turbulence modelling between steady and unsteady RANS applications. The application of an anisotropic turbulence model (RSM) in an unsteady RANS framework showed little improvement over the isotropic (k-ω) unsteady RANS results.

2.7 Summary

Experimental and numerical investigations over many decades have clearly demonstrated that turbulent transport through gap regions of tight lattice geometries is dominated by non-gradient, macroscopic flow processes. These processes are characterized by large scale quasi-periodic structures at gap edges promoting inter-subchannel mixing by way of crossflow pulsations through gaps. It has been established that CFD analyses are capable of predicting the entire three-dimensional flow field in such geometries and can be used to advance our understanding of the underlying physics.

Standard isotropic turbulent diffusion models in a steady RANS framework are not capable of simulating the formation of the oscillating structures. Consequently, these calculations significantly under predict the magnitude of mixing between subchannels. Although DNS and LES can model such complex unsteady flows, they carry a very high computational overhead making them impractical for this study.

The length and timescales of the coherent structures are significantly larger than those inherent in open pipe turbulent flow. As such, they can be captured through calculations applying unsteady RANS equations coupled with a suitable turbulence model and simulation time step. The SA model has been successfully applied in an unsteady RANS framework to simulate flow pulsations in gap connected twin-subchannel geometries (Arvanitis, 2008) [60]. The SA model is a complete and computationally efficient model with acceptable general performance and a demonstrated capability for this specific application. As such, an unsteady RANS based approach applying the SA model is a reasonable choice for the current study.

The reference experimental work for this numerical study is from Lexmond et al. (2005) [3] and Mahmood (2011) [2] supplemented by the numerical analysis of Derksen (2010) [61]. These investigators presented results of experimental and/or numerical assessments of turbulent flow structure and mixing for a specific twin-subchannel geometry considering a similar range of flow conditions. Further details of these investigations are presented in Chapter 4 (Methodology) and Chapter 5 (Results).

Chapter 3

Mathematical Modelling

3.1 The Navier-Stokes Equations

The Navier-Stokes equations are a set of nonlinear partial differential equations that describe fluid flow. These equations define the relationship between the velocity, pressure, and density of a moving fluid. They were derived by Claude-Louis Navier (France) and Sir George Stokes (England) in the early 1800s. The Navier-Stokes equations are based on an assumption that a fluid is a continuum at the scale of interest. They consist of four time-dependent equations: one for conservation of mass and three for conservation of momentum (one in each spatial direction). The Navier-Stokes equations, in their general form, are described in the following sections.

3.1.1 Continuity Equation

The continuity equation (i.e., conservation of mass) in its general form is defined by:

$$\frac{\partial \rho}{\partial t} + \boldsymbol{\nabla} \cdot \rho \mathbf{U} = 0 \tag{3.1}$$

where U is the velocity vector and ρ the fluid density.

In index notation, Equation 3.1 is written as:

$$\frac{\partial \rho}{\partial t} + \frac{\partial \rho u_i}{\partial x_i} = 0 \tag{3.2}$$

For an incompressible flow where density is constant and uniform, Equation 3.2 simplifies to:

$$\frac{\partial u_i}{\partial x_i} = 0 \tag{3.3}$$

3.1.2 Conservation of Momentum

The conservation of momentum equation in the absence of body forces can be written as:

$$\frac{\partial \rho u_i}{\partial t} + \frac{\partial \rho u_j u_i}{\partial x_j} = -\frac{\partial p}{\partial x_i} + \frac{\partial}{\partial x_j}\left[\mu\left(\frac{\partial u_i}{\partial x_j} + \frac{\partial u_j}{\partial x_i}\right)\right] \tag{3.4}$$

where the additional variable is the fluid dynamic viscosity, μ. The terms in Equation 3.4 correspond to the inertial forces (LHS), pressure forces, and viscous forces applied to the fluid (RHS).

3.2 The Scalar Transport Equation

The scalar transport equation describes mathematically the processes by which scalar quantities are transported within a physical system. Scalar quantities include dissolved species, dispersed species, or heat. The main processes involved in scalar transport include, but are not limited to, advection and diffusion.

A passive scalar refers to a diffusive species in a fluid at a sufficiently low concentration that it has no effect on fluid motion by way of altering fluid properties (e.g., density or viscosity). Flows with low concentration tracers or that are weakly heated are two such examples that can be treated analogously.

The scalar transport equation describing instantaneous advection and diffusion of a species in a fluid is given by:

$$\frac{\partial(\rho\phi)}{\partial t} + \frac{\partial(\rho u_i \phi)}{\partial x_i} = \frac{\partial}{\partial x_i}\left[\rho\Gamma_\phi \frac{\partial \phi}{\partial x_i}\right] + S_\phi \tag{3.5}$$

where ϕ represents the transported scalar (e.g., species mass concentration or temperature); Γ_ϕ, the diffusion coefficient for species ϕ (specifically molecular diffusivity of a transported scalar or the thermal diffusivity for temperature) and S_ϕ is a source term accounting production and/or consumption of the species.

3.3 Solving the Navier-Stokes Equations

For most practical applications, analytical solutions to Navier-Stokes equations are not readily available. Solutions do exist for some rather simple laminar flows wherein a number of terms in the equations vanish or can be considered negligible (e.g., Couette flow). However, in general, computational fluid dynamics (CFD) applying a variety of

techniques such as finite difference, finite volume, finite element and spectral methods are used to obtain solutions to the set of equations or approximations to them.

Direct Numerical Simulation (DNS) is a CFD technique which solves directly the unsteady three-dimensional Navier-Stokes equations in the absence of statistical averaging or empirical closure models. DNS does not involve approximations, other than those due to discretization, which are inherent to any numerical solution of differential equations [62]. DNS must use a domain large enough to accommodate the largest naturally-occurring turbulent eddies while using a grid fine enough to fully resolve the dissipation scales. The range of these scales increases with Reynolds number leading to computer time and storage requirements that in turn increase rapidly with Reynolds number. As a result, DNS applications are limited to relatively low Reynolds numbers in practice and it is very expensive to conduct a DNS calculation at even moderately high Reynolds number [62].

Most of the computational effort in DNS is expended resolving the smallest, dissipative scale motions, whereas the energy and anisotropy are contained predominantly in the larger scales of motion. A less computationally onerous solution technique in comparison to DNS is Large-Eddy Simulation (LES). In LES, the dynamics of the larger-scale motions (which are affected by the flow geometry and are not universal) are computed explicitly as in DNS, the influence of the smaller scales (which have, to some extent, a universal character) is represented by simple models. In computational expense, LES lies between Reynolds stress models (discussed later) and DNS, and is motivated by the limitations of each [63]. Although more computationally efficient than DNS, LES is still too expensive for routine industrial applications [62].

As the computational effort required to fully resolve (DNS) or partially resolve

(LES) all but very simple turbulent flows with the complete set of Navier-Stokes equations is prohibitive, approximations to the set of equations are typically solved in practice. These techniques comprise the Reynolds averaged Navier-Stokes (RANS) equations combined with models to close the set of equations by accounting for the Reynolds stress terms that arise from the averaging procedure. These topics are discussed in detail in the following sections.

3.4 The Reynolds Averaged Navier-Stokes Equations

The concept of applying statistical averaging to the Navier-Stokes equations in order to characterize turbulent flows was introduced by Osborne Reynolds in the late 1800s. Reynolds decomposed the instantaneous velocity field (u_i) into a time average or mean component ($\bar{u}_i$) and a turbulent fluctuation (u_i') such that the total instantaneous velocity is given by:

$$u_i = \bar{u}_i + u_i' \tag{3.6}$$

Likewise, decomposition of the pressure field yields:

$$p = \bar{p} + p' \tag{3.7}$$

where the time averaged pressure component is given by $\bar{p}$, the turbulent pressure fluctuation by p' and the total instantaneous pressure is p.

Consider the time averaged component of an unsteady turbulent variable (using

velocity, u_i, as an example) to be defined by:

$$\bar{u}_i = \frac{1}{T}\int_{t_0}^{t_0+T} u_i dt \tag{3.8}$$

If T is large compared to the relevant period of the fluctuations but small compared to the period of large scale fluid motions, the time averaged or mean value can vary slowly with time. This is the case of an unsteady turbulent flow [64].

Substituting Equation 3.6 into the continuity equation (Equation 3.2) and averaging the result can be shown to yield the following:

$$\frac{\partial \rho}{\partial t} + \frac{\partial \rho \bar{u}_i}{\partial x_i} = 0 \tag{3.9}$$

where it has been recognized that the mean fluctuating components ($\bar{u}_i'$) are zero. This is the Reynolds averaged continuity equation and has the form of the continuity equation (Equation 3.2), written in terms of the average velocity components.

Substituting Equations 3.6 and 3.7 into the conservation of momentum equation (Equation 3.4) and averaging the result can be shown to yield:

$$\frac{\partial \rho \bar{u}_i}{\partial t} + \frac{\partial}{\partial x_j}(\rho \bar{u}_i \bar{u}_j) = -\frac{\partial \bar{p}}{\partial x_i} + \mu \frac{\partial^2 \bar{u}_i}{\partial x_j^2} - \frac{\partial}{\partial x_j}(\rho \overline{u_i' u_j'}) \tag{3.10}$$

Equation 3.10 resembles the momentum equation (Equation 3.4) written in terms of the mean flow and pressure with additional terms involving products of the turbulent fluctuations ($\rho \overline{u_i' u_j'}$). These terms are the Reynolds stresses which represent the average momentum flux due to turbulent velocity fluctuations and describe how the fluctuating part of the flow interacts with and forces the mean flow [62].

The Navier-Stokes equations (Equations 3.2 and 3.4) form a fully determinate

system with four equations (three directional components of the momentum equation and continuity) written in terms of four unknowns (three directional components of the velocity vector and pressure). The Reynolds averaged Navier-Stokes equations (Equations 3.9 and 3.10) comprise only the four analogous averaged equations but are written in terms of the four analogous averaged unknowns plus the Reynolds stresses. As such, the RANS system of equations is indeterminate as the number of unknowns exceeds the number of equations. Closure of the RANS equations through modelling of the Reynolds stresses is disused in a later section.

3.5 The Reynolds Averaged Scalar Transport Equation

In addition to enhancing momentum flux, turbulent velocity fluctuations contribute to enhanced transport of scalar quantities. The scalar transport equation (Equation 3.5) can be Reynolds averaged applying an approach similar to that yielding the RANS equations. Decomposing the scalar quantity (ϕ) in Equation 3.5 into mean and fluctuating components yields:

$$\phi = \bar{\phi} + \phi' \tag{3.11}$$

Substituting Equation 3.6 and Equation 3.11 into Equation 3.5 and averaging the result, in the absence of sources or sinks, can be shown to yield:

$$\frac{\partial(\rho\bar{\phi})}{\partial t} + \frac{\partial(\rho\bar{u}_i\bar{\phi})}{\partial x_i} = \frac{\partial}{\partial x_i}\left[\rho\Gamma_\phi\frac{\partial\bar{\phi}}{\partial x_i} - \rho\overline{\phi' u_i'}\right] \tag{3.12}$$

The term $\overline{\phi' u_i'}$ in Equation 3.12 resembles the Reynolds stress term in the RANS momentum equation (Equation 3.10). This term characterizes the transport of ϕ in the x_i direction by turbulent fluctuations. As with the Reynolds stress terms, this term also must be modeled and is discussed in a later section.

3.6 Turbulence Modelling

3.6.1 Closing the RANS Equations

The evolution of the Reynolds stresses in formulating the RANS equations creates an imbalance between equations and unknowns and a closure problem for the system. For typical engineering applications, the details of the turbulent fluctuations are not important, but capturing their influence on the mean flow is. Turbulence models provide a mechanism to quantify this influence without resolving the complete time dependent flow field. As such, in RANS applications, the averaged flow field velocities are calculated with the effect of fluctuations being modelled.

Many turbulence models are based on the Boussinesq hypothesis (J. Boussinesq 1877). The hypothesis assumes a linear relationship between the Reynolds stresses and the mean velocity gradients. The concept is analogous to molecular shear stress in an incompressible Newtonian fluid where the stresses (τ_{ij}) are linearly correlated to the local velocity gradients through the dynamic viscosity (μ), i.e.:

$$\tau_{ij} = \mu \left[\frac{\partial \bar{u}_i}{\partial x_j} + \frac{\partial \bar{u}_j}{\partial x_i} \right] \tag{3.13}$$

After defining a turbulent or eddy viscosity (μ_t) to correlate Reynolds stresses with the mean velocity gradients, the Bousinesq hypothesis for an incompressible fluid is

mathematically expressed as:

$$-(\rho\overline{u_i'u_j'}) = \mu_t\left[\frac{\partial\bar{u}_i}{\partial x_j} + \frac{\partial\bar{u}_j}{\partial x_i}\right] - \frac{2}{3}\rho k\delta_{ij} \tag{3.14}$$

where δ_{ij} is the Kronecker delta function and k is the turbulence kinetic energy per unit mass defined as:

$$k = \frac{1}{2}\overline{u_i'u_i'} \tag{3.15}$$

The second term on the RHS of Equation 3.14 is added to ensure the sum of the normal stresses is $2k$ as required by the definition of k. In some higher order models where k is calculated (e.g., k-ω) it is retained. In simpler models (e.g., algebraic models, Spalart-Almaras), this term is often ignored.

Although the eddy viscosity is dimensionally equivalent to its molecular counterpart, dynamic viscosity (kg/m·s), it is not a fluid property. The eddy viscosity depends on a variety of parameters including geometry, flow conditions and history and as such must be modeled. It should be noted that division of the eddy viscosity (μ_t) by density (ρ) gives the kinematic eddy viscosity (ν_t).

A large number of turbulence models have been developed based on the eddy viscosity concept. These are classified as zero-equation, 1-equation, 2-equation, and higher order models. The number of equations referring to the number of additional PDEs or transport equations the model adds to the RANS set of equations. Higher order models progressively provide a fuller description of the turbulence and tend to be more broadly applicable and accurate than lower order models. However, with increasing order, complexity increases and computational efficiency decreases.

The simplest turbulence models are the zero-equation (or algebraic) models. Examples include the uniform turbulent viscosity model and the mixing-length model. Although these models are relatively simple to implement and are computationally efficient, in general, they have a limited range of applicability [63]. In the current study, the 1-equation Spalart-Allmaras and 2-equation k-ω models are applied and are discussed in the following sections.

3.6.2 The Spalart-Allmaras Model

One-equation models are generally based upon the eddy-viscosity approximation and a transport equation for turbulence kinetic energy or for eddy viscosity. Models based on eddy viscosity are not hampered by the need to specify length scales related to the local shear layer thickness as required by turbulence kinetic energy based models and are therefore considered complete. Models formulated in this way typically require more closure coefficients, closure functions or empirical damping functions but are more broadly applicable without specific calibration than turbulence kinetic energy based one-equation models [65].

The Spalart-Allmaras (SA) [66] model is a one equation model which adds a transport equation for a modified kinematic eddy viscosity ($\tilde{\nu}$) to the RANS set of equations. The model follows the formulation of the earlier Baldwin-Barth model [67]. Spalart and Allmaras constructed, term by term, a transport equation for $\tilde{\nu}$ written as:

$$\frac{\partial \rho\tilde{\nu}}{\partial t} + \frac{\partial}{\partial x_j}(\rho\tilde{\nu}\bar{u}_j) = c_{b1}\rho\tilde{S}\tilde{\nu} + \frac{1}{\sigma}\left[\frac{\partial}{\partial x_j}\left\{(\mu+\rho\tilde{\nu})\frac{\partial\tilde{\nu}}{\partial x_j}\right\} + c_{b2}\rho\left(\frac{\partial\tilde{\nu}}{\partial x_j}\right)^2\right] - c_{w1}f_w\rho\left(\frac{\tilde{\nu}}{d}\right)^2 \tag{3.16}$$

The terms on the LHS of Equation 3.16 are the local rate of change of eddy viscosity and the transport of eddy viscosity by convection. The first term on the RHS of Equation 3.16 is the production of eddy viscosity, the second diffusion and the third dissipation.

In the SA model, the modified kinematic eddy viscosity ($\tilde{\nu}$) is related to the kinematic eddy viscosity (ν_t) through a wall damping function (f_{v1}) as:

$$\nu_t = \tilde{\nu} f_{v1} = \frac{\mu_t}{\rho} \tag{3.17}$$

The damping function (f_{v1}) is adapted from Mellor and Herring [68] and is defined as:

$$f_{v1} = \frac{\chi^3}{\chi^3 + {c_{v1}}^3}, \text{ with } \chi = \frac{\tilde{\nu}}{\nu} \tag{3.18}$$

This function (f_{v1}) becomes zero at the wall and tends to unity at high Reynolds number where $\tilde{\nu} >> \nu$. As such $\tilde{\nu}$ is equal to ν_t everywhere except in near wall (viscosity-affected) regions. The formulation ensures $\tilde{\nu}$ equals $\kappa y u_\tau$ all the way to the wall. Spalart and Allmaras recommended that closure coefficient $c_{v1} = 7.1$.

The production term of Equation 3.16 comprise the following functions and constants:

$$\tilde{S} = S + \frac{\tilde{\nu}}{\kappa^2 d^2} f_{v2}, \text{ with } f_{v2} = 1 - \frac{\chi}{1 + \chi f_{v1}} \tag{3.19}$$

Here, the wall function f_{v2} tends to unity at the wall and zero at high Reynolds number. The magnitude of vorticity, S, is defined as:

$$S = \sqrt{2\Omega_{ij}\Omega_{ij}} \tag{3.20}$$

with the mean rate-of-rotation tensor given by:

$$\Omega_{ij} = \frac{1}{2}\left(\frac{\partial \bar{u}_i}{\partial x_j} - \frac{\partial \bar{u}_j}{\partial x_i}\right) \tag{3.21}$$

The constant $c_{b1} = 0.1355$, κ is the von Kármán constant (0.41) and d is the distance to the nearest wall.

In the diffusion term of Equation 3.16 there are two constants that are yet to be defined, the turbulent Prandtl number, $\sigma = \frac{2}{3}$, and constant $c_{b2} = 0.622$.

The terms describing the dissipation of eddy viscosity in Equation 3.16 are given by:

$$f_w = g\left[\frac{1 + c_{w3}^6}{g^6 + c_{w3}^6}\right]^{1/6}, \; g = r + c_{w2}(r^6 - r), \; r = \frac{\tilde{\nu}}{\tilde{S}\kappa^2 d^2} \tag{3.22}$$

The constant $c_{w2} = 0.3$, $c_{w3} = 2$ and the remaining terms have been defined earlier.

The one-equation SA model is complete and is generally considered robust with moderate resolution requirements. It is computationally simpler and more efficient than two-equation and higher order models [63]. Although wall function constants are tuned to wall bounded aerodynamic flow applications, the model has been shown to perform well in boundary layers with adverse pressure gradients and is increasingly

used in turbomachinery applications [69]. It has been assessed to be a satisfactory choice for many engineering applications particularly, airfoil and wing applications [65]. The model does not account for the decay of ν_t in isotropic turbulence and has been shown to perform less well for free shear flows and decaying turbulence [63].

The SA model has been successfully applied to study flow pulsations in gap-connected twin-subchannel geometries similar to those in the current study [60]. In summary, the SA model is a complete and computationally efficient model with acceptable general performance and a demonstrated capability for this specific application. As such, the SA model is a reasonable choice for a base model in the current study.

3.6.3 The k-ω Model

Sensitivity of the results to a higher order turbulence model (two-equation) than the base case SA model (one-equation) has been assessed. Two-equation models solve transport equations for two turbulence quantities in addition to the RANS set of equations. As noted earlier, two-equation models are complete, provide a fuller description of the turbulence and tend to be more broadly applicable than one-equation models. However, this is achieved at the expense of computational efficiency.

Typically, two-equation models include a transport equation for turbulence kinetic energy (k) coupled with a transport equation for either the dissipation rate for k (i.e., the k-ε model) or the specific dissipation rate for k (i.e., the k-ω model). These particular two-equation models are among the most broadly applied turbulence models in commercial applications.

The basic k-ε equations do not apply within the viscous sublayer [62] and the

model is primarily recommended to be used for outer and overlap layers [64]. The near-wall performance of the k-ε model has been assessed to be unsatisfactory for boundary layers with adverse pressure gradients as compared to the k-ω model [69] and [63]. As such, the k-ω model is generally considered superior for wall bounded and low Reynolds number flows. Since the phenomena of interest in the current study are driven largely by the influence of the near-wall behaviour in the narrow gap region, the k-ω is selected for sensitivity to a higher order model.

The ANSYS CFX formulation of the k-ω model applied here follows that developed by Wilcox [70]. It solves two transport equations, one for the turbulence kinetic energy, k, and one for the turbulent frequency, ω. The stress tensor is computed from the eddy-viscosity concept, i.e.:

$$\tau_{ij} = -(\rho\overline{u_i' u_j'}) = \mu_t \left[\frac{\partial \bar{u}_i}{\partial x_j} + \frac{\partial \bar{u}_j}{\partial x_i} \right] - \frac{2}{3}\rho k \delta_{ij} \tag{3.23}$$

The eddy viscosity is linked to the turbulence kinetic energy and specific dissipation as:

$$\mu_t = \rho k/\omega \tag{3.24}$$

The turbulence kinetic energy (k) equation is given by;

$$\rho\frac{\partial k}{\partial t} + \rho U_j \frac{\partial k}{\partial x_j} = \tau_{ij}\frac{\partial U_i}{\partial x_j} - \beta'\rho k\omega + \frac{\partial}{\partial x_j}\left[(\mu + \sigma_k \mu_T)\frac{\partial k}{\partial x_j} \right] \tag{3.25}$$

and the specific dissipation rate (ω) given by:

$$\rho\frac{\partial \omega}{\partial t} + \rho U_j \frac{\partial \omega}{\partial x_j} = \alpha\tau_{ij}\frac{\partial U_i}{\partial x_j} - \beta\rho\omega^2 + \frac{\partial}{\partial x_j}\left[(\mu + \sigma_\omega \mu_T)\frac{\partial \omega}{\partial x_j} \right] \tag{3.26}$$

Closure coefficients are determined to provide agreement with experimental observations and are established as:

$$\alpha = 5/9,\ \beta = 3/40,\ \beta' = 9/100,\ \sigma_k = 1/2,\ \sigma_\omega = 1/2 \tag{3.27}$$

Auxiliary relations for dissipation and turbulence length scale are given by:

$$\varepsilon = \beta'\omega k \text{ and } l = k^{1/2}/\omega \tag{3.28}$$

3.6.4 Closing the Reynolds Averaged Scalar Transport Equation

The terms $\overline{\phi' u_i'}$ in the Reynolds averaged scalar transport equation (Equation 3.12) characterize the transport of ϕ in the x_i direction by turbulent fluctuations. As only the averaged values of ϕ and u_i are computed in RANS applications, like the Reynolds stresses, the terms $\overline{\phi' u_i'}$ in Equation 3.12 must be modeled.

An approach analogous to the Bousinesq hypothesis for the Reynolds stress terms is applied for the turbulent scalar transport terms. That is, the turbulent transport process for a passive scalar is likened to the molecular diffusion process. In the molecular process, diffusion is quantified by a diffusion coefficient and the local gradient of the scalar. The analogy for turbulent flux can then be written as:

$$\overline{\phi' u_i'} = \Gamma_{\phi t} \frac{\partial \bar{\phi}}{\partial x_i} \tag{3.29}$$

where $\Gamma_{\phi t}$ is the turbulent or eddy diffusivity coefficient for scalar ϕ. The eddy diffusivity ($\Gamma_{\phi t}$) is dimensionally equivalent to molecular diffusivity (m^2/s) but, like

the eddy viscosity, $\Gamma_{\phi t}$ is not a property of the fluid. The eddy diffusivity can also vary with geometry, flow conditions and flow history and again must be modeled.

Turbulent fluctuations drive turbulent diffusion of both momentum and of a passive scalar. Due to this common mechanism, a relationship between eddy viscosity and eddy diffusivity is typically assumed. This relationship is described by the dimensionless ratio between the kinematic eddy viscosity (ν_t) and the turbulent diffusivity ($\Gamma_{\phi t}$) in the form of a turbulent Schmidt number (Sc_t), i.e.;

$$Sc_t = \frac{\mu_t}{\rho \Gamma_{\phi t}} = \frac{\nu_t}{\Gamma_{\phi t}} \tag{3.30}$$

Reynolds (1874) postulated the turbulent Schmidt number (Sc_t) to be of the order unity due to the common driving mechanism. ANSYS CFX applies a default value of 0.9 for the turbulent Schmidt number (Sc_t) and this value is used in the current study.

Chapter 4

Methodology

4.1 Overview

A numerical study of the effects of appendages on subchannel mixing is carried out. Appendages such as those introduced by CANDU bundle end plates or bearing pads are studied. The assessment considers a symmetric, rectangular compound channel geometry connected by a single rectangular gap through the use of CFD techniques. The numerical analysis applies ANSYS CFX, a commercial CFD code, which solves the equations of motion presented in chapter 3, to predict flow fields and mixing both in the absence and presence of appendages to isolate the effect of appendages on the resultant bulk crossflow mixing.

The specific two-channel geometry considered corresponds to that used in Mahmood's detailed experimental program [2]. In this way, the base models used in the CFD calculations (without appendages) can be validated against a series of detailed measurements of flow attributes and crossflow mixing for a specific geometry (channel/gap shape and width) and a variety of inlet conditions (i.e., Reynolds numbers).

Both full test section and periodic boundary condition models are used in the CFD study. The study involves several stages in an overall systematic approach.

The first step is the development of computational models. Although full test section models are required for mixing calculations, for computational efficiency, a sub-domain of the full test section applying streamwise periodic boundary conditions was used for a series of sensitivity studies to establish reasonably converged modelling parameters such as mesh size and time step. Once determined, these parameters are applied in the computationally expensive full test-section simulations used to quantify crossflow mixing.

With modelling parameters established from the periodic simulations, a full domain model of the reference experimental test section was generated. In this model, a NaCl tracer at sufficiently low concentration was added to the inlet of one subchannel consistent with Mahmood's reference experimental procedure. This model was used to perform simulations predicting flow characteristics and total mixing along the test section. The results from these simulations are compared with experimental measurements to establish confidence in the overall model.

With a validated full test section model developed, a single appendage, representative of a CANDU bundle end plate web, was added at the center of the flow domain of the full test section model. Simulations are repeated and from the results, the influence of the appendage on flow and mixing characteristics are isolated.

4.2 Selection of Base Case Experimental Conditions

The geometry considered in the reference experimental study by Mahmood [2] consisted of two simple rectangular channels connected by a single gap. Four gap geometries were assessed by Mahmood [2], these are; rectangular gaps having widths of 2 and 3 mm and curved gaps with 2 and 3 mm widths.

From these, a rectangular gap geometry is selected for assessment in the current study as much of the previous work related to subchannel flow structures has been carried out for this type of geometry (e.g., Arvanitis [60], Home et al. [44], Meyer and Rheme [27]). In the reference study, Mahmood [2] provides detailed measurements from both the flow structure and mixing components of the experimental program for the 3 mm gap dimension. As such, the 3mm rectangular gap geometry is selected for the base case as this geometry provides the most experimental data for model validation.

The base model for this work is then a simple compound geometry with a rectangular gap as shown in Figure 4.1. The dimensions correspond to those used in the experimental programs of both Mahmood [2] and the earlier work of Lexmond et al. [3].

Figure 4.2 shows a schematic of the entire test section from Mahmood [3]. The test section is 1.5 m in length. The subchannels are connected by a gap over the central 1.1 m portion of the test section. They are not connected at the 200 mm inlet and outlet sections.

Two sets of experiments were carried out in Mahmood's [2] overall program. The

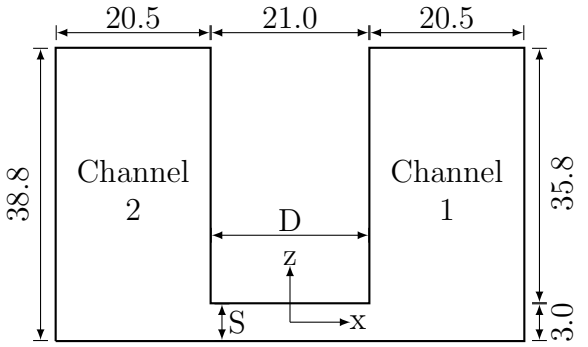

Figure 4.1: Cross-section of twin-subchannel geometry with bulk flow into the page (dimensions in mm)

first set of experiments was designed to measure instantaneous flow velocities in the stream-wise and spanwise directions through the gap mid-plane using particle image velocimetry (PIV). The second set of experiments measured the extent of mixing through the gap along the entire length of the test section by way of a measured amount of a passive scalar (NaCl) introduced into the flow.

The working fluid in the experimental program from Mahmood [2] was water at room temperature (20°C) and Reynolds numbers (based on the hydraulic diamter of full channel geometry, 0.024 m) ranging from approximately 800 to 20000. Mahmood [2] presented more experimental measurements and visualization results for the case with a Reynolds numbers of 2690. Accordingly, this flow condition is chosen as a base case for model development and assessment in the current study, supplemented by flow conditions with a Reynolds number of 7500.

4.3 Model Development and Assessments

ANSYS CFX is a commercially developed CFD software tool having broad engineering applications in design and analysis. ANSYS CFX is provided with a suitably

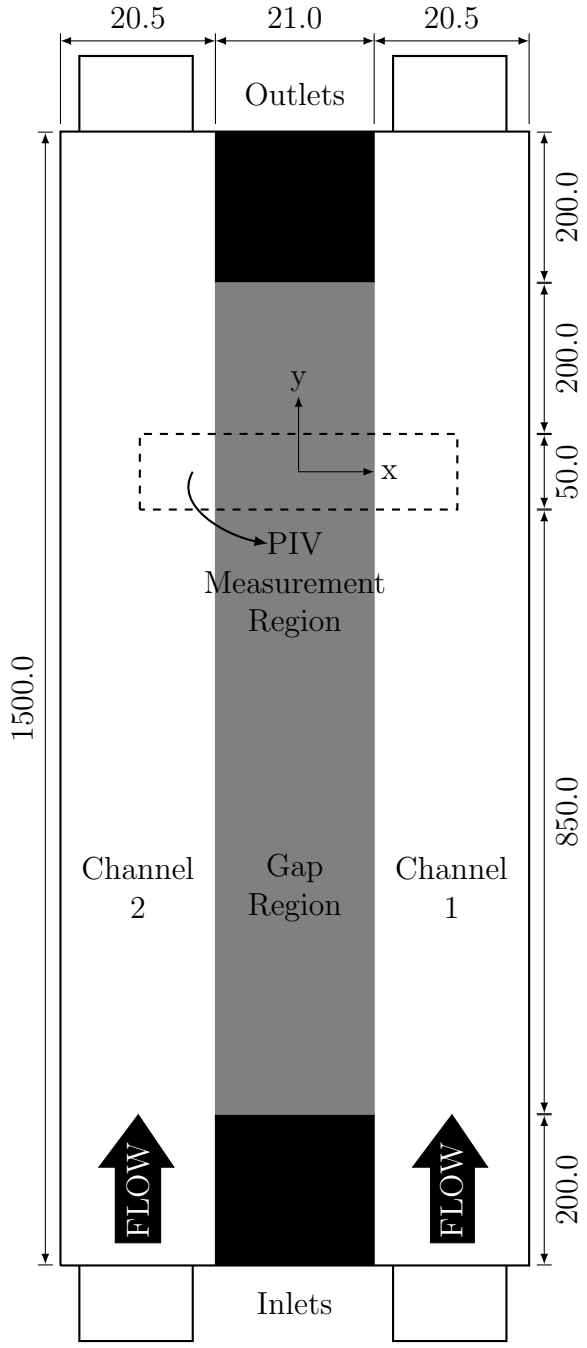

Figure 4.2: Full twin-subchannel test section

meshed representation of the flow domain of interest along with initial and boundary conditions and modelling assumptions appropriate for the specific problem and required output. According to these inputs supplied to ANSYS CFX, the Navier-Stokes equations, as described in Section 3, are discretized over the control volumes defined by the mesh and solved numerically. This is characterized as a finite volume approach.

The inputs for the two models of the base case experimental configuration (streamwise periodic and full test section) are developed in the following sections.

4.3.1 Streamwise Periodic Boundary Condition Models and Sensitivity Assessment

In the streamwise periodic boundary condition technique, flow conditions are cycled through the domain, wrapped around from outlet to inlet, until a converged solution is obtained within the domain. This approach eliminates the development region from the solution and allows for a shorter solution domain. These simulations are computationally more efficient for performing sensitivity studies as solutions converge more readily than with a full test section model having a similarly refined mesh.

The purpose of the sensitivity simulations is to assess convergence of the model in regards to mesh size (spatial), time step (temporal), as well as sensitivity to turbulence model (Spalart-Allmaras and k-ω). In addition, an initial sensitivity assessment considering periodic domain length is carried out to ensure the periodic models are converged in regards to this parameter.

Three streamwise periodic domain model meshes were developed for the sensitivity study as follows;

1. A reference model representing a 300 mm portion of the reference twin-subchannel test section from Mahmood [2].

2. A domain length sensitivity model representing a 550 mm portion of the reference twin-subchannel test section having a mesh consistent with the reference model.

3. A spatial convergence model having identical dimensions to the reference model containing a finer mesh.

Complete details of the solution domain, mesh generation, and solution scheme for the periodic models are presented in the next section.

As discussed in Section 3, Spalart-Allmaras (SA) is a practical and accurate option for most turbulent-flow applications [65]. Arvanitis [60] performed CFD simulations, including a turbulence model sensitivity assessment, investigating flow pulsations in a twin-subchannel geometry similar to the one considered in the current study. Arvanitis [60] reported that the SA turbulence model coupled with a second order accurate in space advection scheme for the equations of continuity and momentum performed best in regard to prediction of the dynamics of flow structures and peak frequency spectra. Due to its performance and practicality, the SA model with a second order accurate advection scheme is applied in the reference periodic model in the current study.

The flow boundary conditions for all sensitivity cases are consistent with the base case experimental conditions of water at 20^{o}C and a Reynolds numbers of 2690. The reference sensitivity case simulation applies the reference periodic model, the Spalart-Allmaras turbulence model with a time step of 1 ms. Each subsequent case

is simulated with a single parameter altered from the reference sensitivity case. All simulations are run for 100,000 time steps with the exception of the time step convergence case which was run with a 0.5 ms time step for 200,000 total time steps. The case matrix for periodic boundary condition sensitivity simulations is shown in Table 4.1.

Table 4.1: Periodic boundary condition sensitivity case matrix

Run	Type	Appendage	Domain Length (mm)	Turbulence Model	Time Step (ms)	Nodes (× million)	Total Time Steps	Re	Comment
1	Periodic	No	300	SA	1	2.2	100 000	2690	Base case
2	Periodic	No	550	SA	1	4.0	100 000	2690	Domain length sensitivity
3	Periodic	No	300	SA	1	6.0	100 000	2690	Spatial convergence
4	Periodic	No	300	SA	0.5	2.2	200 000	2690	Time step convergence
5	Periodic	No	300	k-ω	1	2.2	100 000	2690	Turbulence model sensitivity

Mesh Generation and Solution Scheme - Periodic Models

All models for this study have a geometry consistent with that used in experimental studies by both Mahmood [2] and Lexmond et al. [3]. They consist of two vertical rectangular ducts connected by a near wall gap region. The test section (known as R-3) has a rectangular gap, with gap depth (D) of 21.0 mm and gap spacing (S) of 3.0 mm, connecting two identical rectangular subchannels (20.5 mm x 38.8 mm) as shown in Figure 4.1. Mahmood reported that the flow area and gap spacing were based on typical LWR core subchannel dimensions.

Figures 4.1 and 4.2 also show the coordinate system applied in all models for this study. The streamwise (axial) flow is in the y-direction, the cross-stream (spanwise) direction is labelled x and the gap wall normal direction z.

The ANSYS CFX code uses finite volume discretization with a fully implicit time

advancement scheme. For all computations presented here, the time discretization was carried out using the second-order backward Euler scheme.

Wall models are recommended for most high Reynolds number applications, i.e., Re>10^6, where it is computationally expensive to resolve the viscous sublayer. The SA and k-ω models are applicable throughout the boundary layer provided a sufficiently refined mesh is used near the wall [71]. Due to the range of Reynolds numbers considered (Re<10^4) and in the interest of resolving near wall detail for the benchmark simulations, the SA turbulence model without wall models is selected for the reference periodic assessment.

In the absence of wall models, it is recommended that the first wall adjacent cell be located within the viscous sublayer ($y^+ \approx 1$) [65]. Complying with this condition imposes a fine mesh requirement on the solution domain.

Derksen [61] performed a domain length sensitivity assessment for a periodic boundary condition model of identical cross-section to that used in the current study. Domain lengths containing four and eight structures were considered. Derksen [61] concluded that the shorter (four structure) domain adequately captured the flow details. Mahmood [2] reported that, although any two consecutive structures may differ in length by a factor of 2, the average structure length was practically Reynolds number independent above Re = 2000 for a given channel geometry. For the reference geometry used here, Mahmood [2] observed an average structure length of approximately 73 mm. Accordingly, for the current study, a reference sensitivity model with a 300 mm domain length (equal to approximately four average structure lengths) is used.

With the domain length established, the reference model representing a 300 mm

portion of the twin-subchannel test section was prepared. A structured grid was generated with a uniform distribution of mesh points in the streamwise (y) direction. The mesh in the x and z directions of the subchannels have an expanding or non-uniform structure, inflating further from the walls. The first grid element in the x and z directions are located at $y^+ \approx 1$. The mesh in the x and z directions through the gap is uniform and fixed at the finest corresponding coordinate near wall value. This scheme is designed to capture flow detail in the gap and all near wall regions with a relatively fine mesh. The reference domain and mesh described above is labelled M_1, having a total of approximately 2.2×10^6 nodes. A cross-sectional view of this mesh is shown in Figure 4.3.

An additional 300 mm domain length periodic mesh was generated to assess spatial convergence. This mesh contained a total of approximately 6.0×10^6 nodes and is labelled M_2. A third mesh to assess domain length sensitivity for periodicity effects was also generated (M_3). The domain length for this model is 550 mm and the mesh spacing in all dimensions is identical to the reference mesh (M_1). The total number of nodes for this mesh is approximately 4.0×10^6. Table 4.2 shows the distribution of nodes in the x, y and z directions through the subchannel and gap regions of the domain.

Table 4.2: Periodic model mesh details

Mesh	M_1		M_2		M_3	
	Nodes	Cells	Nodes	Cells	Nodes	Cells
X_{sub}	61	60	76	75	61	60
Y_{sub}	151	150	301	300	276	275
Z_{sub}	91	90	91	90	91	90
X_{gap}	106	105	141	140	106	105
Y_{gap}	151	150	301	300	276	275
Z_{gap}	16	15	21	20	16	15
Total	2 203 996	2 126 250	5 957 091	5 790 000	4 028 496	3 898 125

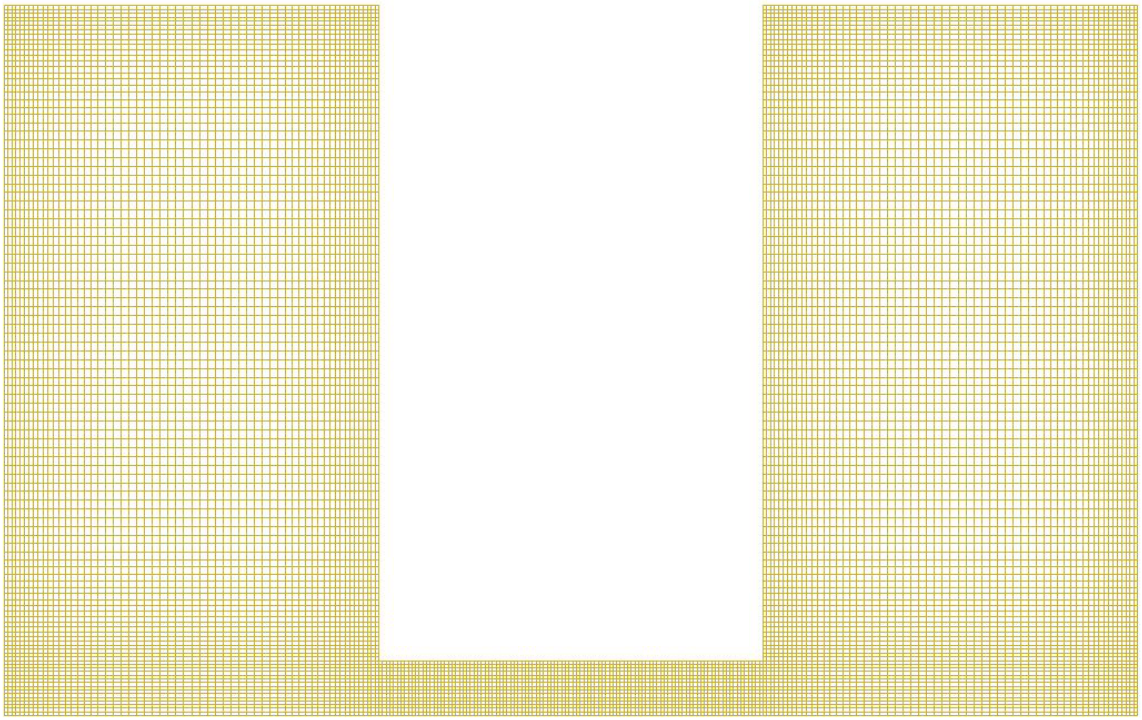

Figure 4.3: Cross section for mesh M_1

For the reference mesh and base case flow conditions with a 1 ms time step, the Courant-Friedrichs-Lewy condition is satisfied with $C_{max}<1.0$. Implicit solvers, as used here, are less sensitive to numerical instability than explicit solvers and can tolerate values of $C_{max}>1.0$. As such, the 1 ms time step is considered appropriate to ensure convergence for this application. Sensitivity to a smaller time step is also part of the overall assessment.

4.3.2 Full Test Section Model and Mixing Calculations

Mixing calculations without appendages are carried out with a model representing the full test section used in the reference experimental study [2]. In the reference experiments, inter-subchannel mixing was determined by the introduction of a measured volume of a NaCl solution at the inlet to one of the subchannels. The concentration of the NaCl solution was sufficiently low that it behaved as a passive scalar within the flow. Calibrated impedance measuring sensors at the outlets of each subchannel were used to establish the exiting NaCl concentrations and hence the extent of mixing over the length of the test section.

Similarly, in the full test section model, a scalar variable was added to the flow in one subchannel to simulate the NaCl tracer. The scalar variable is a non-reacting scalar component transported through the flow with no direct influence on the flow solution thereby behaving as a passive scalar. Scalar variable material properties, boundary conditions, sources, and sinks are defined by the user and they are subsequently distributed through the flow field by way of advection and diffusion through the scalar transport equation.

The kinematic diffusivity (the fluid property quantifying molecular diffusion) of

salt in water is very low (on the order of 10^{-9} m^2/s). As such, in turbulent flows, the diffusion processes are dominated by turbulent diffusion. Although molecular diffusion may be neglected for the current study, a representative value for the kinematic diffusivity of salt in water (1.3×10^{-9} m^2/s) is applied in the simulations.

The default turbulent flux closure model for the scalar variable, governed by the transport equation, is applied in the simulations. This comprises the Eddy Diffusivity model with the turbulent Schmidt number set to a value of 0.9 as discussed in Section 3.6.4.

In the full test section simulations, it is assumed that the concentration of sodium chloride at the inlet of channel 1 is uniform across the inlet boundary as the tracer would develop toward a uniform distribution through the 500 cm section from the injection point to the test section inlet.

Following the conclusions of the sensitivity assessment (see Appendix A), computations are carried out for the entire experimental domain applying the Spalart-Allmaras turbulence model with a time step of 1 ms.

A uniform velocity profile (Re = 2690 or 7500) was applied at the inlet to the test-section consistent with the numerical modelling component of the reference study [2], in which a plug flow boundary condition was assumed. The 200 mm inlet section provides a development length of approximately 8.3 hydraulic diameters upstream of the gap-connected region. The exit boundary condition is set to atmospheric pressure.

Boundary conditions that are consistent with the reference experiments [2] are applied, i.e., water at 20°C with Reynolds numbers of 2690 and 7500. Table 4.3 shows the case matrix for the full test section mixing calculations, where run type 'a' allows the tracer to reach a fully developed state along the length of the test section

and 'b' the final run where data is collected.

Table 4.3: Full test section model for mixing calculations case matrix

Run	Type	Appendage	Domain Length (mm)	Turbulence Model	Time Step (ms)	Nodes (× million)	Total Time Steps	Re	Comment
6a	Full	No	1500	SA	1	13.0	30 000	2690	Set-up run with tracer
6b	Full	No	1500	SA	1	13.0	10 000	2690	Final run
7a	Full	No	1500	SA	1	13.0	30 000	7500	Set-up run with tracer
7b	Full	No	1500	SA	1	13.0	10 000	7500	Final run

Complete details of the mesh generation and solution scheme for the full test section are presented in the following section.

Mesh Generation and Solution Scheme - Full Test Section Model

Figures 4.1 and 4.2 show detailed axial and cross-sectional views of the test section from Mahmood [2] along with the coordinate system applied in the simulations. The entire test section is 1.5 m in length. The subchannels are connected by a gap over the central 1.1 m portion and are not connected at the 200 mm inlet and outlet sections. The entire test section is modelled for mixing calculations.

The rationale applied to establish the mesh details for the full test section model is identical to that applied for the reference periodic model. That is; capturing the gap and near-wall flow detail with a finer mesh ($y^+ \approx 1$) as opposed to using wall models. According to the results of the sensitivity assessment (see Appendix A), the mesh details in the x and z directions for the full test section model are identical to the reference periodic model (see Figure 4.3).

The gap design includes an abrupt flow area change at both the inlet and outlet of the gap-connected portion of the test section. Local entrance and exit effects may influence total mixing between the subchannels. In order to capture relevant detail

at the entrance and exit of the gap-connected region, a finer mesh is applied both upstream and downstream in the axial (y) direction, inflating in both directions from the entrance and exit planes. Table 4.4 shows the distribution of nodes in the x, y and z directions for the mesh generated for the full test section model, including the subchannel, gap, inlet and outlet regions of the domain.

Table 4.4: Full test section mesh details

Mesh	M_{1-1500}	
	Nodes	Cells
X_{sub}	61	60
Y_{inlet}	141	140
Y_{outlet}	141	140
$Y_{channel}$	631	630
Z_{sub}	91	90
X_{gap}	106	105
Z_{gap}	16	15
Total	12 988 478	12 458 250

4.3.3 Full Test Section Appendage Model and Mixing Calculations

Flow oscillations through the gap are the dominant contributors to crossflow mixing in connected compound subchannels. With the introduction of an appendage in the gap region, there will be two main sources of gap flow oscillations; those induced by the gap geometry and those induced by vortex shedding around the appendage. It is assumed that maintaining a similar ratio of gap-induced to appendage-induced vortex frequencies in the numerical model derived from Mahmood's experiment and the CANDU channel will provide comparable relative contributions to total mixing between the two phenomena in both geometries.

The frequency of flow oscillations can be presented in dimensionless form as the Strouhal number using appropriate length and velocity scales. The Strouhal (St) number is defined as;

$$St = fD/U \tag{4.1}$$

where D is the system characteristic length, U the characteristic velocity and f the peak frequency of the power spectrum of the spanwise velocity at the gap center.

Considering first the gap induced oscillations; Chang and Tavoularis (2007) point out that the hydraulic diameter (D_h) for a CANDU channel (or the twin-subchannel geometry) is dominated by the characteristics of the subchannel regions as opposed to the gaps. Since the oscillations of interest are associated with phenomena within the gap, they propose the fuel rod diameter (defining gap depth (D)), as an appropriate length scale. This convention will be applied in the following.

Chang and Tavoularis (2007) state that a variety of velocity scales have been used to quantify Strouhal number (e.g., bulk velocity, average friction velocity, average gap velocity). They point out that for suitably turbulent flow; these scales would be proportional to one another and as such, which is chosen is immaterial as only the value of the Strouhal number would be affected and not its sensitivity to other flow parameters. For the current calculations, the bulk velocity is selected for the velocity scale as its value is readily available in the CANDU bundle geometry and in the experiments for comparison and scaling purposes.

In order to establish appendage dimensions to incorporate into the reference experimental geometry that are representative of a CANDU bundle end plate, the process outlined below is followed;

1. Establish the bulk velocity in a CANDU channel with the same fluid properties and Reynolds number as the base case experiment.

2. Estimate the frequency of gap flow oscillations arising from the flow conditions identified in 1) coupled with the gap geometry in the CANDU channel.

3. Determine the frequency of flow oscillations arising from the flow and gap geometry in the base case experiment.

4. Estimate the frequency of vortex shedding from end plate webs in the CANDU channel under the same flow conditions.

5. Determine the appendage induced vortex shedding frequency for the experimental geometry required to maintain a consistent ratio of frequencies between the CANDU channel and the base case experiment.

6. Use this frequency to establish appendage dimensions for the experimental geometry by way of the Strouhal number.

CANDU Equivalent Bulk Velocity

The geometry and flow conditions from the reference experimental conditions (Mahmood [2]) correspond to a Reynolds number of 2690 (hydraulic diameter $D_h = 0.0242$ m, bulk velocity $U_b = 0.111$ m/s, density $\rho = 998.2$ kg/m^3, viscosity $\mu = 0.001002$ kg/m·s). For the same Reynolds number in a CANDU channel, with $D_h = 0.0076$ m, $\rho = 998.2$ kg/m^3, $\mu = 0.001002$ kg/m·s, the bulk velocity is determined as 0.355 m/s.

Gap Flow Oscillation Frequency (Strouhal Number) - CANDU Channel

Chang and Tavoularis (2008) reported Strouhal numbers associated with coherent structures in various rod geometries corresponding to a variety of ratios of gap spacing (S) to rod diameter (or gap depth), D. If the gap depth for a CANDU subchannel is considered to be the fuel element diameter (0.01307 m) and the gap spacing to be the minimum spacing between two adjacent fuel element surfaces (0.00181 m) the ratio of gap spacing to depth (S/D) is 0.00181/0.01307 or S/D = 0.1385.

For a range of S/D ratios (0.01 to 0.126), Chang and Tavoularis (2008) report experimentally determined Strouhal numbers from various investigators. The highest value of S/D for which a Strouhal number is identified is S/D = 0.126, which approaches that in the CANDU gap geometry considered here (0.1385). The Strouhal number for this geometry is approximately 0.2.

For a Strouhal number of 0.2, a bulk velocity of 0.3553 m/s, a gap depth of 0.01307 m, the fluctuation frequency associated with the gap in the CANDU channel is determined from Equation 4.1 as 5.44 Hz.

Gap Flow Oscillation Frequency (Strouhal Number) - Base Case Experimental Conditions

The gap size (S) for the experimental geometry of Mahmood [2] is 3 mm with a gap depth (D) of 21 mm yielding S/D = 0.1428. This value is close to the CANDU value of 0.1385 determined above. As such, from a gap frequency perspective, the two geometries are similar. Again, the highest value of S/D for which Chang and Tavoularis (2008) reported an experimentally determined Strouhal number is S/D = 0.126 for which a Strouhal number of approximately 0.2 is identified. This value

is applied for the experimental geometry, i.e., for a Strouhal number of 0.2, a bulk velocity of 0.111 m/s, a gap depth of 0.021 m, the fluctuation frequency associated with the gap in Mahmood's geometry is determined to be approximately 1.057 Hz.

Vortex Shedding from End Plate Webs - CANDU Channel

In this study, end plate webs are treated as rectangular bluff bodies in a free-stream flow. The frequency at which vortices shed from a rectangular body under these conditions is given again by Equation 4.1, Naudascher and Rockwell [72]. Where St is the Strouhal number, U is the upstream velocity, and D the characteristic length dimension. For these applications, the characteristic length is the cross-sectional width of the bluff body transverse to the flow (d). For rectangular cross-section bodies, the Strouhal number is determined as a function of; the aspect ratio, i.e., the body dimension in the streamwise direction (e) divided by the cross-section width transverse to the flow (d), the angle of incidence and the corner geometry. For an end plate web in a CANDU bundle, the length (e) is 1.52 mm and the width is (d) 4.55 mm yielding an aspect ratio of 0.334. From Naudascher and Rockwell [72], page 130 Figure 6.20, for this configuration (angle of incidence of 0.0 and non-rounded corners) the Strouhal number is approximately 0.13. From Equation 4.1, with St = 0.13, d = 0.00455 m, assuming U = U_b = 0.355 m/s the frequency for vortex shedding from an end plate web is then determined as 10.14 Hz for a CANDU channel.

Vortex Shedding Frequency from End Plate Webs - Mahmood Geometry

The ratio of flow oscillations induced by the gap to those induced by vortex shedding from the end plate webs in a CANDU channel with Reynolds number of 2690 is

then 5.44/10.14 or 0.536. It is assumed that maintaining a similar ratio of gap to web vortex frequencies in the numerical model of Mahmood's experiment will provide comparable contributions to mixing between the two phenomena. As such, the webs to be added to the model of Mahmood's experiment should be constructed to give a vortex shedding frequency of 1.057/0.536 = 1.972 Hz

Appendage Dimensions - Mahmood Geometry

Assuming the same aspect ratio (and hence Strouhal number, 0.13) for webs in a CANDU channel and the current numerical assessment of interconnected subchannels; the appendage width (d) to be added in Mahmood's mixing model is determined from Equation 4.1 with St = 0.13, U = U_b = 0.111 m/s and f = 1.972 Hz as d = 0.00731 m or 7.31 mm. Maintaining the same aspect ratio of 0.334 as in the CANDU channel yields a web length in the flow direction of 7.31 × 0.334 or 2.44 mm.

It should be noted that, given the similarities between the CANDU and experimental gap geometries (S/D), and the associated Strouhal number, the resultant appendage dimensions scale directly from the ratio of gap depths (D).

The full test section appendage model is then developed directly from the full test section mixing model described above. An appendage, representing a typical end plate type obstruction (7.31 mm wide, 2.44 mm deep, 3 mm high) is added in the gap region of the numerical models at the test section center as shown in Figures 4.4 and 4.5. This is at a distance sufficiently downstream of the gap entrance that the oscillatory flow is well established.

All other considerations are identical to the full test section mixing calculations described above (e.g., addition of scalar to measure mixing, turbulence model, initial

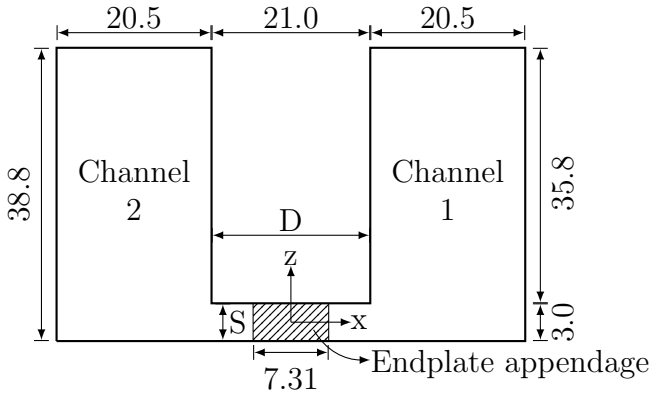

Figure 4.4: Cross-section of twin-subchannel geometry with appendage

and boundary conditions). Table 4.5 shows the case matrix for the full test appendage model mixing calculations, where run type 'a' allows the tracer to reach a fully developed state along the length of the test section and 'b' the final fun where data is collected.

Table 4.5: Full test section with appendage model case matrix

Run	Type	Appendage	Domain Length (mm)	Turbulence Model	Time Step (ms)	Nodes (× million)	Total Time Steps	Re	Comment
8a	Full	Yes	1500	SA	1	14.0	30 000	2690	Set-up run with tracer
8b	Full	Yes	1500	SA	1	14.0	10 000	2690	Final run
9a	Full	Yes	1500	SA	1	14.0	30 000	7500	Set-up run with tracer
9a	Full	Yes	1500	SA	1	14.0	10 000	7500	Final run

Complete details of the mesh generation and solution scheme for the full test section appendage model are presented in the following section.

Mesh Generation and Solution Scheme - Full Test Section Appendage Model

Figures 4.4 and 4.5 show detailed axial and cross-sectional views of the test section from Mahmood [2] with the addition of the end plate appendage at the center of the

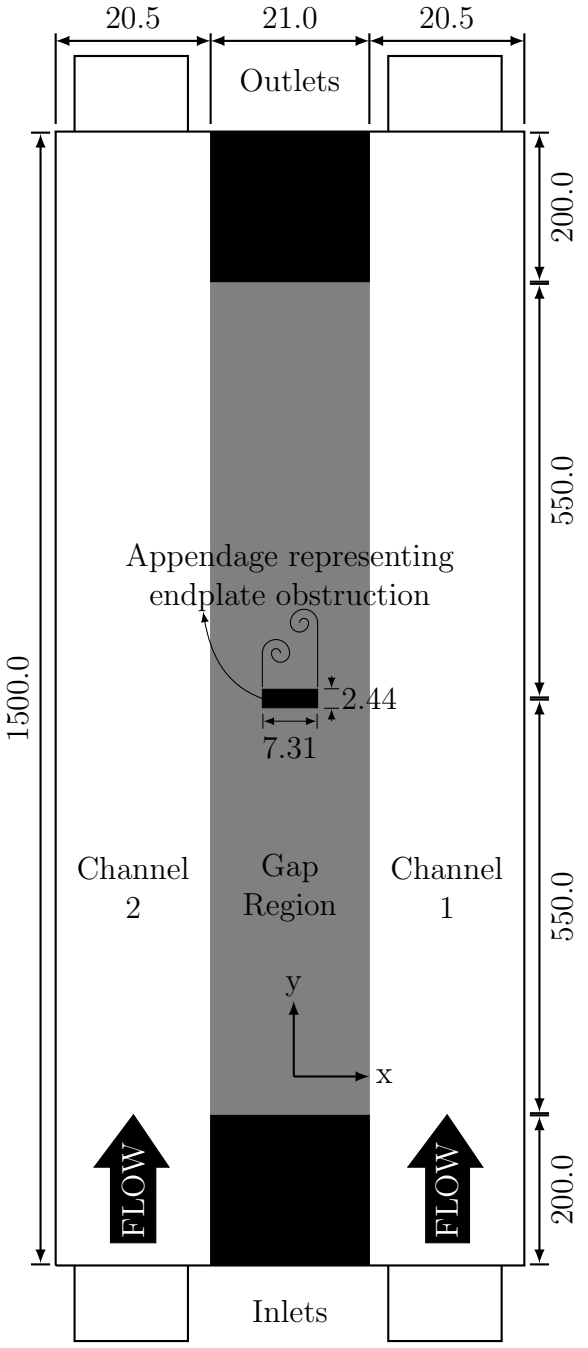

Figure 4.5: Full twin-subchannel test section with appendage

channel. The entire test section is modelled for the end plate mixing calculations.

The rationale applied to establish the mesh details for the full test section appendage model is identical to that applied for the full test section model. Accordingly, the mesh details in the x and z directions for the full test section appendage model are identical to the reference periodic model (see Figure 4.3).

As discussed earlier, the gap design represents an abrupt flow area change at both the inlet and outlet of the gap-connected portion of the test section. A finer mesh is applied both upstream and downstream in the axial (y) direction, inflating in both directions from the entrance/exit plane for the full test section mixing model. This is also true in the near-wall end plate region of the appendage model. As such, a finer mesh is applied inflating from both the upstream and downstream planes of the end plate obstruction.

Table 4.6 shows the distribution of nodes in the x, y and z directions for the mesh generated for the full test section model with the end plate appendage, including the subchannel, gap, inlet and outlet regions of the domain. Note the end plate obstruction present in the gap subtracts a meshing area that is equal to 43×13×15 = 8385 cells.

Table 4.6: Full test section with appendage mesh details

Mesh	$M_{1-1500\_endplate}$	
	Nodes	Cells
X_{sub}	61	60
Y_{inlet}	141	140
Y_{outlet}	141	140
$Y_{channel}$	710	709
Z_{sub}	91	90
X_{gap}	114	113
Z_{gap}	16	15
Total	14 066 935	13 654 770

The solution scheme and time step considerations are as described for the corresponding full test section mixing model.

Chapter 5

Results

5.1 Overview

This chapter presents the results and analysis from simulations of turbulent flow in a gap-connected twin-subchannel geometry. The specific model geometry considered represents the full test section used in the detailed experimental programs documented by Mahmood [2] and Lexmond et al. [3]. Boundary conditions consistent with the experimental procedure at two Reynolds numbers are applied in the numerical study. Simulations both with and without an added appendage are examined to isolate the effect of the appendage on flow structures and mixing.

5.2 Full Test Section Model Without Appendage

Results presented here are from the full test section simulations, without an appendage, and are analyzed in terms of turbulent structures and mixing within the flow field. The numerical results are compared with the experimental datasets of

Mahmood [2] and Lexmond et al. [3]. Structure length, axial velocity distributions, crossflow velocity fluctuations, power spectral density functions and inter-subchannel mixing are compared with available data.

5.2.1 Periodic Structure Length

Figures 5.1 and 5.2 show instantaneous crossflow (x-directed) velocity contours through the gap mid-plane for Reynolds numbers of 2690 and 7500 respectively. These represent a snapshot of the fully developed full test section results with the colour and shade of the zones indicating crossflow velocity direction and magnitude according to the legend provided. Alternating crossflow zones through the gap are clearly present in both figures.

A single flow structure can be defined by two consecutive crossflow zones through the gap, one in each direction [2]. After a development length of approximately 500 mm, the structures are very uniform in size (see Figures 5.1 and 5.2). This was also found in the unsteady RANS simulations of Arvanitis [60] and is in contrast to the LES/DES simulations of Home et al. [44]. The average structure length for structures located sufficiently distant from the ends of the channel to minimize entrance and exit effects (shown boxed in Figures 5.1 and 5.2) for Reynolds numbers of 2690 and 7500 are 73 mm and 70 mm respectively. Structure length is reasonably constant between the two Reynolds numbers.

Figure 5.3 shows the experimentally measured structure length from Mahmood [2] and Lexmond et al. [3] as a function of Reynolds number. Lexmond et al. [3] report the standard deviation of measured structure size to be 20-25% for Reynolds numbers over 2000. The results from the current numerical study are also shown in

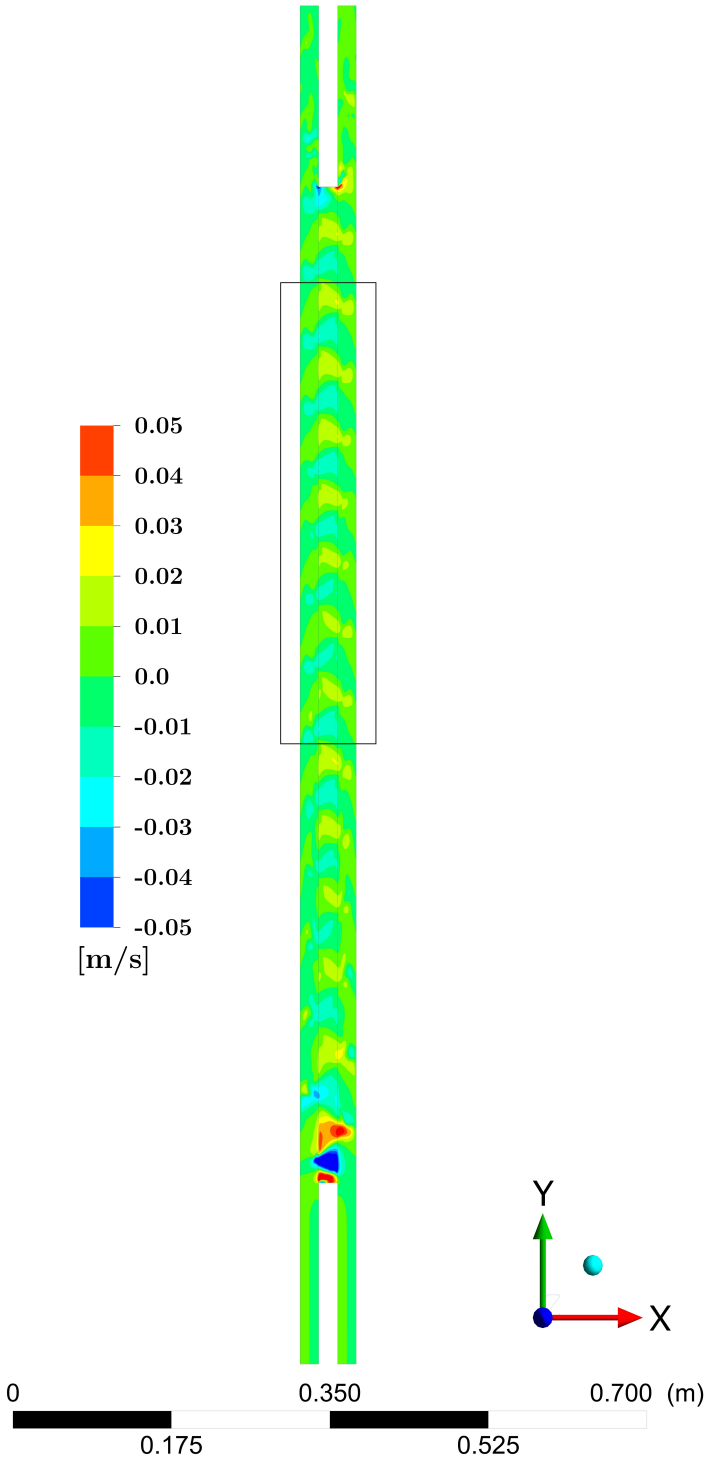

Figure 5.1: Sample of fully developed, full test section crossflow (x-directed) velocity contours through the gap mid-plane, Re = 2690, t = 40 seconds. Box denotes area where structure length is calculated.

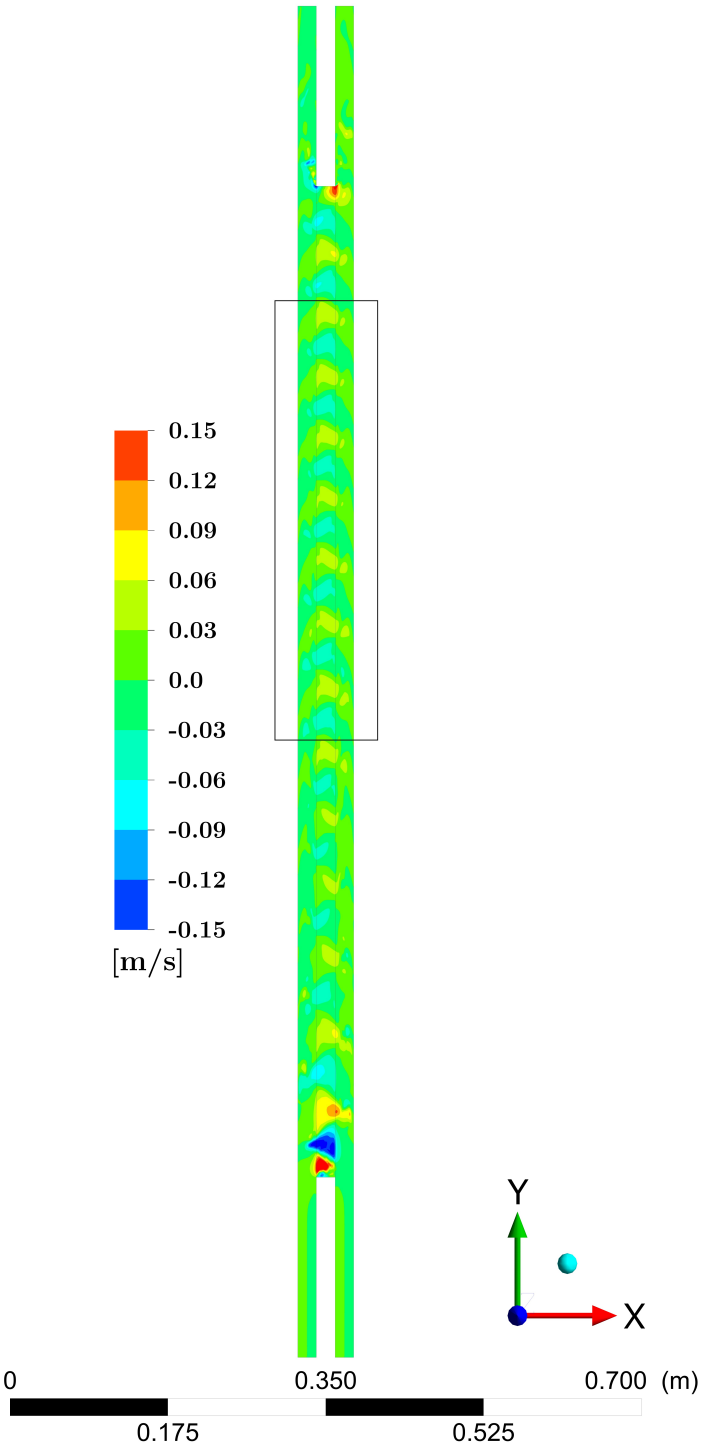

Figure 5.2: Sample of fully developed, full test section crossflow (x-directed) velocity contours through the gap mid-plane, Re = 7500, t = 40 seconds. Box denotes area where structure length is calculated.

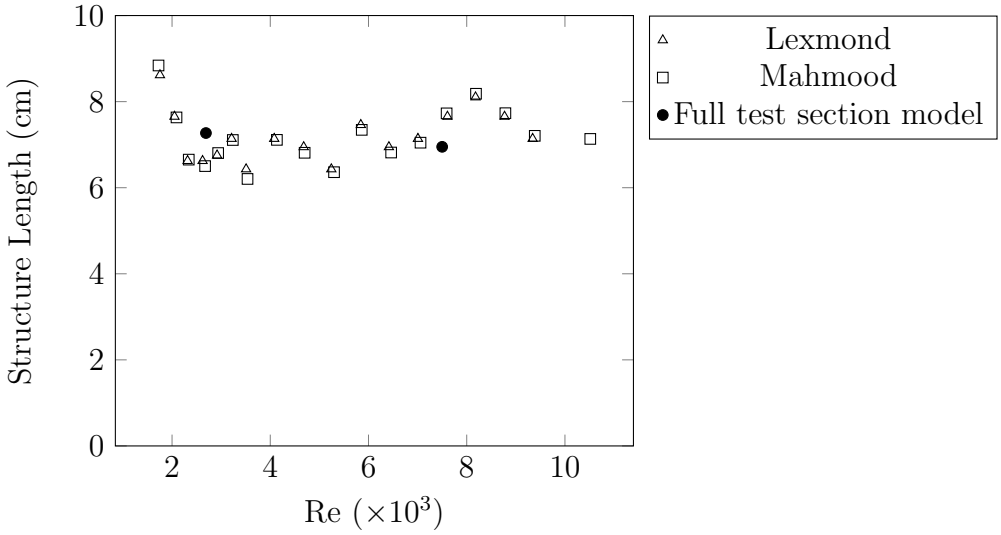

Figure 5.3: Structure length versus Reynolds number.

Figure 5.3. Very good agreement in regards to structure length is obtained between the CFD model and both experimental studies, which also show structure length to be independent of Reynolds number above Re $\approx$ 2000.

5.2.2 Axial Velocity Profiles

Time-averaged axial velocity profiles through the gap mid-plane for Reynolds numbers of 2690 and 7500 are shown in Figures 5.4 and 5.5 respectively along with corresponding experimental measurements from Mahmood [2] and Lexmond et al. [3]. The results reported by Mahmood [2] and Lexmond et al. [3] differ substantially at a Reynolds number of 2690. Agreement of the CFD results with the measurements of Mahmood is very good at Re = 2690 with a slight over-prediction of the gap-center velocity.

Overall, reasonable agreement is obtained between the experimental measurements and the CFD simulations, particularly those of Mahmood [2]. It should be

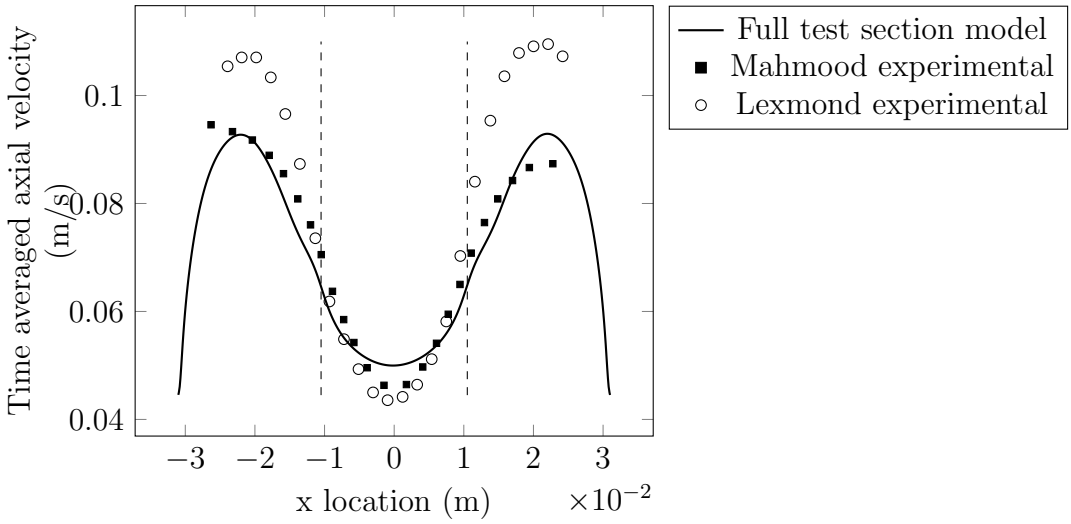

Figure 5.4: Time averaged axial velocity profile through the gap mid-plane, Re = 2690. Dashed line shows gap edge location.

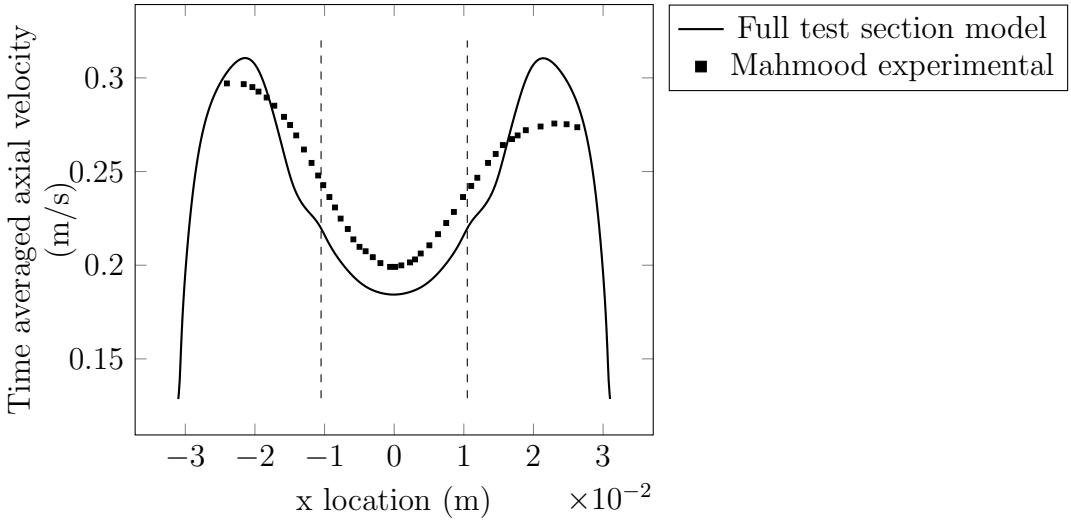

Figure 5.5: Time averaged axial velocity profile through the gap mid-plane, Re = 7500. Dashed line shows gap edge location.

noted that the asymmetries in measured peak subchannel velocities from Mahmood [2] were attributed by Mahmood to an erroneous experimental procedure which was corrected for subsequent runs including the mixing related experiments discussed in Section 5.2.5.

5.2.3 Crossflow Velocity Time Traces

Both Mahmood [2] and Lexmond et al. [3] presented measured crossflow velocities at the gap center and midplane for a Reynolds number of 2690. A sample of those measured results are shown in Figure 5.6 together with the corresponding CFD results. The experimental results show quasi-periodic behaviour, with velocity fluctuations centered on a value of zero. The CFD results show a very regular and periodic trace around a value of zero. The peak-to-peak amplitude of the CFD fluctuations agree very well with measurements.

No time series experimental results for gap center and midplane crossflow velocity are available for a Reynolds number of 7500. Figure 5.7 shows the CFD results for this case. Again, very regular and periodic behaviour is demonstrated at a notably higher frequency and peak crossflow velocity as compared to the Re = 2690 case. The peak-to-peak amplitude of the crossflow velocity at Re = 7500 is approximately double that at Re = 2690.

Mahmood [2] and Lexmond et al. [3] reported experimental measurements for the RMS crossflow velocity at the gap center as a percentage of the bulk flow velocity for a range of Reynolds numbers. Figure 5.8 shows the experimental results combined with CFD results from this study. Both the magnitudes of the RMS velocities and the slight decrease with increasing Reynolds number agree reasonably well with experimental

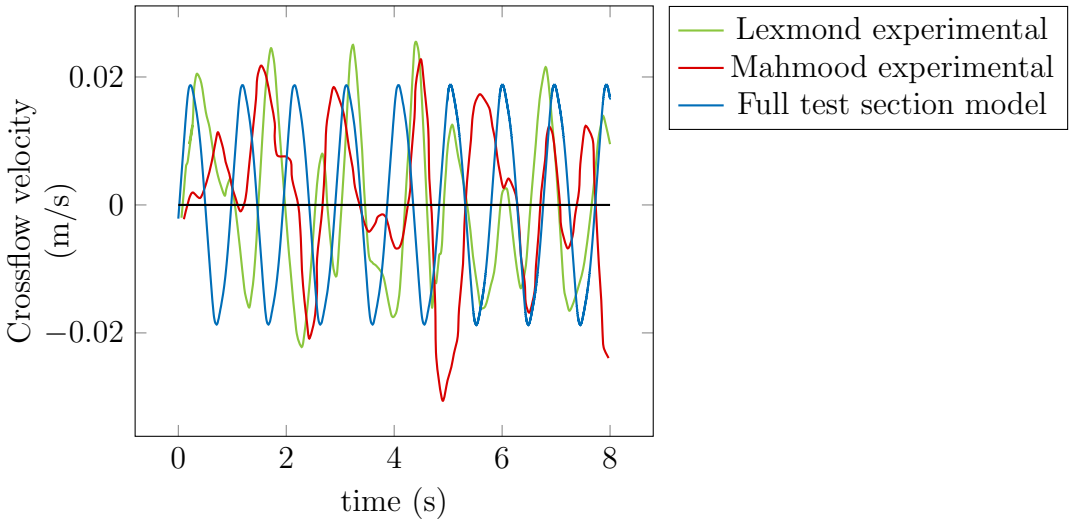

Figure 5.6: Crossflow velocity through the gap center and mid-plane, Re = 2690.

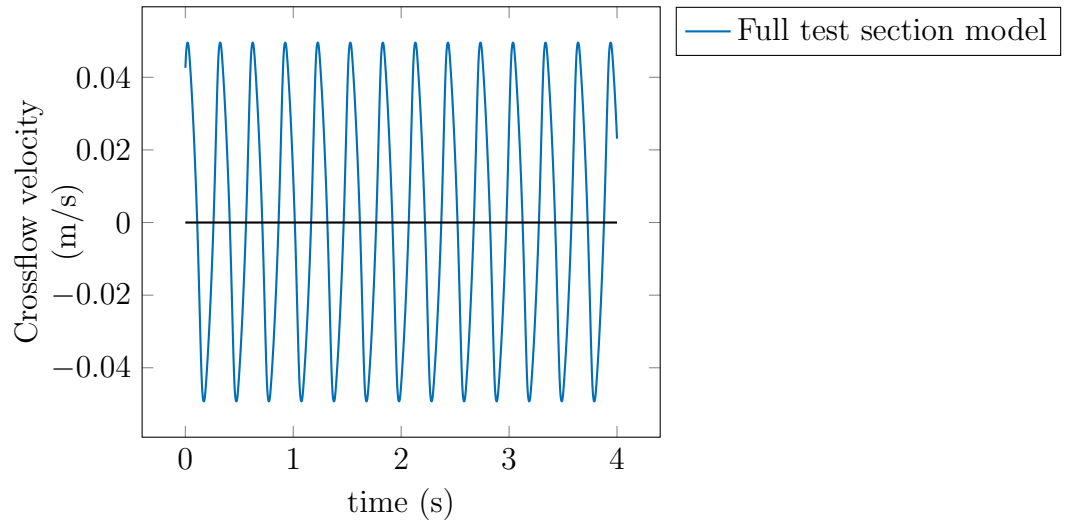

Figure 5.7: Crossflow velocity through the gap center and mid-plane, Re = 7500.

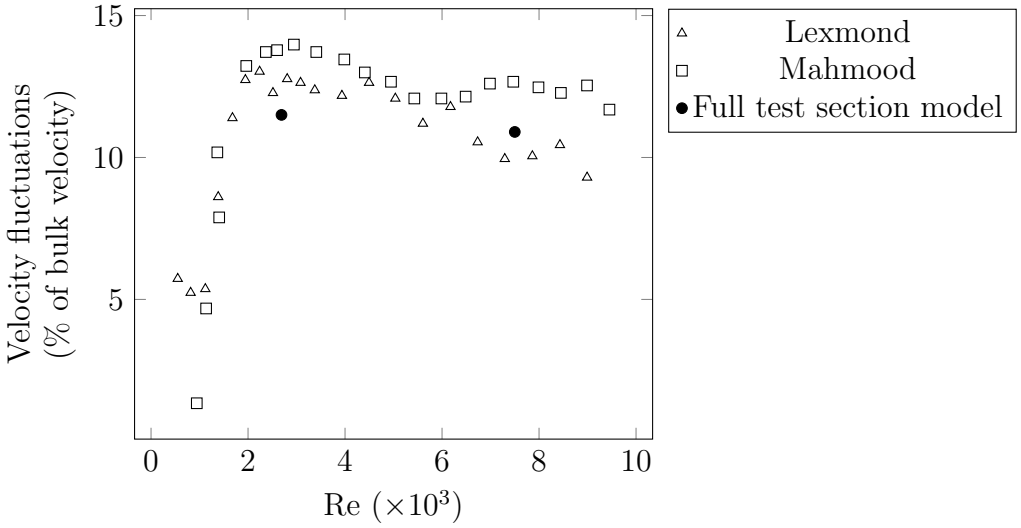

Figure 5.8: RMS crossflow velocity at the gap center and mid-plane as a percentage of the bulk flow velocity.

measurements.

5.2.4 Crossflow Power Spectral Density Functions

As discussed above, time traces of the crossflow velocity at the gap center and mid-plane from the CFD simulations showed periodic behaviour, indicating the presence of large-scale periodic structures in the flow. The dominant frequencies of the flow structures can be extracted from the corresponding frequency spectra. The frequency spectra of crossflow velocities were obtained by implementing an FFT script in MATLAB over a 10 second interval once the flow became fully developed.

Figure 5.9 shows the frequency spectrum of crossflow velocity at the gap center and midplane at various axial locations along the test section for a Reynolds number of 2690. A very distinct peak at a frequency of 1.0 Hz is obtained at all axial locations. Lexmond et al. [3] reports measured crossflow velocities in the fully developed region

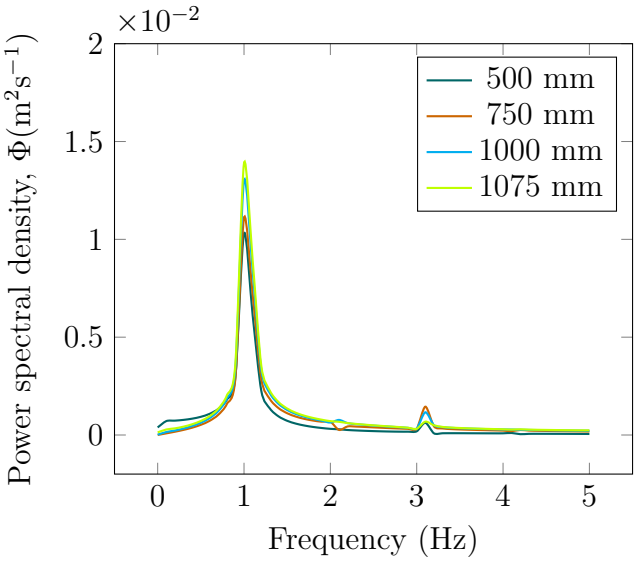

Figure 5.9: Full test section frequency spectrum of crossflow (u) velocities at the gap center and mid-plane, Re = 2690.

with an average frequency of 1.1 Hz.

As discussed earlier, the frequency of the crossflow oscillations (f) can be presented in dimensionless form as a Strouhal number (St) using appropriate length (D) and velocity scales (U) as;

$$St = fD/U \tag{5.1}$$

Meyer and Rehme [27] proposed a Strouhal number for gap geometries based on a length scale as the square root of the gap width (S) times depth (D) combined with a characteristic velocity of the axial velocity at the gap edge (u_e). A mean Strouhal number of 0.115 based on these parameters is reported to correlate data within +/- 16% [27]. Results from the full test section model with a Reynolds number of 2690 show a gap edge velocity (u_e) of 0.065 m/s and a crossflow frequency of 1.0 Hz. With $S = 0.003$ m and $D = 0.021$ m, Equation 5.1 yields a Strouhal number of 0.122, which

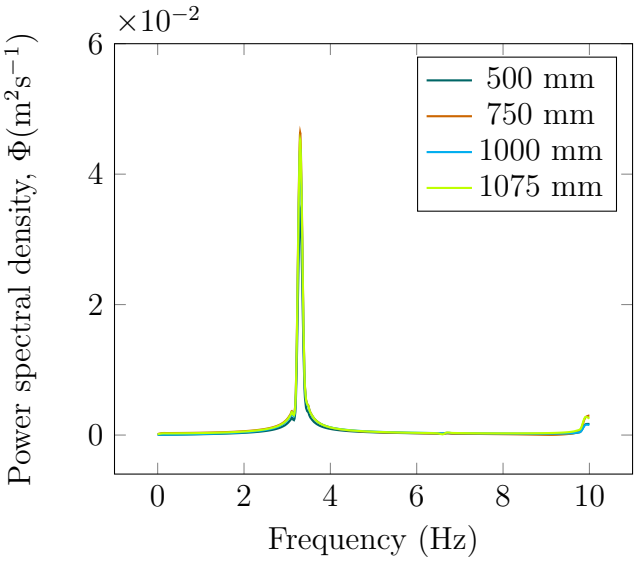

Figure 5.10: Full test section frequency spectrum of crossflow (u) velocities at the gap center and mid-plane, Re = 7500.

agrees very well with the corresponding Meyer and Rehme [27] value of 0.115.

The frequency spectrum of crossflow velocity at the gap center and midplane at various axial locations in the full test section model for a Reynolds number of 7500 is shown in Figure 5.10. Again, one clear peak frequency is obtained at all axial locations (3.3 Hz). No measured data is reported by either Mahmood [2] or Lexmond et al. [3] at these flow conditions. However, a Strouhal number can be determined from the Meyer and Rheme [27] correlation described above. CFD results from the full test section model with a Reynolds number of 7500 show a gap edge velocity (u_e) of 0.220 m/s. From Equation 5.1, with $S = 0.003$ m and $D = 0.021$ m, a Strouhal number of 0.119 is obtained. This again agrees very well with the corresponding Meyer and Rehme [27] value of 0.115.

5.2.5 Inter-Subchannel Mixing

The contributions of the observed flow structures and crossflow velocity fluctuations toward the inter-subchannel transport of a passive scalar were also experimentally investigated by Mahmood [2] and Lexmond et al. [3]. For these experiments, a measured volume of a NaCl solution was added as a tracer to one of the subchannels. The tracer transfer through the gap (θ) is defined by way of the measured concentration at the exit of each subchannel as;

$$\theta = \frac{C_2^{out}}{C_1^{out} + C_2^{out}} \tag{5.2}$$

where C is the scalar concentration, subscript 1 refers to the channel in which the tracer was injected, subscript 2 refers to the subchannel without tracer at the inlet.

Similarly, in the full test section simulations in ANSYS CFX, an additional scalar was added to simulate the NaCl tracer. It is assumed that the concentration of the tracer is uniform across the inlet of channel 1. The concentrations at the test section exits were tracked as fully developed flow was established through the solution domain at a simulation time of 30 seconds.

Figure 5.11 shows the fully developed NaCl concentration at the gap mid-plane in the full test section CFD simulations, without appendage, for a Reynolds number of 2690. Figure 5.12 shows the corresponding results for a Reynolds number of 7500. In both cases the periodic concentration fronts within the gap develop rapidly from the inlet and retain coherence as they propagate downstream. This is similar to the crossflow velocity contours in Figure 5.1 and 5.2.

The fully developed gap mid-plane flow oscillations alternately transport high and low concentration fluid through the gap. This is illustrated in Figure 5.13 showing

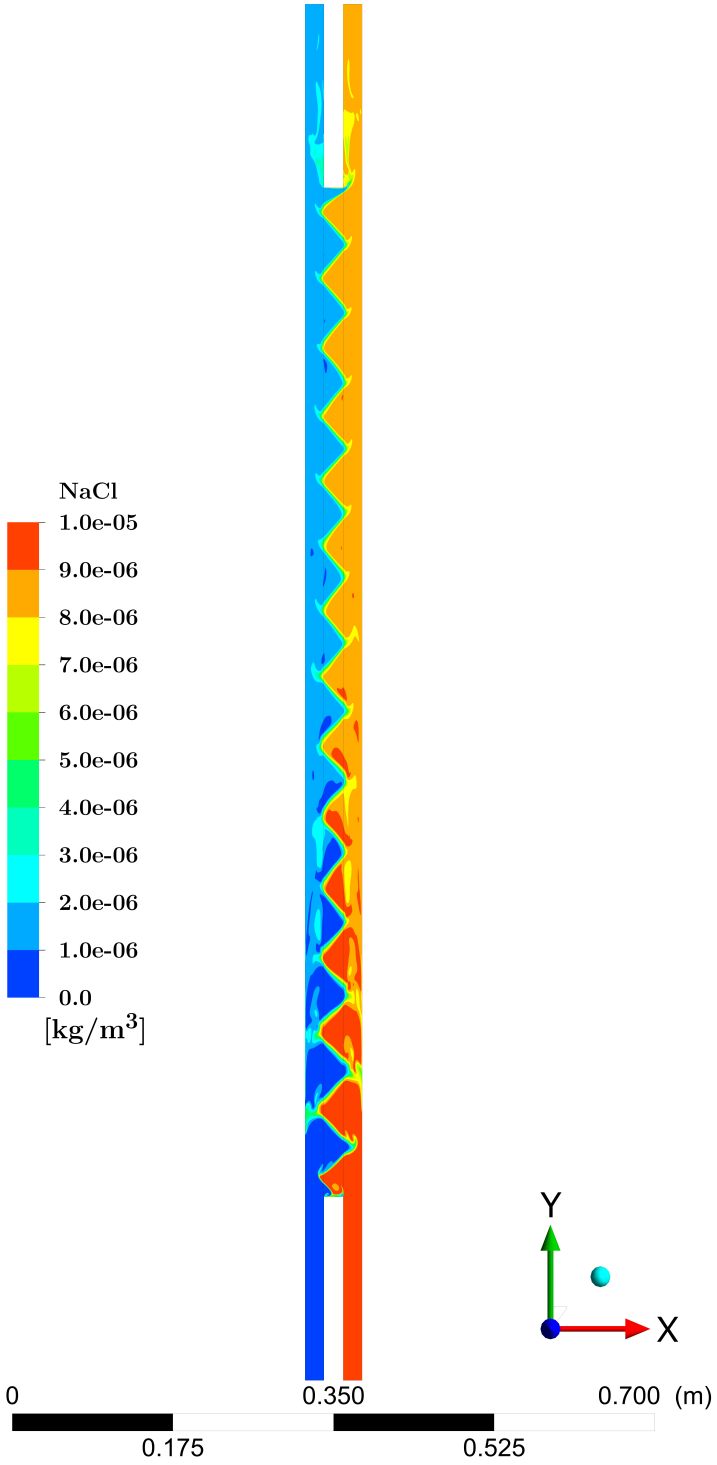

Figure 5.11: NaCl concentration through the gap mid-plane after fully developed flow has been established. Full test section model without appendage, Re = 2690.

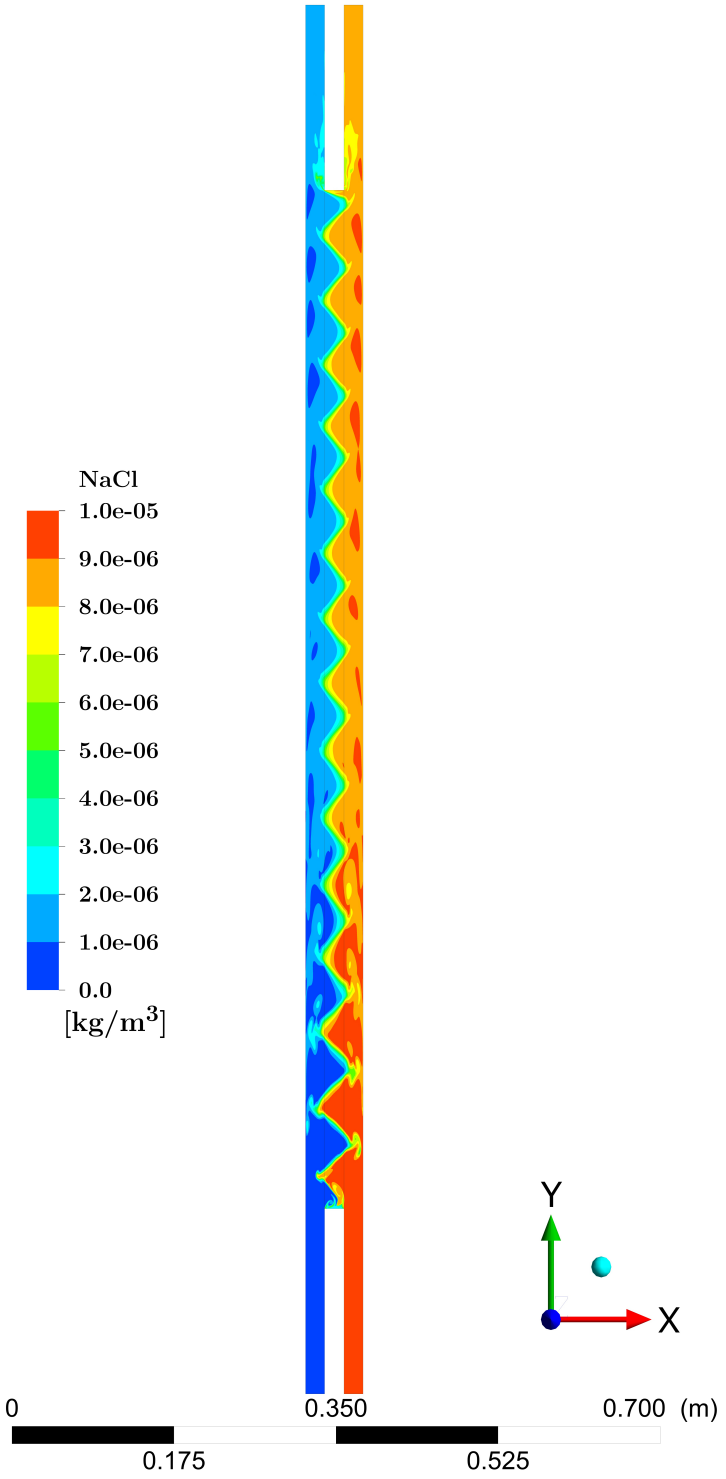

Figure 5.12: NaCl concentration through the gap mid-plane after fully developed flow has been established. Full test section model without appendage, Re = 7500.

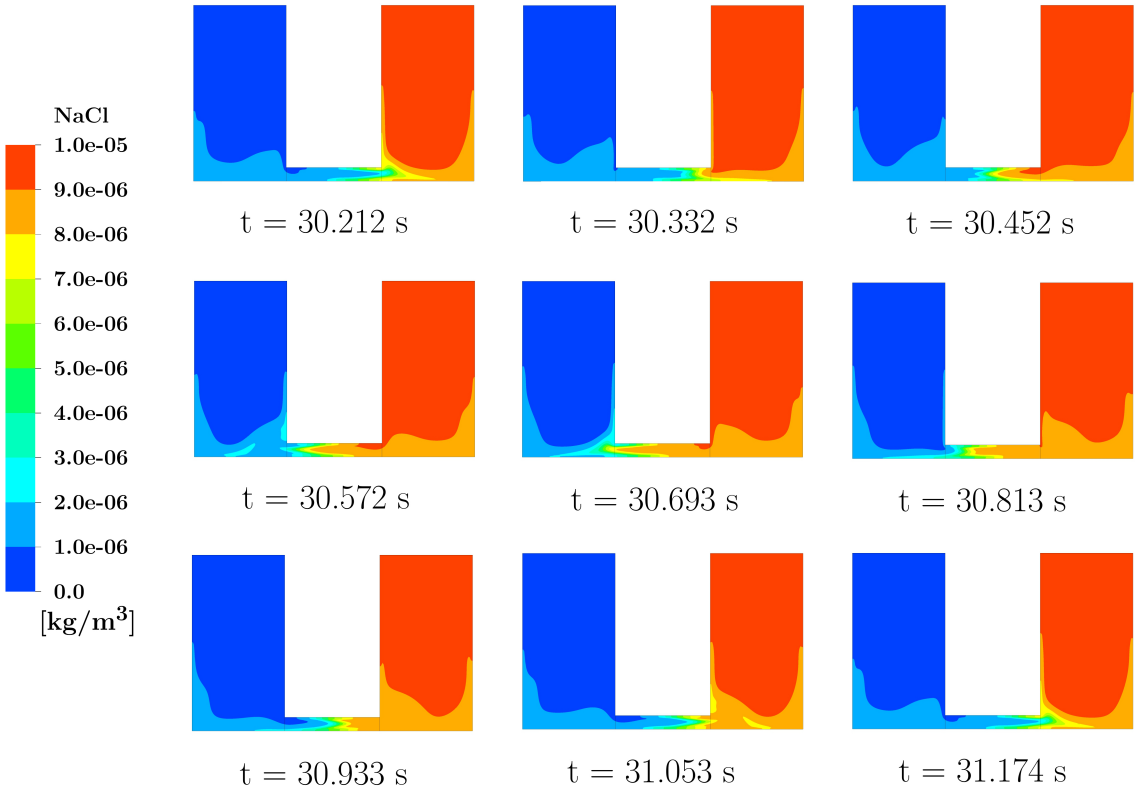

Figure 5.13: Fully developed concentration cycle at channel center (XZ plane). Full test section model, Re = 2690.

fully developed NaCl concentration distributions in the XZ plane at the channel center for a Reynolds number of 2690. The figures are at regular intervals through a full structure cycle of 962 ms. Note that the penetration of the concentration fronts from each channel through the gap is limited (Figures 5.11 and 5.13), agreeing with crossflow velocities and frequencies as the convective flow distances based on the average crossflow velocities and half periods roughly match the gap length.

After 30 seconds, with fully developed flow established, the simulations are extended for an additional 10 seconds. Figures 5.14 and 5.15 show the developed NaCl concentration at the exit of subchannels 1 and 2 for Reynolds numbers of 2690 and 7500 respectively. The initial (time zero) concentration at the exit of both subchannels would be zero as the tracer is introduced at the inlet of channel 1 only at time zero and must propagate downstream. In the final 10 seconds (t = 30 - 40 seconds), the results show reasonably stable concentrations at the exits of both subchannels. The NaCl concentration at the exit is averaged over this period to establish the exit concentrations (C_1^{out} and C_2^{out}). The tracer transfer through the gap (θ) is then determined by way of Equation 5.2.

Although Figure 5.11 suggests there may be notable fluctuations in exit concentration based on the concentration cycles through the gap mid-plane, the corresponding XZ plane concentration (Figure 5.13) shows the bulk of the subchannel concentration to be relatively stable throughout a cycle. As such, the full cross-sectional averaged exit concentration fluctuations are small (Figure 5.14). The final channel concentration could then be sensitive to changes in the extent of fluctuation penetration through the gap or in the degree of mixing of the penetrated flow in the subchannels.

Figure 5.16 shows the results for mixing from the experimental measurements of

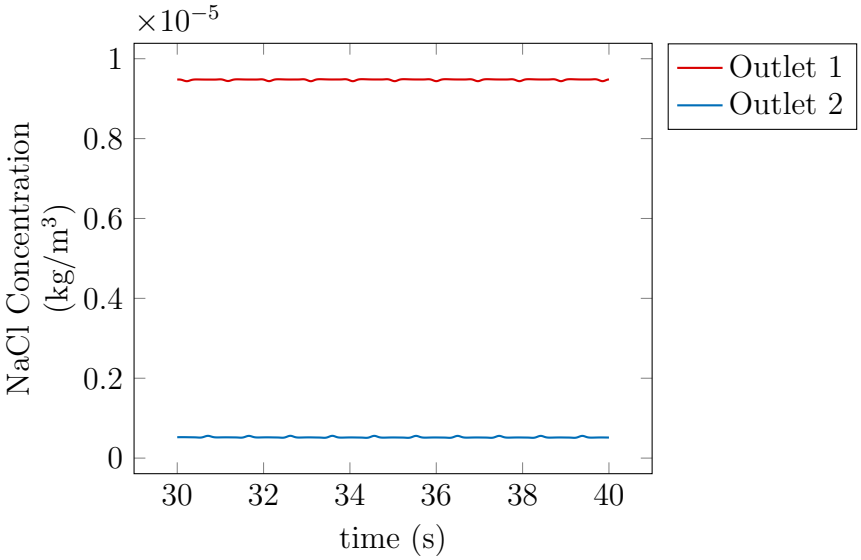

Figure 5.14: Averaged NaCl concentration at each outlet after fully developed flow established, Re = 2690.

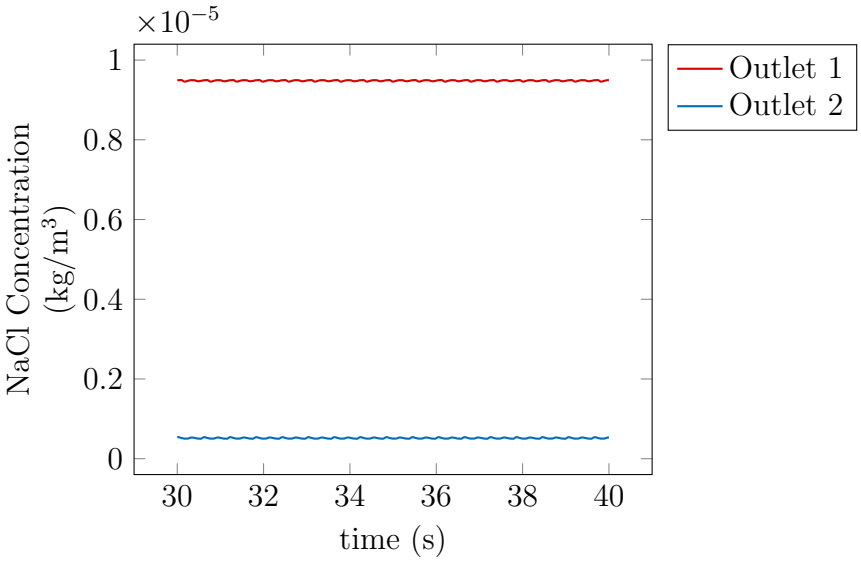

Figure 5.15: Averaged NaCl concentration at each outlet after fully developed flow established, Re = 7500.

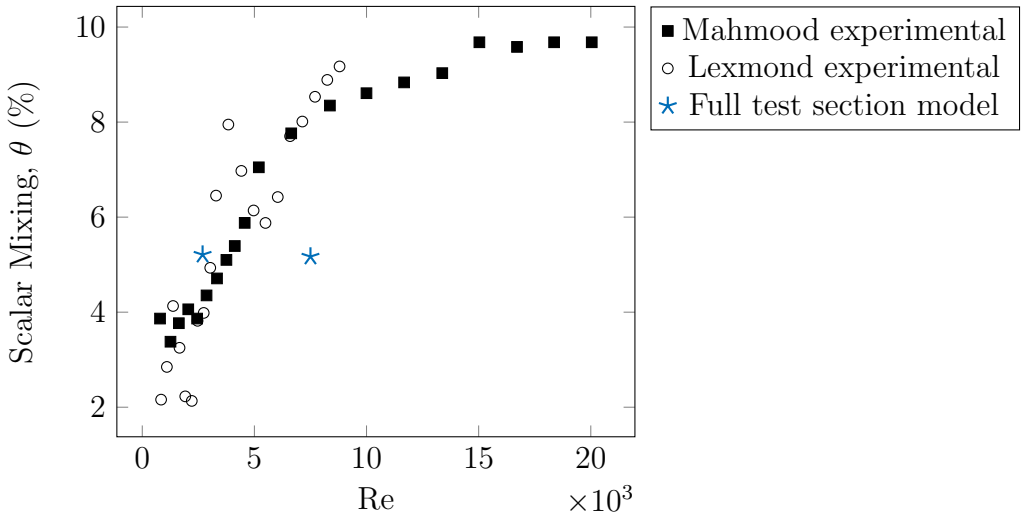

Figure 5.16: Comparison of subchannel mixing experimental measurements with CFD predictions from the current study for the full test section model.

Mahmood [2] and Lexmond et al. [3] generated over a range of Reynolds numbers. The mixing results from the full test section CFD models, without the appendage, are also shown for Re = 2690 and Re = 7500. Very good agreement with experiments is obtained in the absence of the appendage at Re = 2690. The trend of increased mixing with Reynolds number is not captured by the model at Re = 7500. The CFD results show mixing to be almost Reynolds number independent, which is characteristic of the higher Reynolds number experimental results shown in Figure 5.16 (i.e., Re > 15,000).

5.2.6 Full Test Section Summary

Twin-subchannel CFD models having geometry consistent with that used in the experimental programs of Mahmood [2] and Lexmond et al. [3] have been generated (see Chapter 4). Boundary conditions at two Reynolds numbers (2690 and 7500) consistent with the experimental procedure were applied to the CFD models and model

output is compared with measured data and known empirical correlations. In the absence of appendages, very good agreement with available experimental measurements ([2] and [3]) was obtained for periodic structure length, time-averaged axial velocity profiles through the gap midplane, gap-center crossflow velocity time traces, and RMS crossflow velocity. The Strouhal number for gap crossflow pulsation frequency also showed very good agreement with the correlation proposed by Meyer and Rehme [27].

The extent of inter-subchannel mixing agrees very well with experimental measurements for a Reynolds number 2690. The CFD results do not demonstrate the measured trend of increased mixing at a Reynolds number of 7500. The CFD results for mixing in this range are seen to be practically Reynolds number independent, a trend demonstrated by experimental measurement only at higher Reynolds numbers, i.e., above 15,000. This result is discussed in detail in Section 5.4.

5.3 Effect of a Gap Appendage on Flow and Mixing in a Twin-Subchannel Geometry

In this section, the effect of an appendage in the gap region connecting twin-subchannels on flow structures and mixing is investigated using CFD. Simulation results are generated at two Reynolds numbers (2690 and 7500) with the full test section model following the introduction of an appendage into the gap region at the test section center. The effects of the appendage on turbulent flow structures and mixing are isolated through comparisons of results with the corresponding full test section simulation without appendage.

5.3.1 Periodic Structure Length - Effect of Appendage

Figure 5.17 and 5.18 show instantaneous crossflow velocity contours through the gap midplane at Reynolds numbers of 2690 and 7500 for the appendage model. The appendage is located at the center of the test section (at 750 mm). The crossflow structures develop upstream of the appendage location in the same manner both with and without the appendage (compare with Figures 5.1 and 5.2). At the appendage location, the crossflow velocities are seen to increase and the distance between consecutive crossflow zones decreases. The increased crossflow is associated with flow diversion and vortex shedding around the appendage. Further downstream, the local effect of the appendage is seen to diminish and the gap instability induced crossflow zones begin to re-emerge as the dominant contributor to the gap pulsations.

5.3.2 Crossflow Power Spectral Density Functions - Effect of Appendage

Figures 5.19 and 5.20 show crossflow power spectral density versus frequency at various axial locations for Re = 2690 without and with the appendage respectively. Upstream of the appendage (at 500 mm and 700 mm), the power spectral density versus frequency traces with the appendage are very similar to the corresponding traces without the appendage. These traces are characteristic of the gap instability induced crossflow pulsations discussed in Section 5.2.4 having a frequency of 1 Hz and power spectral densities between 0.01 and 0.015 m^2/s. This observation, combined with the corresponding similarity in crossflow velocity contours discussed in Section 5.3.1, indicates that the influence of the appendage does not propagate upstream.

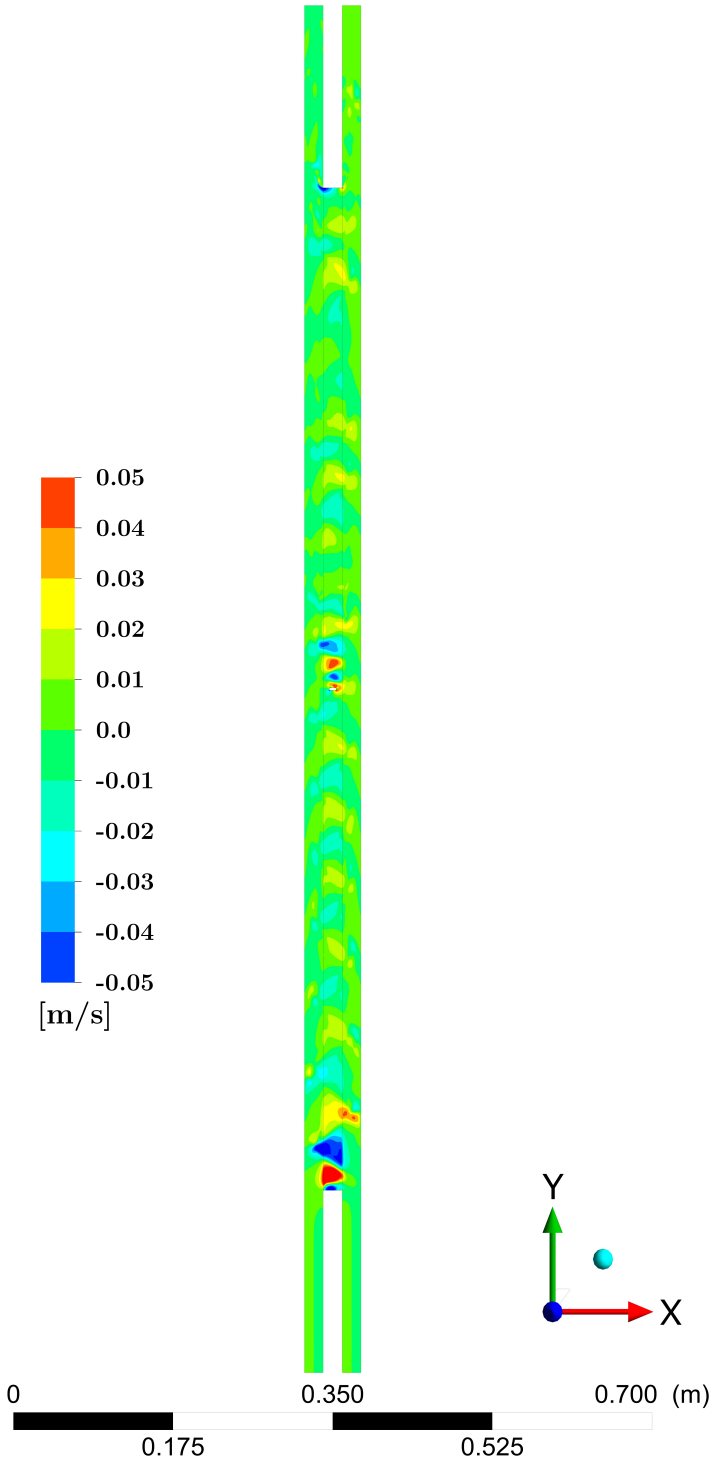

Figure 5.17: Instantaneous crossflow (x-directed) velocity contours through the gap mid-plane. Full test section model with appendage, Re = 2690.

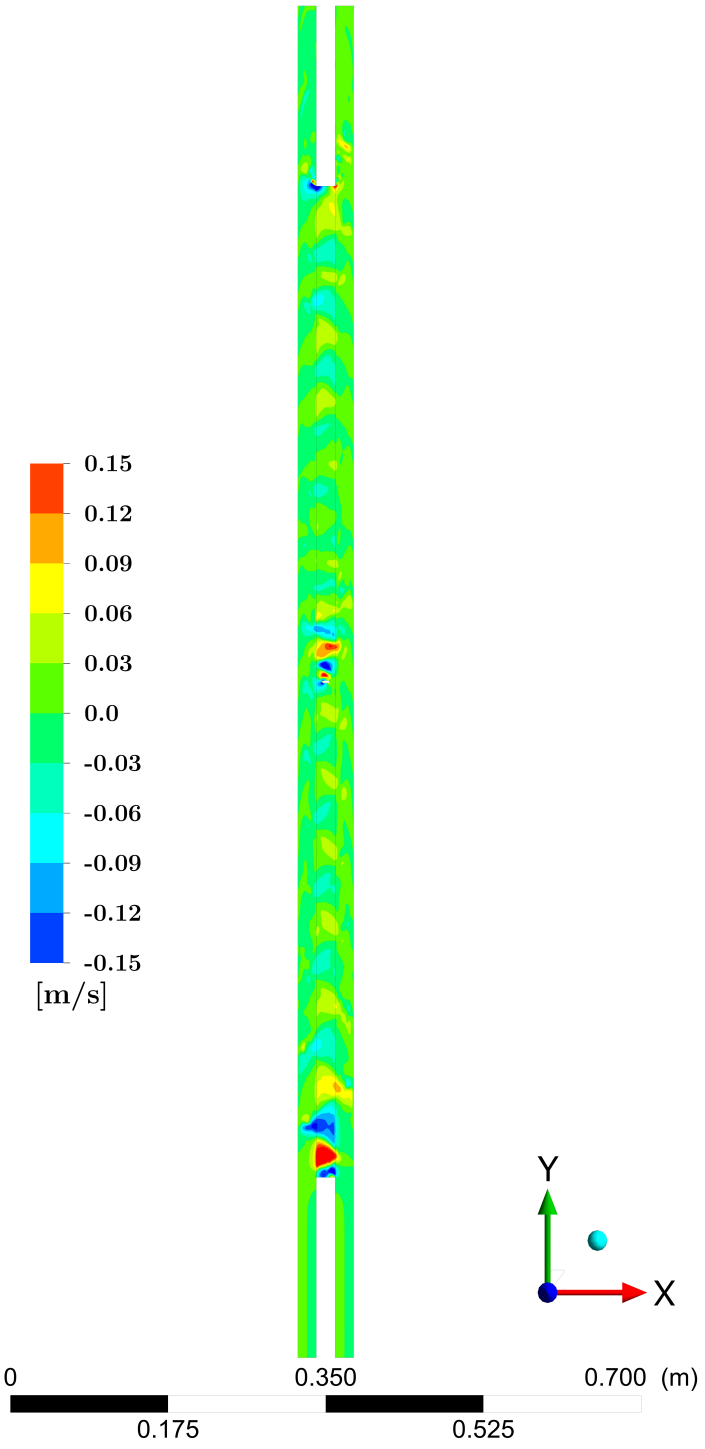

Figure 5.18: Instantaneous crossflow (x-directed) velocity contours through the gap mid-plane. Full test section model with appendage, Re = 7500.

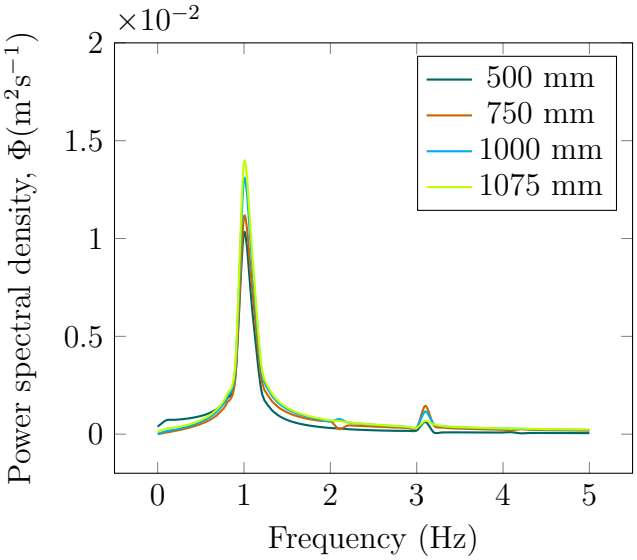

Figure 5.19: Frequency spectrum of crossflow (u) velocities at the gap center and mid-plane without appendage, Re = 2690 (as presented in Figure 5.9).

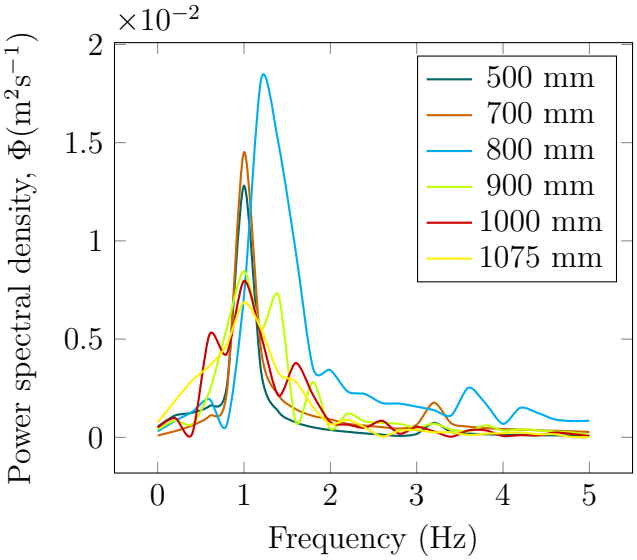

Figure 5.20: Frequency spectrum of crossflow (u) velocities at the gap center and mid-plane with appendage, Re = 2690.

The peak frequency shifts higher, from 1.0 Hz to approximately 1.2 Hz, immediately downstream of the appendage (at 800 mm, see Figure 5.20). This is coupled with an increase in power spectral density. This higher frequency is consistent with the vortex shedding frequency of such a rectangular bluff body in a free-stream flow. As discussed in Section 4.3.3, the Strouhal number for this geometry is approximately 0.13 [72] for a characteristic length defined as the width of the bluff body transverse to the flow (0.00731m). An appropriate characteristic velocity for an appendage located at the gap center would be bounded by the velocities at the gap center and gap edge (0.050 m/s to 0.065 m/s). This velocity range, combined with $f = 1.2$ Hz and $D = 0.00731$ m, yields a Strouhal number in the range of 0.175 to 0.135. This is in rough agreement with the value of 0.13 from Naudascher and Rockwell [72].

At 900 mm, the peak associated with the appendage vortex shedding frequency decreases as the peak associated with the gap instability induced crossflow frequency recovers. Based on the crossflow velocity contours (Figure 5.17) and the spectral density versus frequency traces (Figure 5.20), the gap induced pulsations do not fully recover before the end of the test section. As such, the effect of the appendage is seen to extend well downstream of the appendage location.

The crossflow power spectral density versus frequency at various axial locations along the test section without and with the appendage for Re = 7500 are shown in Figures 5.21 and 5.22 respectively. Again, upstream of the appendage (at 500 mm and 700 mm), these traces are not altered significantly with the addition of the appendage. They are characteristic of the gap instability induced crossflow pulsations discussed in Section 5.2.4 having a frequency of 3.3 Hz. This observation, again combined with the corresponding similarity in crossflow velocity contours discussed in Section

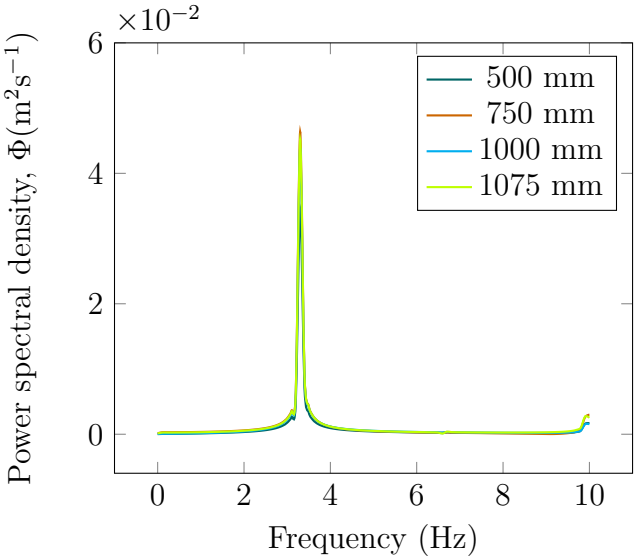

Figure 5.21: Frequency spectrum of crossflow (u) velocities at the gap center and mid-plane without appendage, Re = 7500 (as presented in Figure 5.10).

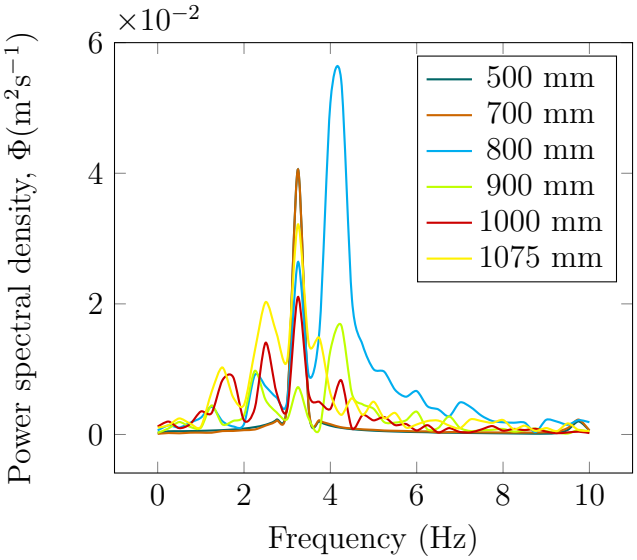

Figure 5.22: Frequency spectrum of crossflow (u) velocities at the gap center and mid-plane with appendage, Re = 7500.

5.3.1, supports the conclusion that the influence of the appendage does not propagate upstream.

The peak frequency is seen to shift higher immediately downstream of the appendage (at 800 mm), from 3.3 Hz to approximately 4.1 Hz. This is coupled with an increase in power spectral density. This higher frequency is again consistent with the vortex shedding frequency of such a rectangular bluff body in a free-stream flow. Applying the same approach as above with Re = 2690, the velocities at the gap center and gap edge for Re = 7500 are 0.184 m/s and 0.220 m/s, respectively. This velocity range, combined with $f = 4.1$ Hz and $D = 0.00731$ m, yields a Strouhal number in the range of 0.163 to 0.136. This again is in rough agreement with the value of 0.13 from Naudascher and Rockwell [72].

Behaviour downstream of the appendage for a Reynolds number of 7500 is similar to that at 2690. The frequency peak associated with vortex shedding from the appendage decreases as the peak associated with the gap instability induced crossflow frequency recovers. Both the crossflow velocity contours (Figure 5.18) and the power spectral density versus frequency traces (Figure 5.22), support the conclusion that the effect of the appendage extends well downstream of the appendage location.

5.3.3 Inter-Subchannel Mixing - Effect of Appendage

The combination of higher crossflow velocity and the higher frequency around the appendage is expected to contribute to an increase in mixing between the subchannels. Figure 5.23 shows the trace of NaCl concentration through the gap mid-plane once fully developed flow is established for a Reynolds numbers of 2690 with the appendage. Figure 5.24 shows the corresponding trace for a Reynolds number of

7500. No significant effect on the concentration distribution is noted upstream of the appendage at either Reynolds number (compare Figures 5.11 and 5.12). The concentration distribution is clearly disturbed downstream of the appendage with a disruption in the regular sawtooth concentration profiles. Further, broader regions of intermediate concentration (8.0×10^{-6} to 2.0×10^{-6} kg/m^3) appear as wakes through the gap and around the gap edges.

Again, the NaCl concentration at the exit of each subchannel is averaged over the steady state portion of the simulation to establish the exit concentrations (C_1^{out} and C_2^{out}) and the tracer transfer through the gap (θ) is then determine from Equation 5.2. Figure 5.25 shows the results for mixing across subchannels from the experimental measurements of Mahmood [2] and Lexmond et al. [3] generated over a range of Reynolds numbers. The mixing results from the full test section CFD models, without and with the appendage, are also shown for Re = 2690 and Re = 7500. With an end plate type appendage introduced into the gap region, total mixing along the test section is predicted to increase due to flow diversion and vortex shedding around the appendage. Although data is limited, it appears that mixing is augmented more by the appendage with increasing Reynolds number, specifically by 13% at Re = 2690 and 29% at Re = 7500.

5.3.4 Full Test Section Summary - Effect of Appendage

Twin-subchannel CFD models having geometry consistent with that used in the experimental programs of Mahmood [2] and Lexmond et al. [3] have been generated with the addition of an appendage in the gap region connecting the channels. With an end plate type appendage introduced into the gap region, crossflow velocity and

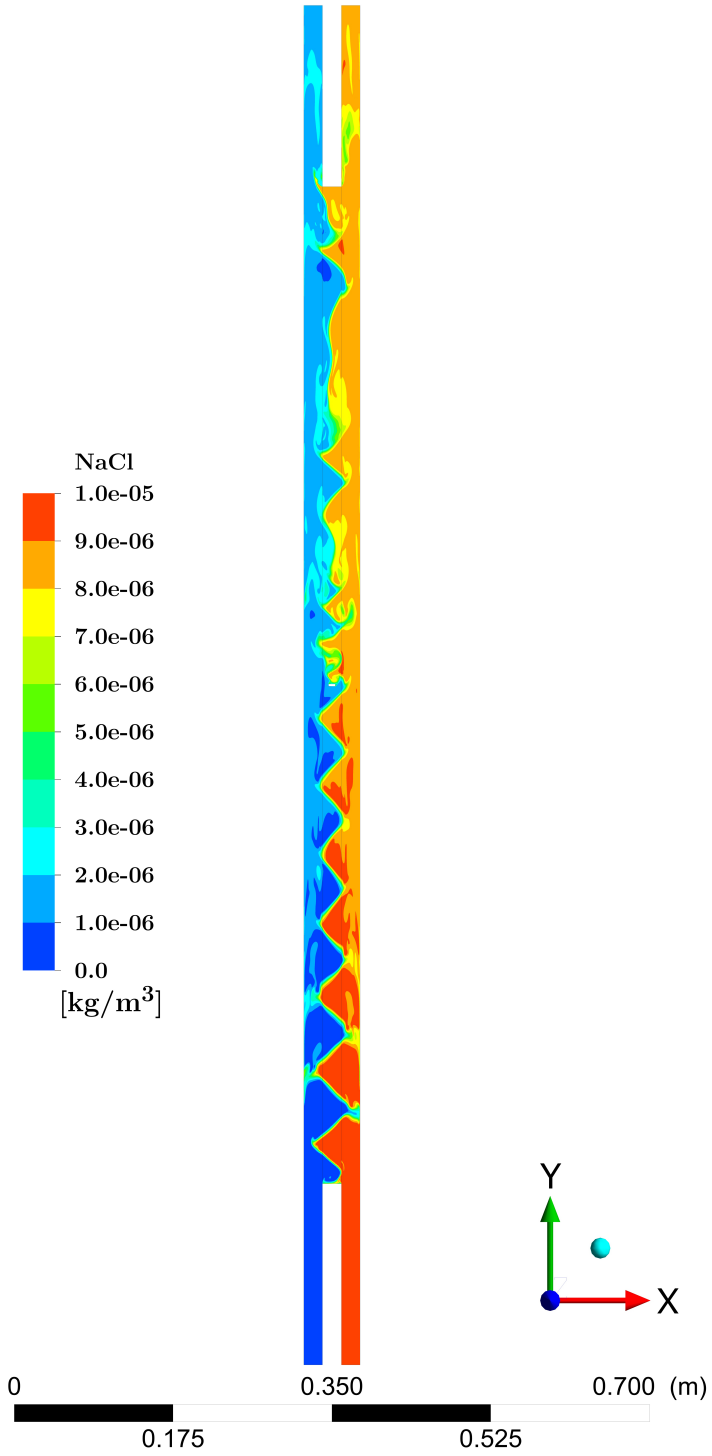

Figure 5.23: NaCl concentration through the gap mid-plane after fully developed flow has been established. Full test section model with appendage, Re = 2690.

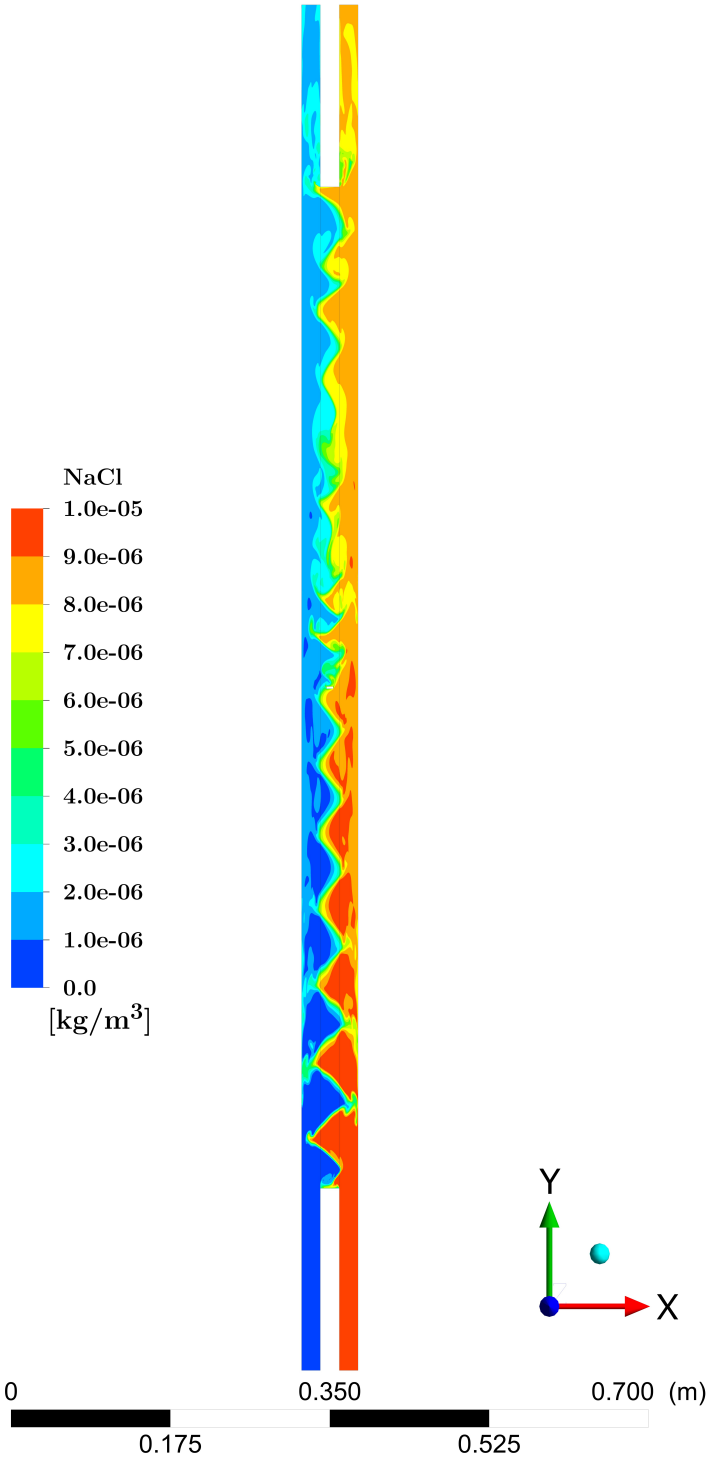

Figure 5.24: NaCl concentration through the gap mid-plane after fully developed flow has been established. Full test section model with appendage, Re = 7500.

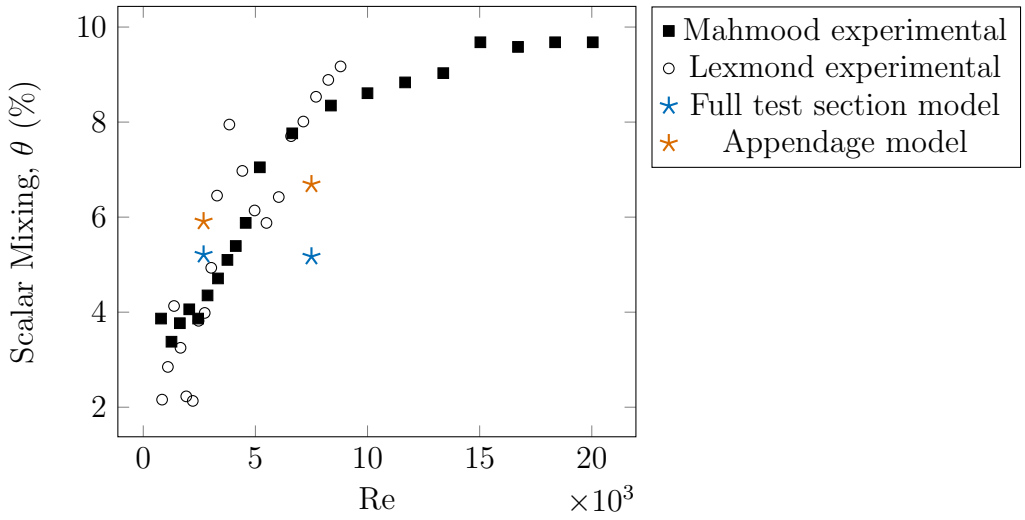

Figure 5.25: Comparison of subchannel mixing experimental measurements with CFD predictions from the current study.

frequency are predicted to increase immediately downstream of the appendage due to flow diversion and vortex shedding. The higher frequency is consistent with the vortex shedding frequency calculated for a stationary rectangular cylinder at the gap conditions. These phenomena contribute to increased mixing just downstream of the appendage. Further downstream, gap induced instabilities begin to be re-established as the dominant contributor to crossflow pulsations. Mixing is augmented more by the appendage with increasing Reynolds number for the range examined. This result is further discussed in Section 5.4.

5.4 Potential Increase in Subchannel Mixing Mechanisms

For the full test section without an appendage, the properties of the gap flow pulsations (frequencies, velocity fluctuations, and length scales) are well predicted by the

model at both Re = 2690 and 7500. It has been established that these pulsations through the gap are the dominant contributor to inter-subchannel mixing. The total tracer transfer between subchannels is reasonably well predicted for Re = 2690, however, the model fails to capture the measured increase in scalar transfer through the gap with increased Reynolds number at Re = 7500. It is expected that a second order contributor to the total transfer is not being captured by the model for the range of Reynolds numbers considered.

One flow characteristic that will influence tracer transfer through the gap is the cross-sectional distribution of tracer within the subchannels. Figure 5.13 shows a model predicted cycle of this distribution at the channel center. The majority of the cross-section is seen to carry a concentration in the extreme range for that subchannel ($C_2 < 1.0\times10^{-6}$ and $C_1 > 9.0\times10^{-6}$) throughout the cycle. The concentration at the entrance to the gap varies throughout the cycle according to the flow pulsations. Vonka (1988a) [19] measured secondary flow characteristics in a rod bundle geometry and concluded that these flows can contribute to the transport processes, but primarily within the subchannel as opposed to between subchannels. Secondary flows then may redistribute a scalar within the subchannel, influencing the amount exchanged through the gap with the pulsations.

Secondary flows of Prandtl's second kind are often studied by considering turbulent flow in a square duct because of its relatively simple geometry. The mean transverse secondary flow that occurs in this geometry consists of eight streamwise vortices, two counter-rotating in each corner. Flow is directed toward each corner from the duct center along the corner bisector, and toward the duct center along each

wall bisector (Huser and Biringen (1993) [73]). Hoagland (1960) [74] investigated secondary flows experimentally in rectangular ducts of varying aspect ratio (1:1, 2:1 and 3:1). He reported large velocities along the corner bisector feeding flow from the duct core to the corner region. He concluded that the duct aspect ratio does not appear to influence the magnitude of the secondary velocities. As such, observations from square duct studies discussed below are considered relevant to the current geometry (subchannel aspect ratio 1.9:1).

Secondary flows developing separately in each subchannel will redistribute flow from the extreme concentration (high or low) central portion of the subchannels to the corners creating a steeper concentration gradient across the gap. This will in turn enhance scalar mixing through the gap by way of the flow pulsations. Rectangular twin-subchannel geometries with the gap connection at a corner, as in the current study, realize maximum benefit from this transfer enhancement mechanism. The effect will be commensurate with the strength of the secondary flows.

Zhang et al. (2015) [1], is one of the many Direct Numerical Simulation (DNS) studies of turbulent flows in square ducts. They conducted several DNS runs of turbulent flows in a square duct at various shear velocity based Reynolds numbers (Re_τ). For the subchannel geometry considered in the current study, the correspondence between Re_τ and Re as presented by Derksen (2010) [61] has been incorporated into the following discussion.

Calculated normalized mean secondary velocity vectors and stream-wise flow contours in the lower left quadrant of the duct are shown in Figure 5.26 for Re = 5000, 11000, 20000 and 35000 (Zhang et. al, 2015) [1]. The expected pair of counter-rotating vortices in the quadrant is clearly visible at all Reynolds numbers. The secondary

flows will transfer fluid from the central region of the duct toward the corners. The strength of the vortices increase with Reynolds number as demonstrated by the secondary velocity vectors along the corner bisector penetrating further into the corner with increasing Reynolds number. This effect is most clearly evident between 5.26 (a) and 5.26 (b) with Reynolds number increasing from Re = 5000 to Re = 11000 respectively. At the higher Reynolds numbers (Re = 20000 and 35000), the normalized profiles appear reasonably Reynolds number independent. It is also noted by the authors that the marginal Reynolds number capable of maintaining the two counter rotating vortices in each corner is Re $\sim$ 2000. At Reynolds numbers below this value the secondary flows are too weak to persistently maintain this flow structure.

Figures 5.27 and 5.28 (from Zhang et. al, 2015) [1] show the corresponding normalized z-directed secondary flow velocity profiles from the wall (y/h = 0.0) to the channel center (y/h = 0.5). Figure 5.27 is along a line near the channel center (z/h = 0.4) and Figure 5.28 along a line near the bottom of the channel (z/h = 0.08). The profiles for Re = 5000 demonstrate a notably different trend as compared to those from the higher Reynolds number flows at both locations. The profile for Re = 11000 has clearly migrated significantly towards the profiles at the higher Reynolds numbers (Re = 20000 and 35000) and the profiles at the higher Reynolds number appear to be reasonably converged. Again, the Reynolds number effect on the y-directed secondary flow profiles is most significant in the Re = 5000 to 11000 range.

The spectrum of secondary flow behaviour identified by Zhang et al. (2015) and the expected consequential effect on scalar redistribution in the duct cross section can be postulated as follows. Below Re $\sim$ 2000, secondary flows are too weak to persistently form the eight vortex structures and as a result cannot contribute to scalar

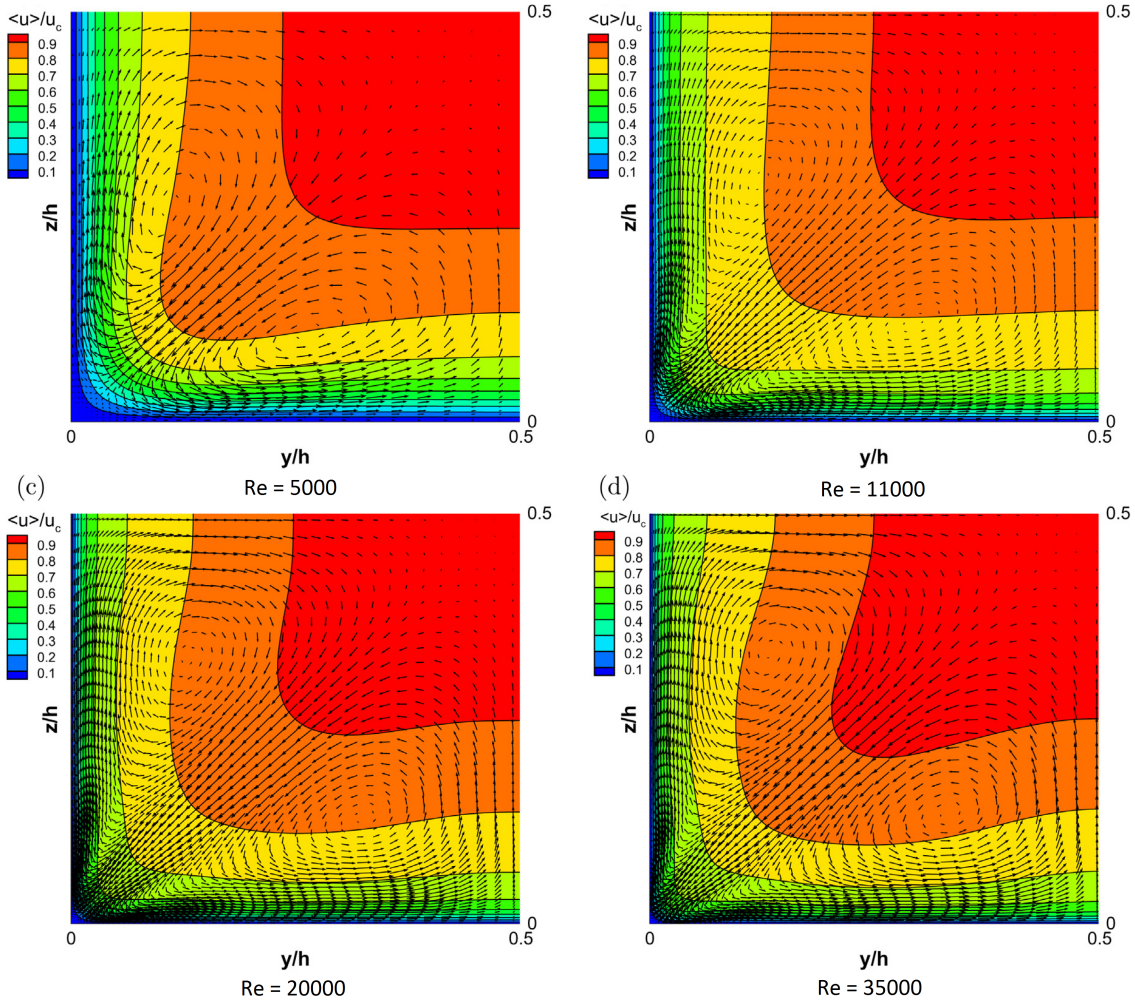

Figure 5.26: Mean normalized secondary velocity vectors with mean normalized streamwise flow contours (Zhang et. al, 2015) [1]

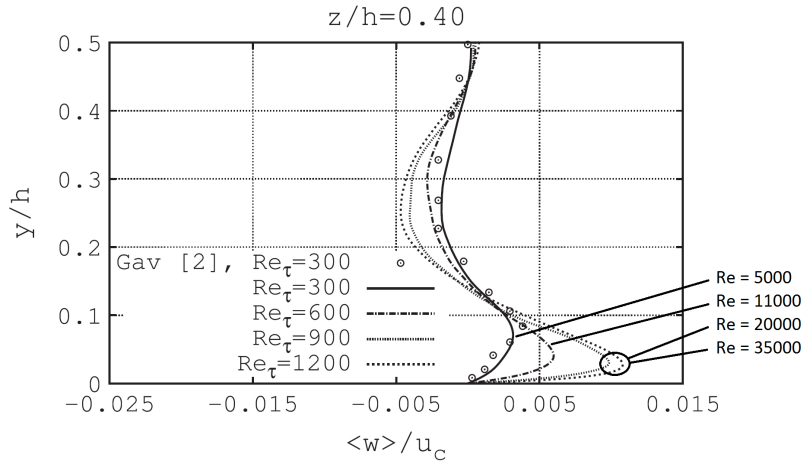

Figure 5.27: Normalized z-directed secondary flow profiles near the wall bisector (Zhang et. al, 2015) [1]

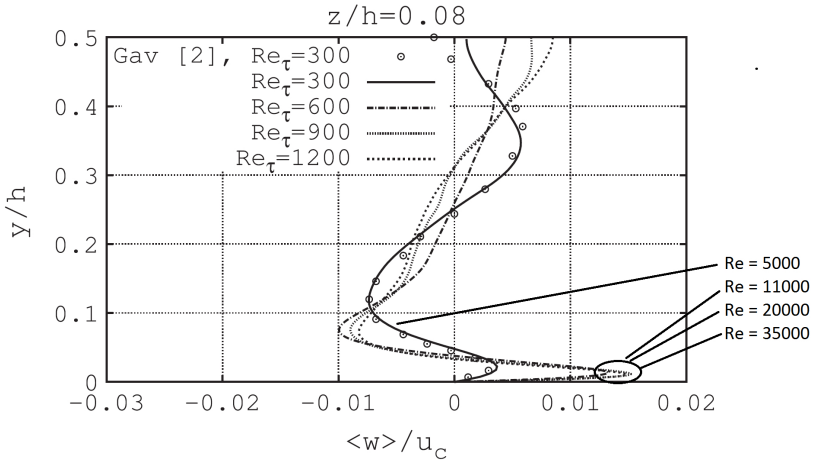

Figure 5.28: Normalized z-directed secondary flow profiles near the duct bottom (Zhang et. al, 2015) [1]

redistribution within the subchannels. For 2000 $<$ Re $<$ 11,000, counter rotating vortices are formed in each corner with their strength and consequently influence on scalar redistribution increasing significantly throughout the range. For Re $>$ 11000, the secondary flow vortices, and by association scalar redistribution, become essentially Reynolds number independent.

Figure 5.26 shows the experimental mixing results from Mahmood [2] and Lexmond et al. [3] generated over a range of Reynolds numbers. The trend of total tracer transfer through the gap shows a strong positive correlation with the expected contribution of secondary flows to scalar redistribution within the subchannels outlined above. For Re $\sim$ 2000, corresponding to a zone of weak or non-existent secondary flows, mixing appears to be independent of Reynolds number. As Reynolds number increases from Re = 2000 to Re = 11,000, the strength and influence of secondary flows on scalar redistribution are expected to increase significantly and the total tracer transfer through the gap is seen to increase sharply in this range. Between Re = 11,000 and Re = 20,000, the strength of secondary flows and their influence on scalar redistribution trends towards Reynolds number independence as does the tracer transfer through the gap. The experimental results are consistent with secondary flows contributing to the overall level of tracer transfer through the gap by way of scalar redistribution within the subchannel cross section.

The mixing results from the current full test section CFD models, without the appendage, are also shown on Figure 5.26 for Re = 2690 and Re = 7500. As discussed earlier, the Spalart-Allmaras (SA) model applied in the current study is an isotropic turbulent diffusion model. This model does not include the anisotropy of normal stresses responsible for generating secondary flows in straight rectangular ducts. As

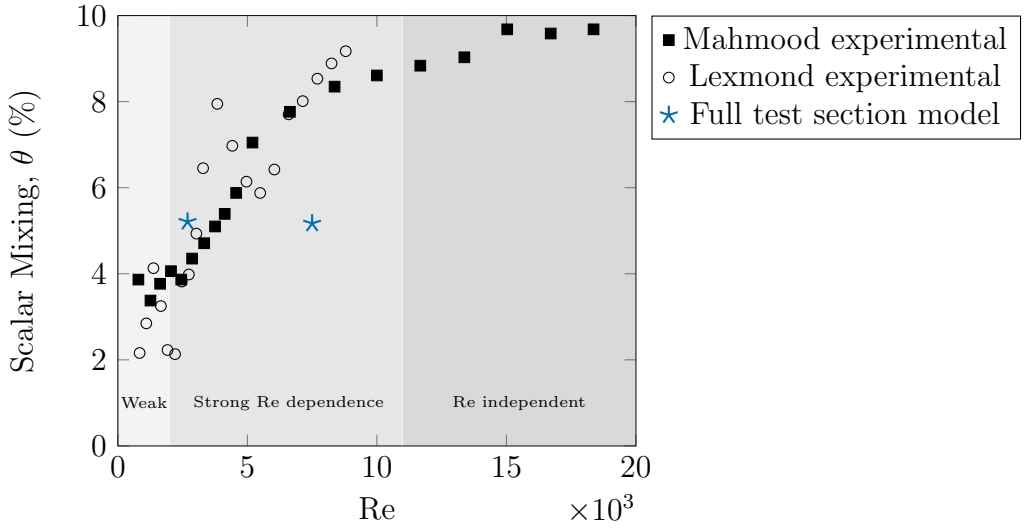

Figure 5.29: Subchannel mixing results from Mahmood [2], Lexmond et. al [3] and current study, along with Re based regions of secondary flow influence on scalar redistribution within channels adapted from Zhang et al. (2015) [1].

such, the secondary flow effect on tracer redistribution within the subchannel, and hence on inter-subchannel mixing, is not captured in the calculations.

The calculated properties of the gap flow pulsations and the extent of mixing from the current study for Re = 2690 agree well with measurements. A Reynolds number of 2690 is approaching the lower limit where stable counter-rotating vortex pairs are able to form in the subchannel corners. Mahmood [2] carried out LES simulations applying periodic boundary conditions in the streamwise direction for this geometry at a Reynolds number of 2690. Results were only documented for Re = 2690 and the simulation did not include a passive scalar. His assessment was that the numerical results show no evidence of strong secondary flows near the gap region. It can be reasonably concluded that secondary flows are still relatively weak at this Reynolds number and contributions to scalar redistribution within the subchannel are not significant. Agreement between the model and experiment is then not surprising. The

model is simply not able to capture a mechanism that is not contributing to the result. It then follows that calculated mixing results are not expected to be significantly altered by application of an anisotropic turbulence model capturing secondary flows for Re = 2690.

For Re = 7500, the predicted properties of the gap flow pulsations again agree well with measurements, although the extent of mixing is under predicted. This Reynolds number is well within the range where secondary flows strengthen and are expected to alter the subchannel scalar distribution (i.e., 2000 $<$ Re $<$ 11,000). Neglect of anisotropy in the turbulence model precludes secondary flows in the predicted flow field and the associated redistribution of scalar to the corners of the subchannels. This redistribution of scalar would increase the scalar gradient across the gap and thereby increase the scalar transfer through the gap by way of flow pulsations. It is anticipated that increased subchannel mixing in calculations for Re = 7500 will bring model prediction closer to measurement by this mechanism.

Chapter 6

Summary, Conclusions, and Recommendations

6.1 Summary and Conclusions

The objective of this work has been to study of the effects of appendages on flow characteristics and scalar mixing in gap-connected subchannel geometries. Appendages, such those introduced by end plate or bearing pad type obstructions in CANDU fuel bundles, are assessed. The assessment considers a symmetric, rectangular compound channel geometry connected by a single rectangular gap using CFD. The numerical analysis utilizes ANSYS CFX and models developed both with and without a gap-centered appendage in order to isolate the effect on flow characteristics and bulk crossflow mixing.

The study involved several stages in an overall systematic approach. Models (without appendage), consistent with the full test sections from two reference experimental

studies ([2] and [3]), were generated. A sensitivity study, applying streamwise periodic boundary conditions to a sub-domain of the full test section model, was carried out to establish suitable parameters (e.g., mesh size, time step) for the full test section simulations required for mixing calculations. Once determined, these parameters are applied in the full test-section simulations used to quantify flow characteristics and mixing in the absence of an appendage. Consistent with the experiments, the extent of mixing between subchannels is determined by tracking the exit concentration of a passive scalar introduced into one of the subchannels at the entrance. The periodic and full test section models, without appendages, were validated against experimental measurements from the reference studies. A single gap-centered appendage was then added to the validated full test section model. Simulations are repeated, and by comparison of the results with the no appendage model, the effects of the appendage are isolated.

Turbulent transport through gap regions of tight lattice geometries is dominated by large scale quasi-periodic structures at gap edges promoting inter-subchannel mixing by way of crossflow pulsations through gaps. The length and timescales of the coherent structures are significantly larger than those inherent in open pipe turbulent flow. In the current study, quasi-periodic structure details are captured through calculations in an unsteady RANS framework coupled with the Spalart Allmaras turbulence model to close the RANS equations.

Full test section simulations are carried out at two Reynolds numbers (2690 and 7500) consistent with conditions at which detailed experimental measurements are reported ([2] and [3]). Structure length, axial velocity distributions, crossflow velocity

fluctuations, power spectral density functions and inter-subchannel mixing are compared with available data. For the full test section model without an appendage, these macroscopic properties of the gap flow pulsations are well predicted by the model at both Reynolds numbers. The total tracer transfer between subchannels is reasonably well predicted for Re = 2690, however, the model fails to capture the measured increase in scalar transfer through the gap with increased Reynolds number at Re = 7500.

It is reasoned that the scalar concentration gradient across the gap at Re = 7500 may be under predicted due to the absence of secondary flows in the subchannels. Secondary flows in rectangular ducts redirect flow from the center of the subchannel to the gap located at the corners. Combined with the more extreme scalar concentration in the core of each subchannel, secondary flows are expected to increase the scalar concentration gradient across the gap. This in turn enhances cross gap mixing with the flow pulsations. Spalart-Allmaras is an isotropic turbulent diffusion model which does not include the anisotropy of normal stresses responsible for generating secondary flows in straight rectangular ducts. As such, this secondary flow effect on tracer redistribution within the subchannel, and hence on inter-subchannel mixing, is not captured in the calculations.

Based on a numerical study of secondary flows in square ducts by Zhang et al. (2015) [1], it is demonstrated that secondary flow effects at a Reynolds number of 2690 are expected to be quite weak. Accordingly, they would have little effect on the experimentally measured mixing and their exclusion from the calculations is of no consequence allowing agreement between model predictions and experiments. The same study showed that the strength and influence of secondary flows increased with

Reynolds number between Re = 2690 and 7500. These effects may be substantial at Re = 7500. Neglect of secondary flows and the associated scalar redistribution in the model calculations may account for the inability of the model to capture the Reynolds number effect on inter-subchannel mixing.

With the appendage introduced into the gap region, crossflow velocity and frequency are predicted to increase immediately downstream of the appendage due to flow diversion and vortex shedding. The higher local frequency is shown to be consistent with the vortex shedding frequency calculated for a stationary rectangular cylinder at the gap conditions. These phenomena contribute to increased mixing just downstream of the appendage. Further downstream, gap induced instabilities begin to be re-established as the dominant contributor to crossflow pulsations. Mixing is augmented more by the appendage with increasing Reynolds number for the range examined.

The macroscopic crossflow pulsation properties do not appear to be affected by secondary flows in the subchannels. The current isotropic model is expected to capture the influence of the appendage on flow pulsations and the associated mass transfer through the gap. Secondary flows are reasoned to be an insignificant contributor to the scalar concentration distribution at Re = 2690. As such there is some confidence in the model predictions of increased mixing at this Reynolds number with the introduction of the appendage (13%).

At a Reynolds number of 7500, with the appendage, the properties of the gap flow pulsations and associated gap mass transfer are again expected to be reasonably well captured by the model. The ability of the model to predict the scalar concentration gradient across gap is uncertain at this Reynolds number in the absence of secondary

flow effects. The increase in total tracer transfer depends on a combination of both of these parameters. As such the model predicted 29% increase should be considered suspect.

6.2 Recommendations

By comparison with measurements, the CFD models generated for this study have been shown to capture well the dynamics of quasi-periodic structures that develop at gap edges promoting cross channel pulsations and inter-subchannel mixing. Although direct measurements are not available for comparison, flow diversion and vortex shedding around a gap-centered appendage have model-predicted characteristics that are reasonably consistent with known physics. In the absence of an appendage, the Reynolds number effect on inter-subchannel mixing is not captured by the model. It has been demonstrated that neglect of anisotropy of normal stresses in the turbulence model, precluding secondary flows and scalar redistribution within the subchannels, can reasonably account for this deficiency.

The reference experimental design dictated modelling of the entire test section in order to generate results that could be compared with measurements. In addition, a very detailed mesh was applied with a time step sufficiently small to capture the unsteady characteristics of the pulsations. As a result, one significant challenge encountered in this study was the extremely long simulation time required for each run (many months). A methodology incorporating wall models will allow a coarser mesh to be applied with a corresponding reduction in simulation time. As a first step in advancing this investigation, it is recommended to perform a sensitivity study to identify such modelling methods that allow for an increase in computational efficiency.

The results from the current study, without appendage, would be used as a reference to assess convergence of the revised models.

It is further recommended that the hypothesis identifying neglect of secondary flows in the CFD model as the source of the discrepancy in Reynolds number effect between modelled and measured mixing be tested. The revised more efficient models, without an appendage, should be used as the base calculations with application of a suitable anisotropic turbulence model to promote secondary flows within the subchannels. Secondary flows can also be promoted within the subchannels by applying Large Eddy Simulation modelling in that region. It is expected that the effect on predicted inter-subchannel mixing will be insignificant at a Reynolds number of 2690. For a Reynolds number of 7500, the model predictions are expected to move closer to the experimental measurement.

If the models developed as outlined above are shown to reasonably capture the Reynolds number effect on mixing across the test section, it is recommended that they be modified to include the gap centered appendage from the current study. It has been reasoned that the degree of mixing augmentation at Re = 2690 will not be strongly affected. It is unclear what effect the revised modelling will have at Re = 7500 due to the unknown interaction of secondary flows with appendage induced vortices.

This work may be extended by considering alternate appendage geometries representative of bundle spacer and bearing pads. Variations in subchannel and/or gap geometry may also be considered.

Appendix A

Sensitivity and Convergence Study

Sensitivity assessments applying periodic boundary condition models were carried out in order to verify the full test section modelling parameters used for the mixing and appendage related simulations. The assessment included spatial and temporal convergence, as well as sensitivity to the turbulence model used (Spalart-Allmaras and k-ω) for the base case Reynolds number of 2690. The table below details the five simulations making up the complete suite of sensitivity cases. Details of the methodology and models applied are presented in Section 4.

Table A.1: Periodic boundary condition sensitivity case matrix

Run	Type	Appendage	Domain Length (mm)	Turbulence Model	Time Step (ms)	Nodes (× million)	Total Time Steps	Re	Comment
1	Periodic	No	300	S-A	1	2.2	100 000	2690	Base case
2	Periodic	No	550	S-A	1	4.0	100 000	2690	Domain length sensitivity
3	Periodic	No	300	S-A	1	6.0	100 000	2690	Spatial convergence
4	Periodic	No	300	S-A	0.5	2.2	200 000	2690	Time step convergence
5	Periodic	No	300	k-ω	1	2.2	100 000	2690	Turbulence model sensitivity

A.1 Base case

Figures A.1 through A.4 show respectively the instantaneous crossflow velocity contours through the gap mid-plane, crossflow frequency spectra at the gap center, the time averaged streamwise velocity profile through the gap mid-plane and the time averaged streamwise velocity contours for the base case simulation.

The instantaneous crossflow velocity contour through the gap (Figure A.1) represents a snapshot of the periodic results. The colour and shade of the zones indicates crossflow velocity direction and intensity according to the legend provided. The absolute value of peak crossflow velocities reported by Mahmood [2] and Lexmond et al. [3] are typically in the range of 0.01 m/s to 0.03 m/s with infrequent peaks exceeding 0.03 m/s. This agrees well with the periodic results in Figure A.1.

Alternating crossflow zones through the gap are clearly present in Figure A.1. Three macroscopic structures exist in the solution domain. This is one structure less than the anticipated four structures (see Section 4). The structures are not of equal length. This lack of structure length uniformity has been observed in a similar periodic boundary condition study with an identical geometry [61]. Derksen [61] identified one structure in the solution domain to be twice the length of the remaining structures. He concluded that this was not a lack of statistical convergence but rather a reflection of the flow attempting to conform to a structure size different than the domain length (L) divided by an integer number. Fewer structures (3 versus 4) imply an average structure length 33% longer than experimentally observed. A full quantitative comparison of structure length and other experimentally measured parameters against the CFD results is presented for the full test section simulations detailed in Section 5 where the results are not constrained in this manner.

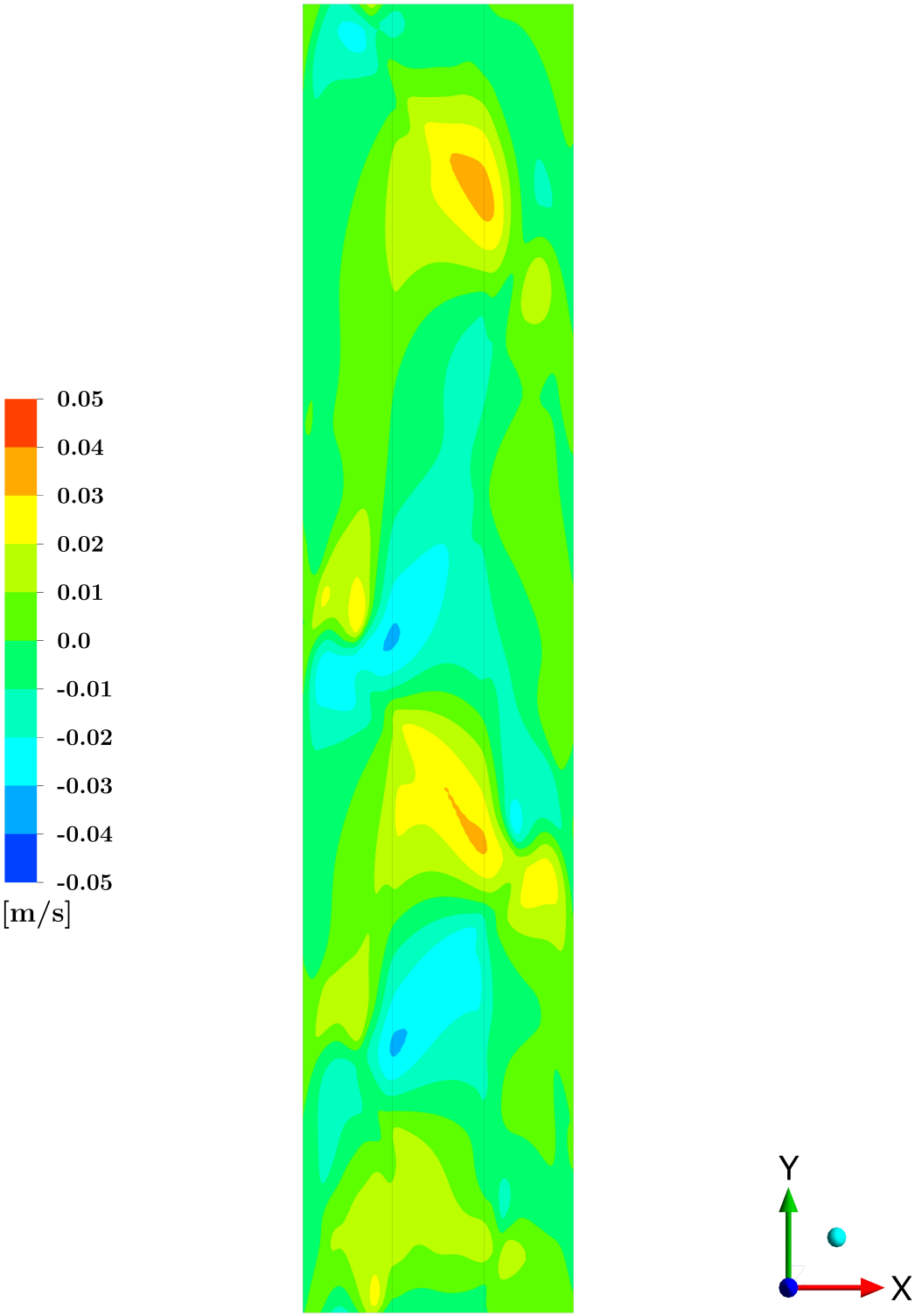

Figure A.1: Instantaneous crossflow velocity contour plot for base case.

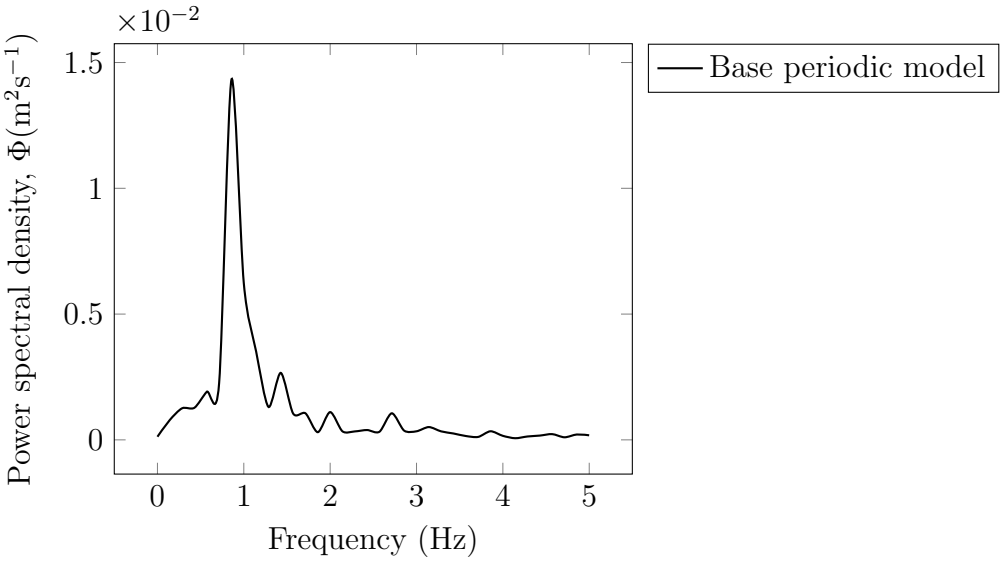

Figure A.2: Frequency spectrum of crossflow (u) velocities at gap center for base case.

The frequency spectra of crossflow velocity at the gap center and midplane were obtained by implementing an FFT script in MATLAB. The base case periodic CFD results show a peak crossflow frequency slightly below 1 Hz (Figure A.2). Lexmond et al. [3] reports a measured crossflow velocity for an identical geometry and inlet conditions that varies periodically with an average frequency of 1.1 Hz. A structure length 33% longer than experimentally observed translates to a crossflow frequency approximately 75% of the observed value (i.e., 0.75 $\times$ 1.1=0.825 Hz) assuming no significant change in structure velocity. This agrees reasonably well with the base case results. More detailed comparisons of crossflow velocity and frequency are presented for the full test section results in Section 5.

The time-averaged axial velocity profile through the gap midplane for the base case is shown in Figure A.3. The results from two experimental studies with identical geometry and flow conditions ([2] and [3]) are also shown for comparison. Reasonable agreement is obtained between the base case periodic results and the experimental

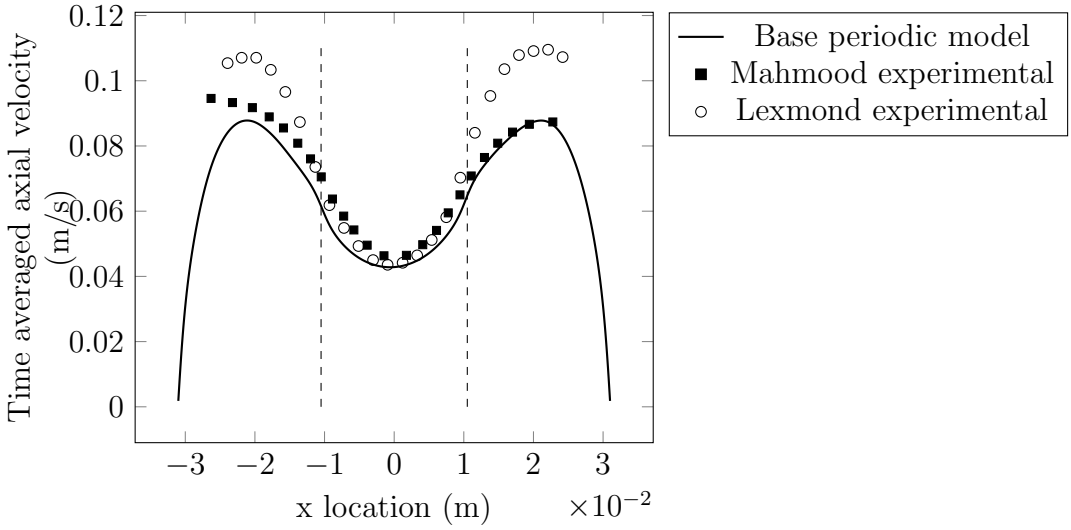

Figure A.3: Time averaged axial velocity profile through the gap mid-plane for base case. Dashed line shows gap edge location.

measurements, particularly those of Mahmood [2].

Figure A.4 shows the time averaged streamwise velocity contours from the base case simulation. Although there are no corresponding experimental measurements for this parameter, it is assessed in the context of the various sensitivities to help ensure a converged set of modelling and simulation parameters.

A.2 Domain length dependence

For this assessment, the domain length is increased from 300 mm to 550 mm. The mesh details for this model are identical to the base case model only extended an additional 250 mm. The instantaneous crossflow velocity contour through the gap midplane for the domain length sensitivity case is shown in Figure A.5. The contours are qualitatively similar to those for the base case (Figure A.1). Again, the absolute value of peak crossflow velocities are generally in the range of 0.01 m/s to 0.03 m/s,

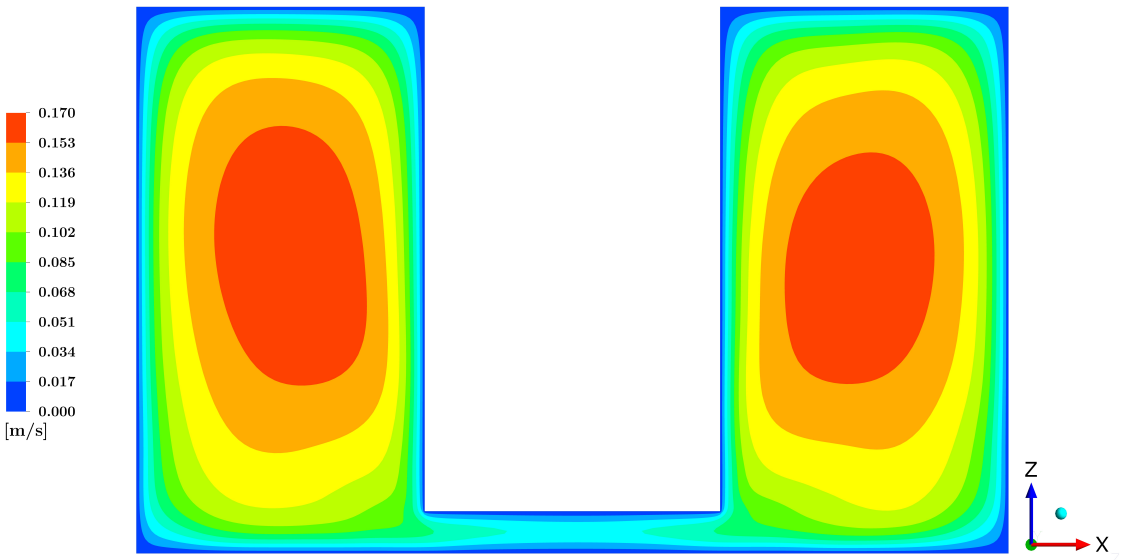

Figure A.4: Time averaged axial velocity contour plot for base case.

agreeing well with the experimental results from Mahmood [2] and Lexmond et al. [3].

Alternating crossflow zones through the gap are again clearly present in Figure A.5. The number of structures increased from three to five, consistent with the 80 percent increase in domain length. As in the base case, this is approximately 75% of the anticipated seven structures.

The frequency spectra of crossflow velocity at the gap center and midplane for the domain length sensitivity case is shown in Figure A.6. The results show a peak crossflow frequency slightly below 1 Hz consistent with the base case simulation.

The time-averaged axial velocity profile through the gap midplane for the domain length sensitivity case is shown in Figure A.7 along with the results from Mahmood [2] and Lexmond et al. [3]. The simulation results compare well with the experiments and are in very good agreement with the base case results.

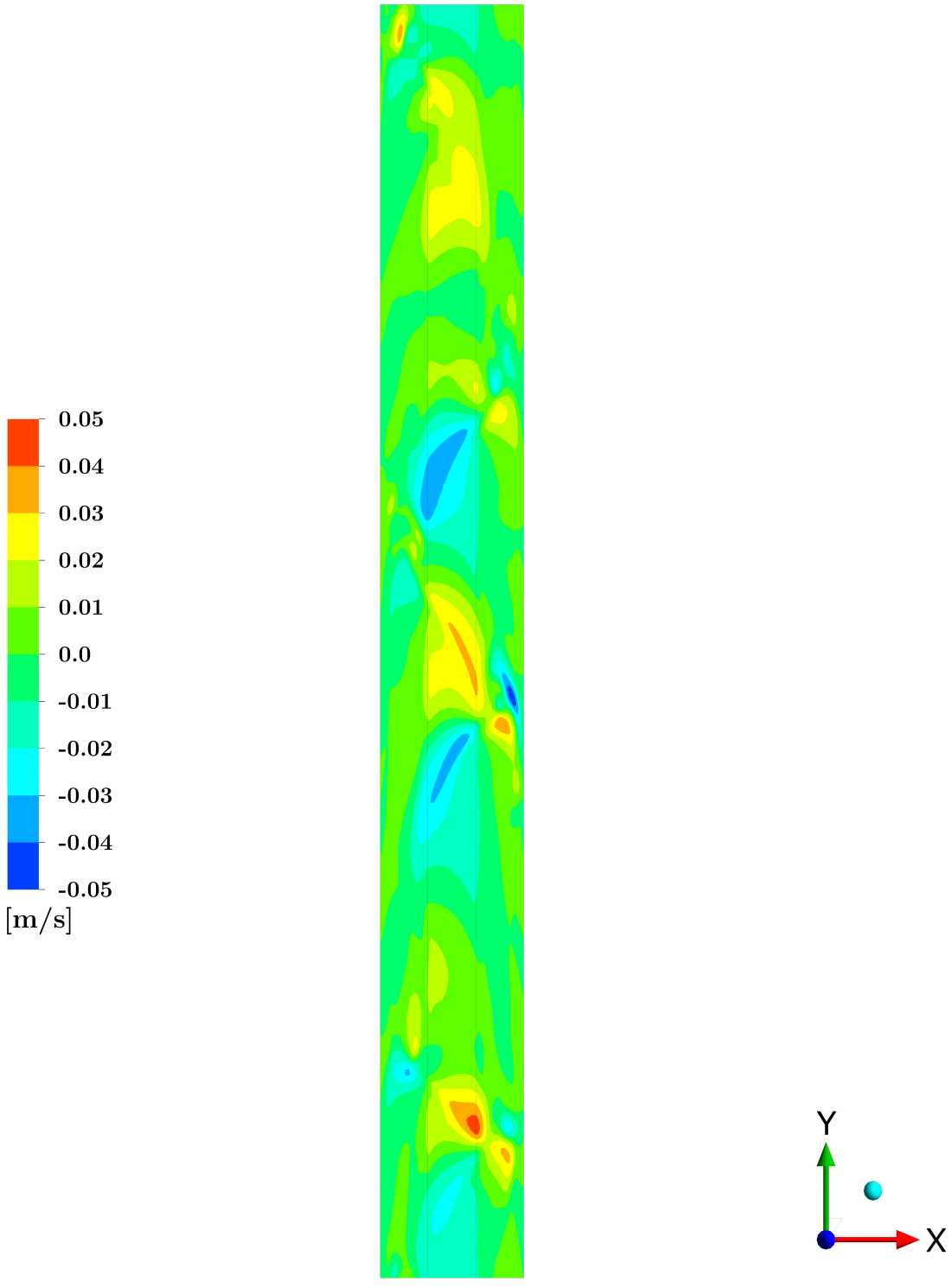

Figure A.5: Instantaneous crossflow velocity contour plot for domain length sensitivity case.

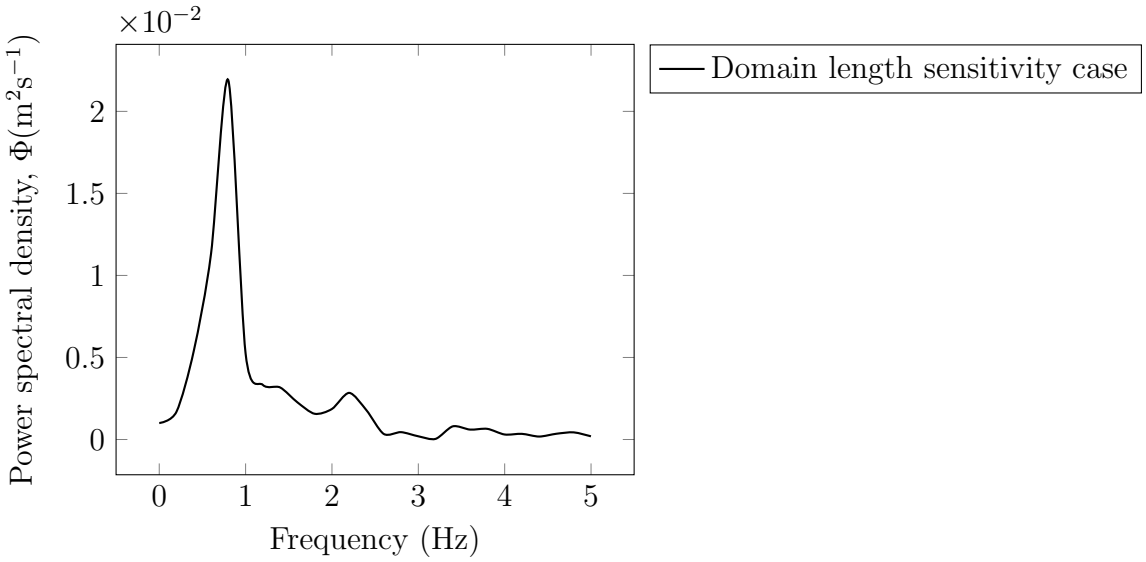

Figure A.6: Frequency spectrum of crossflow (u) velocities at gap center for domain length dependence case.

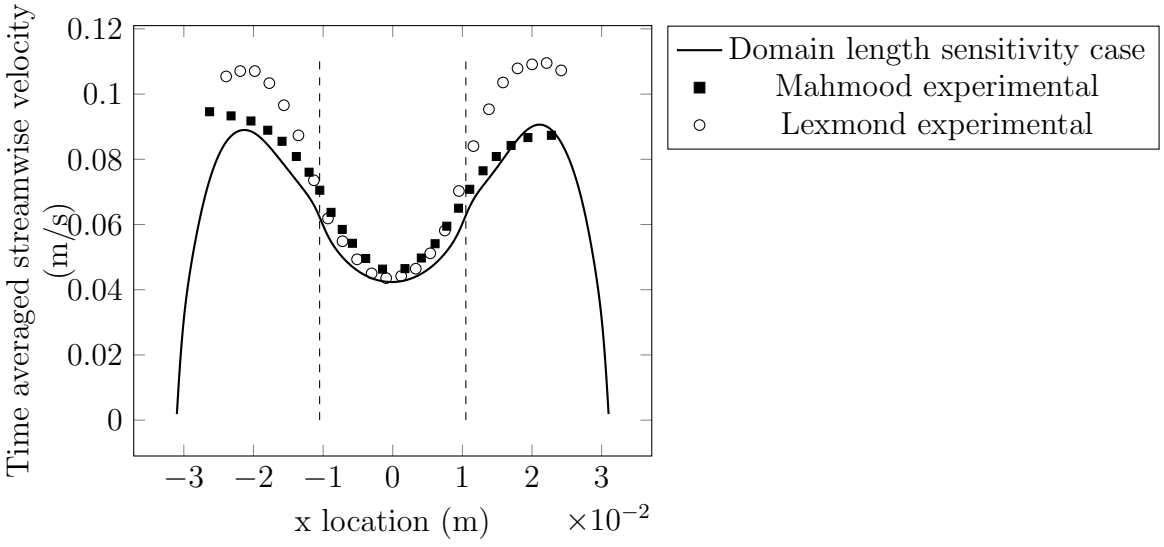

Figure A.7: Time averaged axial velocity profile through the gap mid-plane for domain length dependence case. Dashed line shows gap edge location.

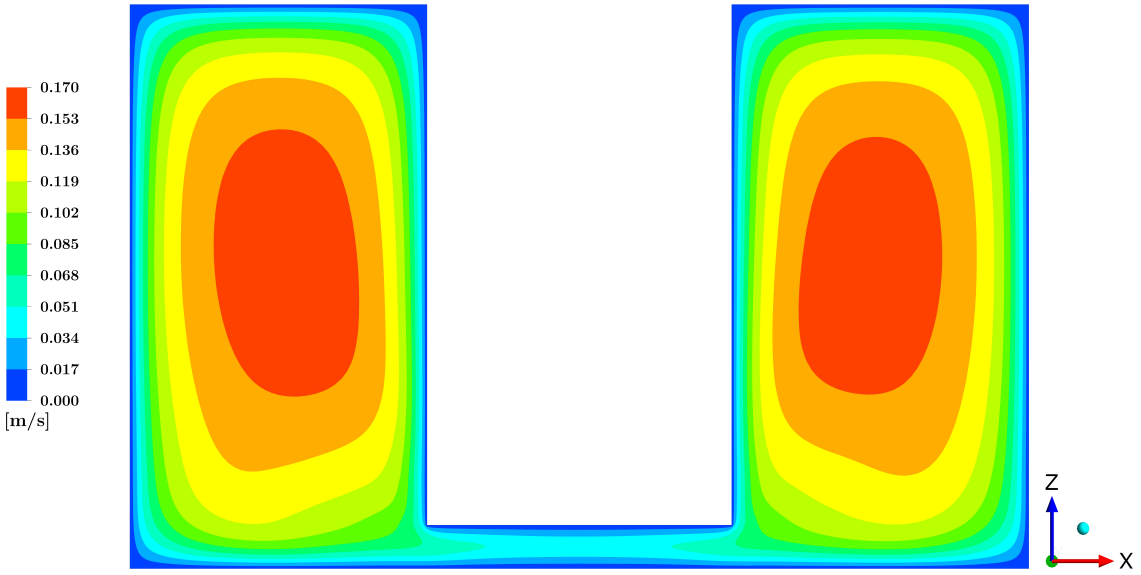

Figure A.8: Time averaged axial velocity contour plot for domain length sensitivity case.

Figure A.8 shows the time averaged streamwise velocity contours from the domain length sensitivity case. As noted earlier, there are no corresponding experimental measurements for this parameter but comparison against the base case results (Figure A.4) show very good agreement.

As there is no demonstrated improvement in agreement between experimental and numerical results for the domain length sensitivity case, the 300 mm domain is considered adequate for the balance of the sensitivity cases.

A.3 Mesh sensitivity

To assess grid independence for the periodic test section, grids M_1 and M_2 were generated. A 300 mm domain length periodic model was generated to assess spatial convergence. This model (M_2) had identical geometry compared to the base case

model but was discretized with a significantly finer mesh (approximately 6.0×10^6 versus 2.2×10^6 nodes) as discussed in Section 4.

Figure A.9 shows the instantaneous crossflow velocity contour through the gap midplane for the spatial convergence sensitivity case. The contours are again qualitatively very similar to those for the base case (Figure A.1). Peak crossflow velocities agree well with the experimental results from Mahmood [2] and Lexmond et al.[3] and are unchanged from the base case results. Both models develop three flow structures in the solution domain.

Figure A.10 shows the frequency spectra of crossflow velocity at the gap center and midplane for the spatial convergence case. Again, consistent with the base case simulation, the results show a peak crossflow frequency slightly below 1 Hz.

The spatial convergence sensitivity results for time-averaged axial velocity profile through the gap midplane are shown in Figure A.11. The numerical results compare well with the experimental results from Mahmood [2] and Lexmond et al. [3] and are in very good agreement with the base case.

The time averaged streamwise velocity contours from the spatial convergence case is shown in Figure A.12. Comparison against the base case results (Figure A.4) show very good agreement.

There is no notable improvement in agreement between experimental and numerical results for the spatial convergence sensitivity case and the results agree very well with those from the base case. As such, the base model nodalization scheme (2.2×10^6 nodes) is assessed to be acceptable for the domain and is used for the remaining sensitivity cases and the full test section model.

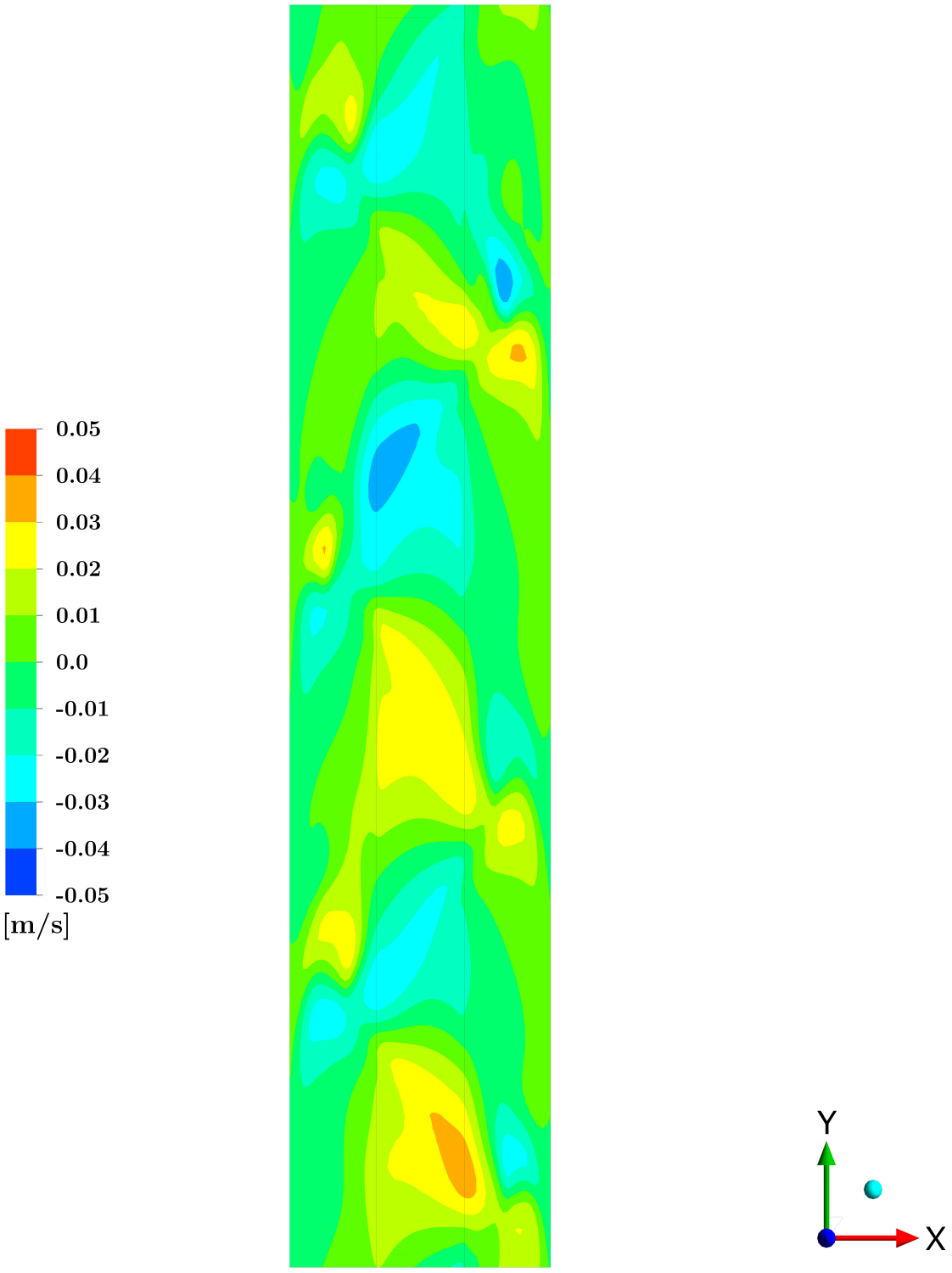

Figure A.9: Instantaneous crossflow velocity contour plot for grid independence sensitivity.

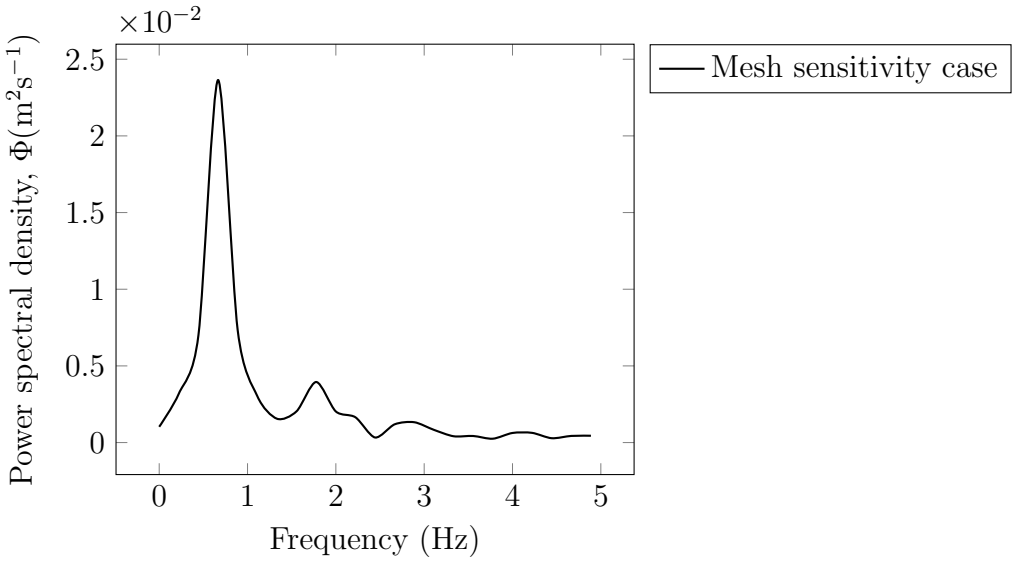

Figure A.10: Frequency spectrum of crossflow (u) velocities at gap center for mesh sensitivity (M_2) case.

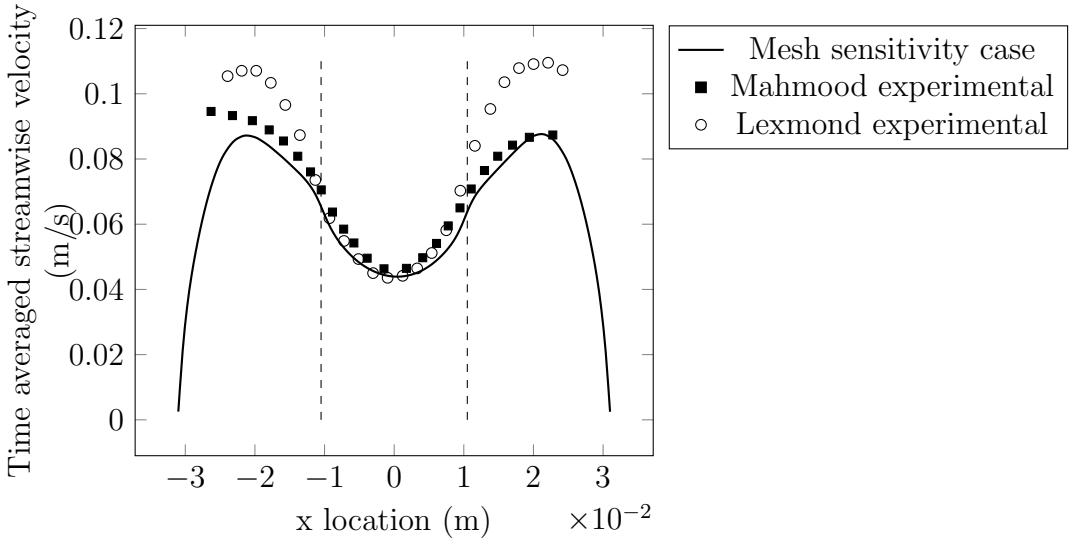

Figure A.11: Time averaged axial velocity profile through the gap mid-plane for grid independence sensitivity case. Dashed line shows gap edge location.

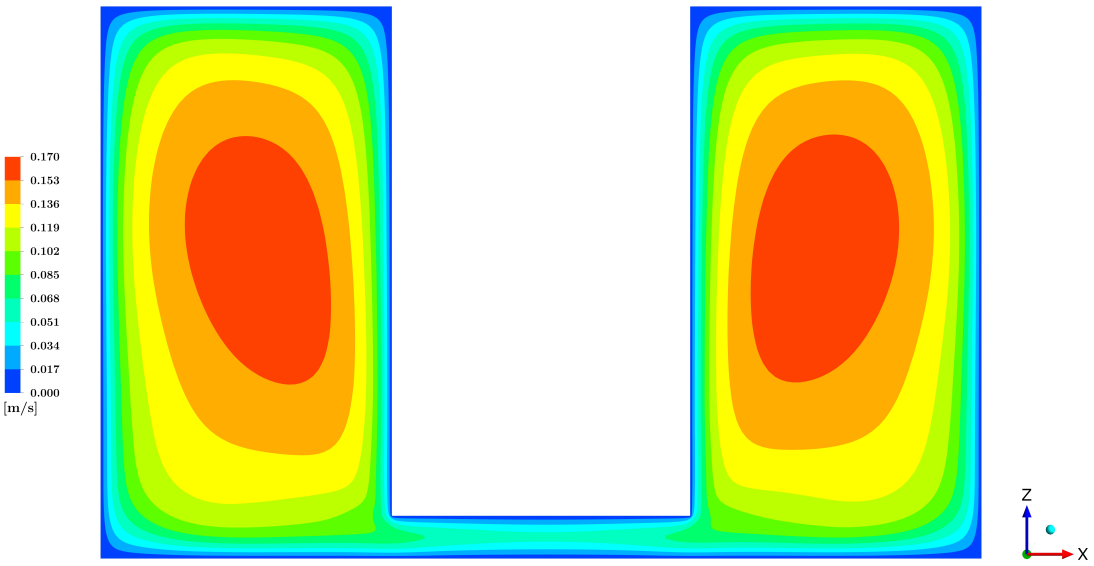

Figure A.12: Time averaged axial velocity contour plot for grid independence sensitivity case.

A.4 Time step independence

The temporal convergence assessment is carried out with model geometry, discretization, initial and boundary conditions identical to the base case simulation. The only change is that the fixed time step is reduced from 1 ms to 0.5 ms.

The instantaneous crossflow velocity contour through the gap midplane for this case (Figure A.13) is qualitatively very similar to the base case results (Figure A.1). Peak crossflow velocities agree well with the experimental results from Mahmood [2] and Lexmond et al. [3] and the base case results. Both the temporal convergence and base case models develop three flow structures in the solution domain.

The frequency spectra of crossflow velocity at the gap center and midplane (Figure A.14) for the temporal convergence case are consistent with the base case simulation having a peak crossflow frequency slightly below 1 Hz.

The time-averaged axial velocity profile through the gap midplane is shown in Figure A.15 for the spatial convergence case. Once again, the results show reasonable agreement with the experimental results ([2] and [3]) and are essentially unaltered from the base case.

Figure A.16 shows the time averaged streamwise velocity contours from the temporal convergence case which again shows very good agreement with the base case results (Figure A.4).

As the level of agreement with experimental results is unaltered from the base case simulations, the base case time step of 1 ms is assessed to be acceptable for these simulations and is used for the remaining sensitivity cases and the full test section model.

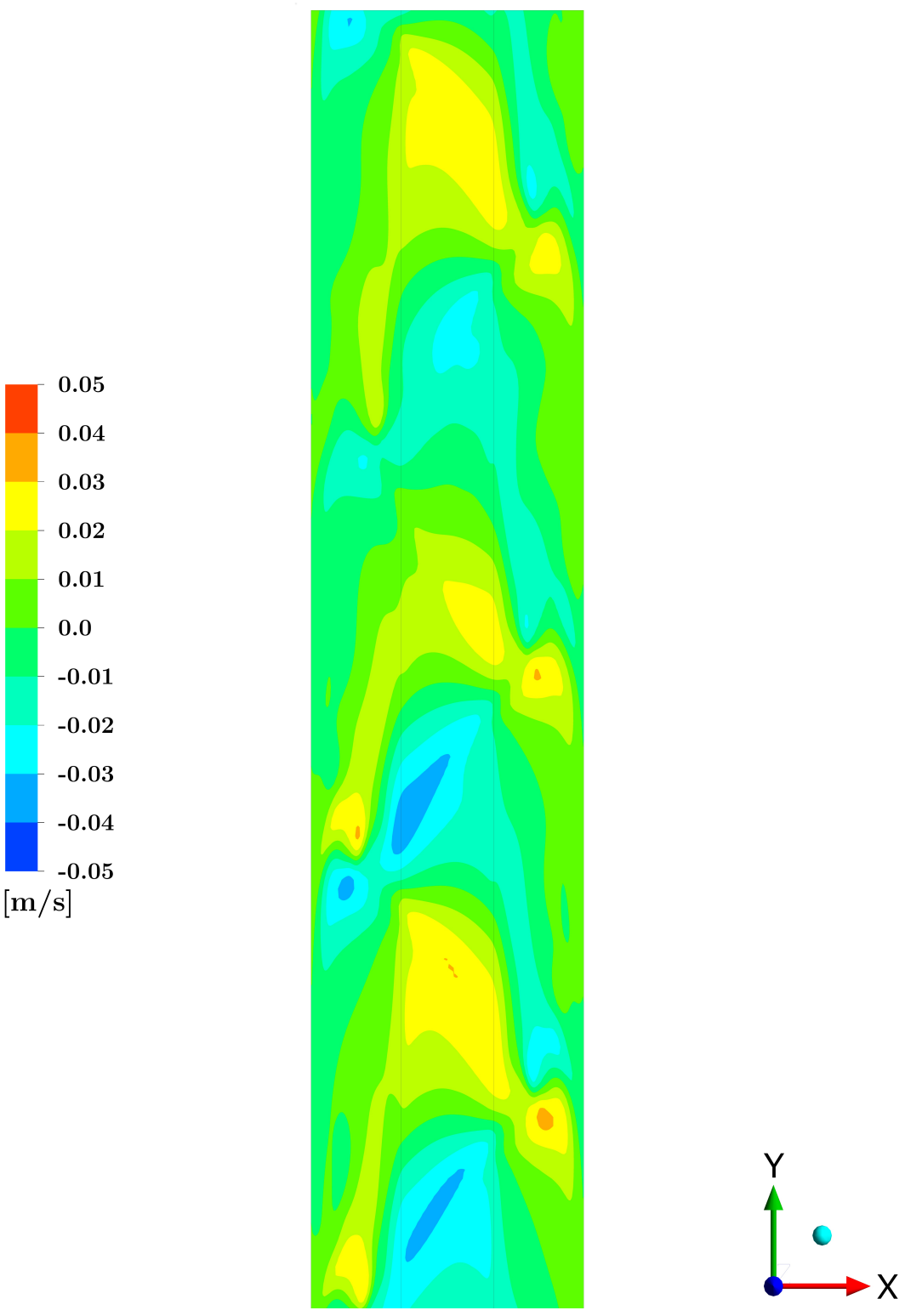

Figure A.13: Instantaneous crossflow velocity contour plot for time step sensitivity case.

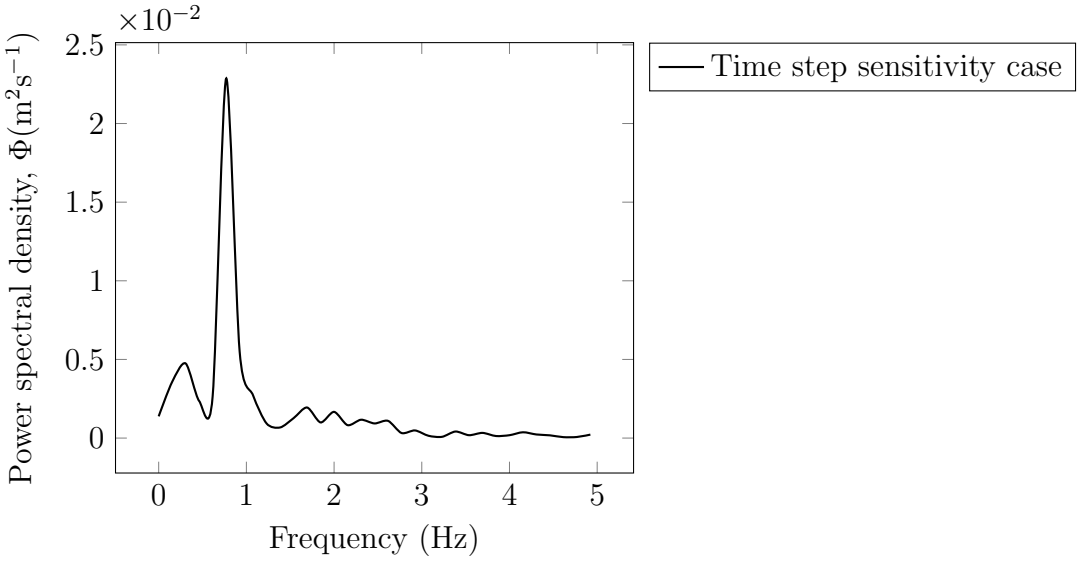

Figure A.14: Frequency spectrum of crossflow (u) velocities at gap center for time step sensitivity case.

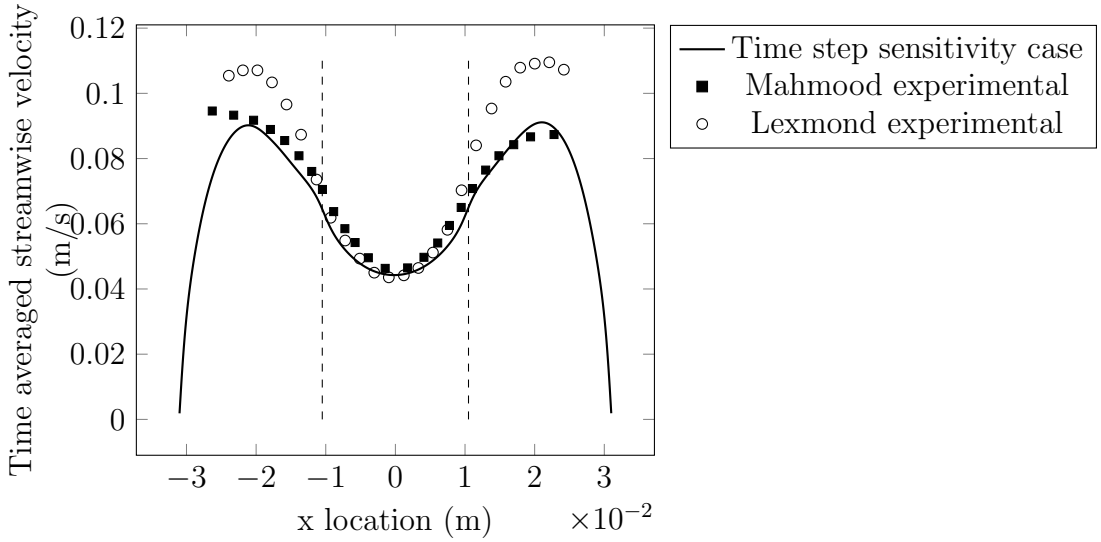

Figure A.15: Time averaged axial velocity profile through the gap mid-plane for time step sensitivity case. Dashed line shows gap edge location.

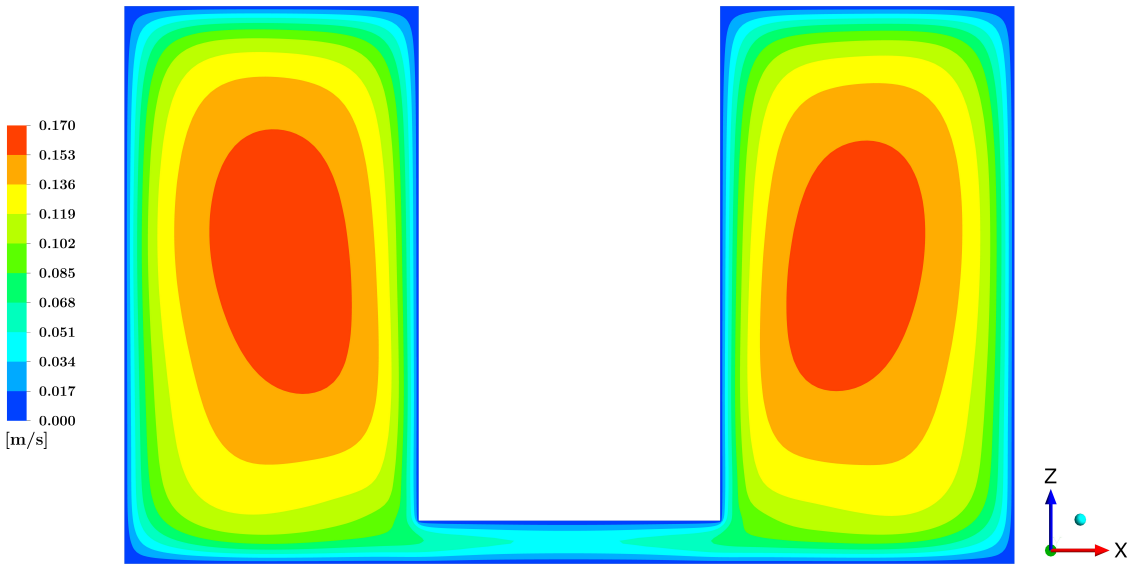

Figure A.16: Time averaged axial velocity contour plot for time step sensitivity case.

A.5 Turbulence model sensitivity

The sensitivity of the results to a higher order turbulence model (two-equation, k-ω) than the base case SA model (one-equation) is assessed. As discussed in Section 3, two-equation models provide a fuller description of the turbulence and tend to be more broadly applicable than one-equation models; however, this is achieved at the expense of computational efficiency. For the turbulence model sensitivity case, the only change from the base case simulations is that the k-ω turbulence model is applied by ANSYS CFX in the solution scheme.

Figure A.17 shows the instantaneous crossflow velocity contour through the gap midplane for the k-ω sensitivity case. The contours are again qualitatively very similar to those for the base case results shown in Figure A.1. Peak crossflow velocities agree well with the experimental results from Mahmood [2] and Lexmond et al. [3] and are similar to those from the base case simulation. Both models develop three flow

structures in the solution domain.

Figure A.18 shows the frequency spectra of crossflow velocity at the gap center and midplane for the turbulence model sensitivity case. Again, the results are consistent with the base case simulation showing a peak crossflow frequency slightly below 1 Hz.

Figure A.19 shows the time-averaged axial velocity profile through the gap midplane for the k-ω sensitivity case along with the experimental results from Mahmood [2] and Lexmond et al. [3]. The axial velocity through the gap region is slightly lower than both the experimental results and those from the base case. The axial velocity at the gap midplane through the subchannel region is slightly increased form the base case, still in reasonable agreement with the experimental results.

The time averaged streamwise velocity contours from the turbulence model sensitivity case is shown in Figure A.20. The highest velocity regions in the core of the subchannels are notably reduced in size compared to the base case results. As noted earlier, there are no direct experimental measurements for this parameter. The difference between the predictions cannot be used to support either of the two models. This parameter has been used in the sensitivity study primarily to demonstrate convergence in the application of the Spalart-Allmaras model.

The k-ω model demonstrates reasonable agreement with the experimental results as does the Spalart-Allmaras model. There is not a convincing case to be made to assume the computational expense of using the two-equation k-ω model for the full test section simulations.

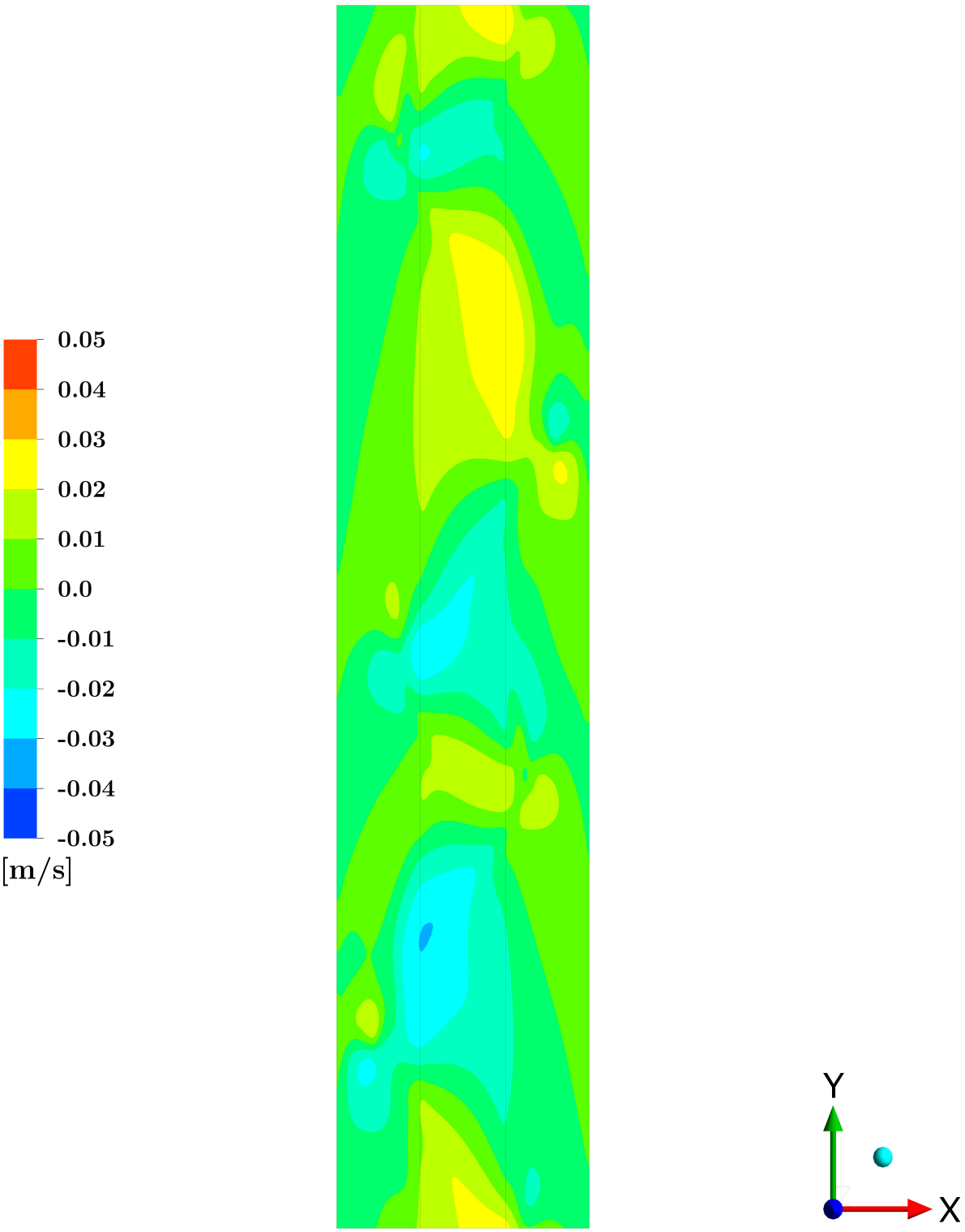

Figure A.17: Instantaneous crossflow velocity contour plot for k-omega turbulence model case.

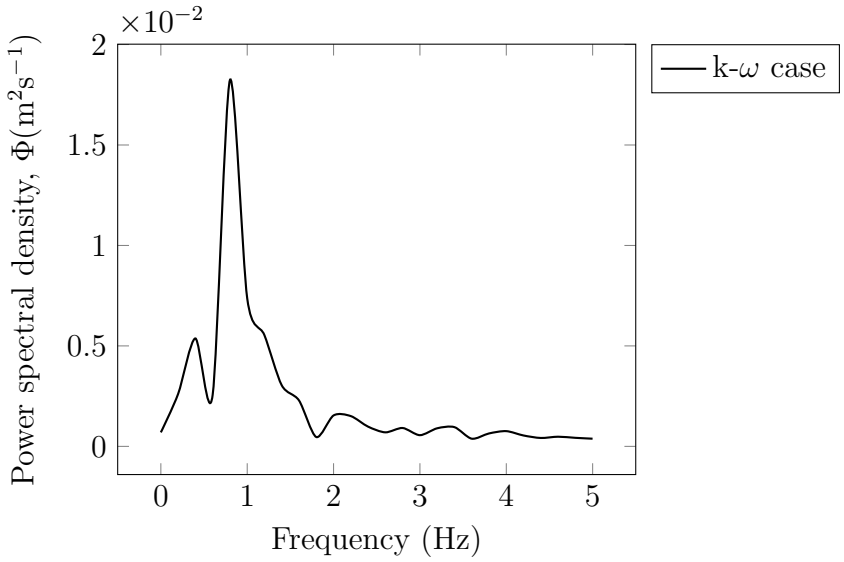

Figure A.18: Frequency spectrum of crossflow (u) velocities at gap center for k-omega case.

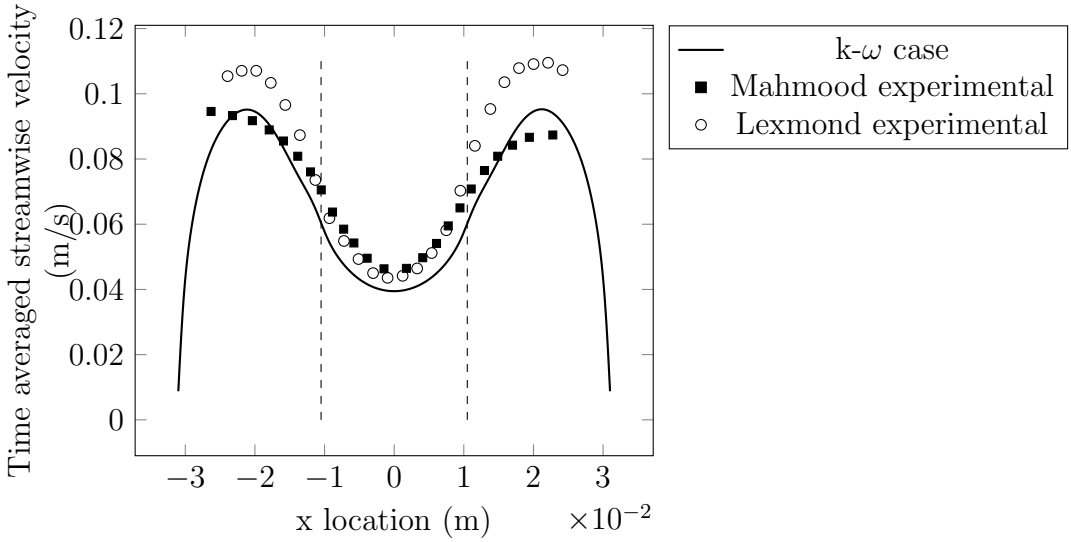

Figure A.19: Time averaged axial velocity profile through the gap mid-plane for k-omega case. Dashed line shows gap edge location.

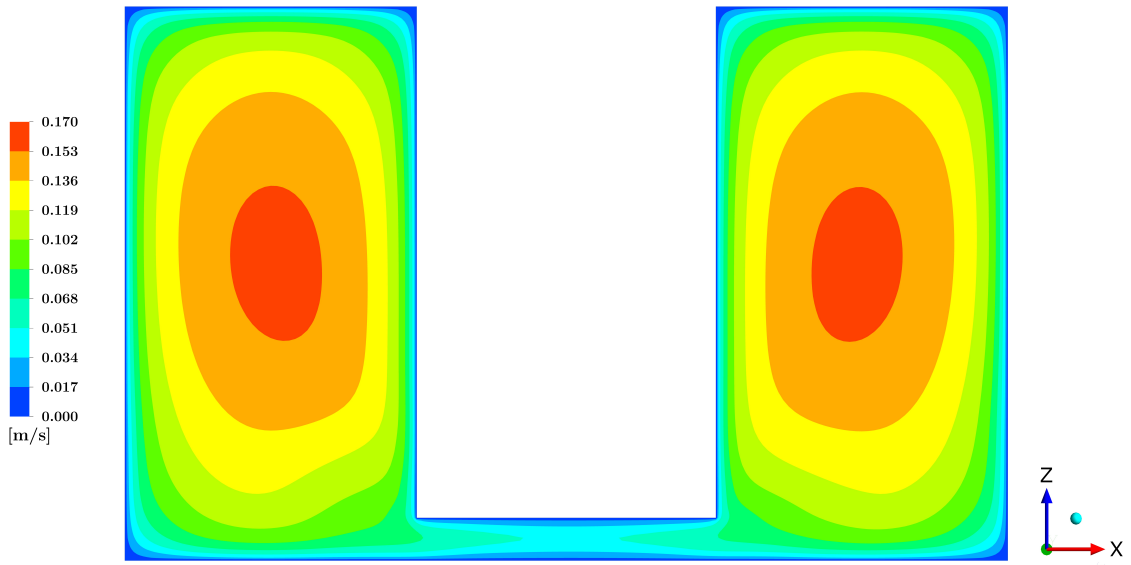

Figure A.20: Time averaged axial velocity contour plot for k-omega turbulence model

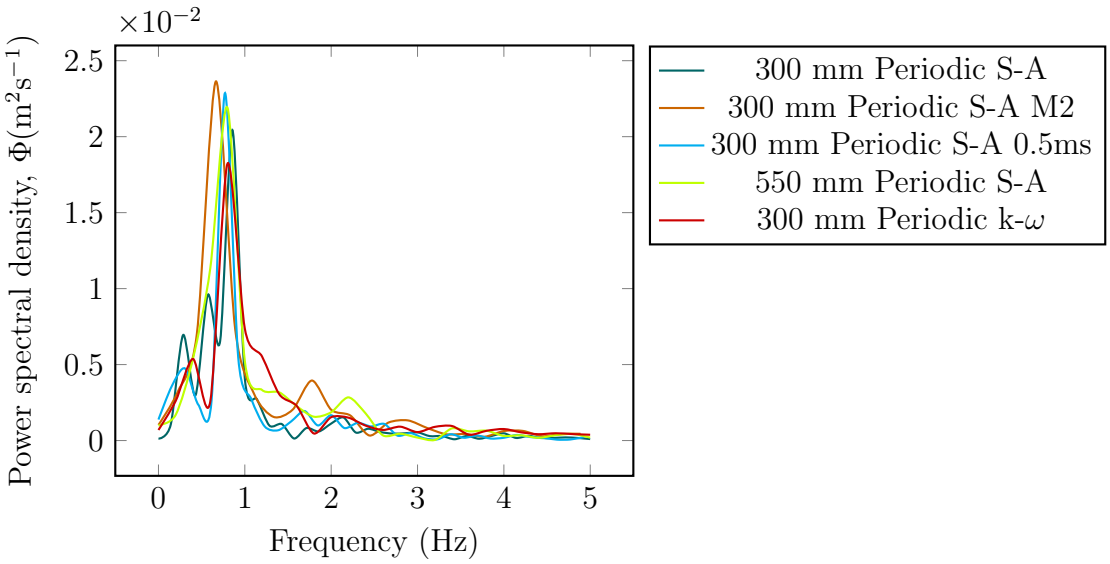

Figure A.21: Frequency spectra of crossflow (u) velocities at gap center for periodic cases

Bibliography

[1] Hao Zhang, F. Xavier Trias, Andrey Gorobets, Yuanqiang Tan, and Assensi Oliva. Direct numerical simulation of a fully developed turbulent square duct flow up to $re_\tau = 1200$. *International Journal of Heat and Fluid Flow*, 54:258 – 267, 2015.

[2] A. Mahmood. *Single-Phase Crossflow Mixing in a Vertical Tube Bundle Geometry - An Experimental Study.* PhD thesis, Delft University of Technology, 2011.

[3] Axel S. Lexmond, Rob F. Mudde, and Tim H.J.J. van der Hagen. Visualization of the vortex street and characterisation of the cross flow in the gap between two sub-channels. *The 11th International Topical Meeting on Nuclear Reactor Thermal-Hydraulics (NURETH-11)*, (122):1–20, 10 2005.

[4] CANDU. CANDU Reactor Power Plant Schematic. `https://cna.ca/wp-content/uploads/2016/01/reactor-v2-sized.jpg`, 2017. [Online; accessed 25-May-2017].

[5] UNENE. 37-element CANDU fuel bundle. `https://canteach.candu.org/`

Image%20Library1/Chapter17-image1.png, 2016. [Online; accessed 27-April-2017].

[6] D.S. Rowe and C.W. Angle. *Crossflow mixing between parallel flow channels during boiling. Part II. Measurement of flow and enthalpy in two parallel channels.* BNWL-371, Jan 1967.

[7] V.R. Skinner, A.R. Freeman, and H.G. Lyall. Gas mixing in rod clusters. *International Journal of Heat and Mass Transfer*, 12(3):265 – 278, 1969.

[8] L. Ingesson and B. Kjellstrm. On gas mixing in rod bundles. *International Journal of Heat and Mass Transfer*, 13(2):429 – 431, 1970.

[9] T. Van der Ros and M. Bogaardt. Mass and heat exchange between adjacent channels in liquid-cooled rod bundles. *Nuclear Engineering and Design*, 12(2):259 – 268, 1970.

[10] Hartmut Ramm, Klaus Johannsen, and Neil E Todreas. Single phase transport within bare rod arrays at laminar, transition and turbulent flow conditions. *Nuclear Engineering and Design*, 30(2):186 – 204, 1974.

[11] Hartmut Ramm and Klaus Johannsen. Hydrodynamics and heat transfer in regular arrays of circular tubes. *Int. Seminar on Recent Developments in Heat Exchangers, Trogir, Yugoslavia*, 1972.

[12] Fujio TACHIBANA, Akira OYAMA, Mamoru AKIYAMA, and Shunsuke KONDO. Measurement of heat transfer coefficients for axial air flow through eccentric annulus and seven-rod cluster. *Journal of Nuclear Science and Technology*, 6(4):207–214, 1969.

[13] D.S. Rowe, B.M. Johnson, and J.G. Knudsen. Implications concerning rod bundle crossflow mixing based on measurements of turbulent flow structure. *International Journal of Heat and Mass Transfer*, 17(3):407 – 419, 1974.

[14] A.C. Trupp and R.S. Azad. The structure of turbulent flow in triangular array rod bundles. *Nuclear Engineering and Design*, 32(1):47 – 84, 1975.

[15] A. M. M. Aly, A. C. Trupp, and A. D. Gerrard. Measurements and prediction of fully developed turbulent flow in an equilateral triangular duct. *Journal of Fluid Mechanics*, 85(1):5783, 1978.

[16] W.J. Seale. Turbulent diffusion of heat between connected flow passages part 1: Outline of problem and experimental investigation. *Nuclear Engineering and Design*, 54(2):183 – 195, 1979.

[17] W.J. Seale. Turbulent diffusion of heat between connected flow passages part 2: Predictions using the k-epsilon turbulence model. *Nuclear Engineering and Design*, 54(2):197 – 209, 1979.

[18] W. J. Seale. Measurements and predictions of fully developed turbulent flow in a simulated rod bundle. *Journal of Fluid Mechanics*, 123:399423, 1982.

[19] V Vonka. Measurement of secondary flow vortices in a rod bundle. *Nuclear Engineering and Design*, 106(2):191 – 207, 1988.

[20] V Vonka. Turbulent transports by secondary flow vortices in a rod bundle. *Nuclear Engineering and Design*, 106(2):209 – 220, 1988.

[21] J. D. Hooper and K. Rehme. Large-scale structural effects in developed turbulent

flow through closely-spaced rod arrays. *Journal of Fluid Mechanics*, 145:305337, 1984.

[22] K. Rehme. The structure of turbulent flow through rod bundles. *Nuclear Engineering and Design*, 99:141 – 154, 1987.

[23] Sergio Viosa Mller. On phenomena of turbulent flow through rod bundles. *Experimental Thermal and Fluid Science*, 4(1):25 – 35, 1991.

[24] Sergio Viosa Mller. Single-phase turbulent mixing in rod bundles. *Experimental Thermal and Fluid Science*, 5(1):26 – 33, 1992.

[25] X. Wu and A.C. Trupp. Experimental study on the unusual turbulence intensity distributions in rod-to-wall gap regions. *Experimental Thermal and Fluid Science*, 6(4):360 – 370, 1993.

[26] D. Chang and S. Tavoularis. Simulations of turbulence, heat transfer and mixing across narrow gaps between rod-bundle subchannels. *Nuclear Engineering and Design*, 238(1):109 – 123, 2008.

[27] L. Meyer and K. Rehme. Large-scale turbulence phenomena in compound rectangular channels. *Experimental Thermal and Fluid Science*, 1994.

[28] T Krauss and L Meyer. Experimental investigation of turbulent transport of momentum and energy in a heated rod bundle. *Nuclear Engineering and Design*, 180(3):185 – 206, 1998.

[29] M.S Guellouz and S Tavoularis. The structure of turbulent flow in a rectangular channel containing a cylindrical rod part 1: Reynolds-averaged measurements. *Experimental Thermal and Fluid Science*, 23(1):59 – 73, 2000.

[30] M.S. Guellouz and S. Tavoularis. The structure of turbulent flow in a rectangular channel containing a cylindrical rod part 2: phase-averaged measurements. *Experimental Thermal and Fluid Science*, 23(1):75 – 91, 2000.

[31] F. Baratto, S.C.C. Bailey, and S. Tavoularis. Measurements of frequencies and spatial correlations of coherent structures in rod bundle flows. *Nuclear Engineering and Design*, 236(17):1830 – 1837, 2006.

[32] Leonhard Meyer. From discovery to recognition of periodic large scale vortices in rod bundles as source of natural mixing between subchannelsa review. *Nuclear Engineering and Design*, 240(6):1575 – 1588, 2010.

[33] A.C. Trupp and A.M.M. Aly. Predicted secondary flows in triangular array rod bundles. *Journal of Fluids Engineering*, 101:354 – 362, 1979.

[34] C.W. Rapley and A.D. Gosman. The prediction of fully developed axial turbulent flow in rod bundles. *Nuclear Engineering and Design*, 97(3):313 – 325, 1986.

[35] Kye Bock Lee and Ho Cheol Jang. A numerical prediction on the turbulent flow in closely spaced bare rod arrays by a nonlinear k model. *Nuclear Engineering and Design*, 172(3):351 – 357, 1997.

[36] E. Baglietto and H. Ninokata. A turbulence model study for simulating flow inside tight lattice rod bundles. *Nuclear Engineering and Design*, 235(7):773 – 784, 2005.

[37] S. Tth and A. Aszdi. Cfd analysis of flow field in a triangular rod bundle. *Nuclear Engineering and Design*, 240(2):352 – 363, 2010.

[38] D. Chang and S. Tavoularis. Numerical simulation of turbulent flow in a 37-rod bundle. *Nuclear Engineering and Design*, 237(6):575 – 590, 2007.

[39] M Biemuller, Leonhard Meyer, and K Rehme. Large eddy simulation and measurement of the structure of turbulence in two rectangular channels connected by a gap, 1996.

[40] B.H. Ouma and S. Tavoularis. Turbulence structure in triangular subchannels of a reactor bundle model. *Nuclear Engineering and Design*, 128(3):271 – 287, 1991.

[41] B.H. Ouma and S. Tavoularis. Flow measurements in rod bundle subchannels with varying rod-wall proximity. *Nuclear Engineering and Design*, 131(2):193 – 208, 1991.

[42] E. Merzari, H. Ninokata, and E. Baglietto. Numerical simulation of flows in tight-lattice fuel bundles. *Nuclear Engineering and Design*, 238(7):1703 – 1719, 2008.

[43] F. Abbasian, S.D. Yu, and J. Cao. Experimental and numerical investigations of three-dimensional turbulent flow of water surrounding a candu simulation fuel bundle structure inside a channel. *Nuclear Engineering and Design*, 239(11):2224 – 2235, 2009.

[44] D. Home, G. Arvanitis, M.F. Lightstone, and M.S. Hamed. Simulation of flow pulsations in a twin rectangular sub-channel geometry using unsteady reynolds averaged navierstokes modelling. *Nuclear Engineering and Design*, 239(12):2964 – 2980, 2009.

[45] Maolong Liu and Yuki Ishiwatari. Unsteady numerical simulations of the single-phase turbulent mixing between two channels connected by a narrow gap. *Nuclear Engineering and Design*, 241(10):4194 – 4205, 2011.

[46] Michio Sadatomi, Akimaro Kawahara, and Yoshifusa Sato. Prediction of the single-phase turbulent mixing rate between two parallel subchannels using a subchannel geometry factor. *Nuclear Engineering and Design*, 162(2):245 – 256, 1996.

[47] Seong-Ho Hong, Jeong-Sik Seo, Jae-Ki Byun, Young Choi, and Jong-Keun Shin. Turbulent heat transfer characteristics in compound channels with gap. 25:2217–2225, 09 2011.

[48] B.H. Yan, H.Y. Gu, and L. Yu. Numerical simulation of the coherent structure and turbulent mixing in tight lattice. *Progress in Nuclear Energy*, 54(1):81 – 95, 2012.

[49] T. Krauss and L. Meyer. Characteristics of turbulent velocity and temperature in a wall channel of a heated rod bundle. *Experimental Thermal and Fluid Science*, 12(1):75 – 86, 1996.

[50] D.S. Rowe and C.C Chapman. Measurement of turbulent velocity, intensity and scale in rod bundle flow channels containing a grid spacer. *BNWL-1757*, 1973.

[51] Sarman Gencay, A Tapucu, N Troche, and M Merilo. Experimental study of the diversion crossflow caused by subchannel blockages: Part i: Experimental procedures and mass flow rates in the channels. part ii: Pressures in the channels

and the comparison of the cobra iii-c predictions with experimental data. *ASME J. Fluids Eng.*, 106:435–447, 1984.

[52] Sun Kyu Yang and M Chung. Turbulent flow through spacer grids in rod bundles. *ASME J. Fluids Eng.*, 120:786–791, 1998.

[53] Mary V. Holloway, Donald E. Beasley, and Michael E. Conner. Single-phase convective heat transfer in rod bundles. *Nuclear Engineering and Design*, 238(4):848 – 858, 2008.

[54] C.C. Liu, Y.M. Ferng, and C.K. Shih. Cfd evaluation of turbulence models for flow simulation of the fuel rod bundle with a spacer assembly. *Applied Thermal Engineering*, 40:389 – 396, 2012.

[55] M.V. Holloway, H.L. McClusky, Donald Beasley, and M.E. Conner. The effect of support grid features on local, single-phase heat transfer measurements in rod bundles. 2003:547–560, 01 2003.

[56] Mary V. Holloway, Timothy Conover, Heather L. McClusky, Donald Beasley, and Michael E. Conner. The effect of support grid design on azimuthal variation in heat transfer coefficient for rod bundles. 127, 06 2005.

[57] B. L. Smith, C.-H. Song, S.-K. Chang, J. R. Lee, and J. W. Kim. Report of the oecd/nea kaeri rod bundle cfd benchmark exercise. *Nuclear Energy Agency*, 2013.

[58] J Szymanski, Dong-il Chang, David Novog, K Podila, Joanne Bailey, Yanfei Rao, A Rashkovan, and S Tavoularis. Canadian participation in oecd/nea-kaeri rod bundle benchmark for cfd codes. *24th Nuclear Simulation Symposium*, 10 2012.

[59] Alex Rashkovan and D.R. Novog. R522.1a: International cfd benchmark problem. *McMaster University*, 2012.

[60] G. Arvanitis. Simulation of flow pulsations in gap geometries using unsteady reynolds averaged navier-stokes modelling. Master's thesis, McMaster University, 2008.

[61] J.J. Derksen. Simulations of lateral mixing in cross-channel flow. *Computers & Fluids*, pages 1058–1069, 1 2010.

[62] J. Mathieu and J. Scott. *An Introduction to Turbulent Flow*. Cambridge University Press, 2000.

[63] S.B. Pope. *Turbulent Flows*. Cambridge University Press, 2000.

[64] F.M. White. *Viscous Fluid Flow*. McGraw-Hill international editions: Mechanical engineering series. McGraw-Hill, 1991.

[65] D.C. Wilcox. *Turbulence Modeling for CFD*. DCW Industries, 2006.

[66] P.R. Spalart and S.R. Allmaras. A one-equation turbulence model for aerodynamic flows. *30^{th} Aerospace Sciences Meeting and Exhibit*, 1992.

[67] B.S. Baldwin and T.J. Barth. A one-equation turbulence transport model for high reynolds number wall-bounded flows. *NASA Technical Memorandum*, 1990.

[68] G.L. Mellor and H.J. Herring. Two methods of calculating turbulent boundary layer behaviour based on numerical solutions of the equations of motion. i: Mean velocity field method; ii: Mean turbulent field method. *Proceedings - Computation of Turbulent Boundary Layers*, 1968.

[69] H.K. Versteeg and W. Malalasekera. *An Introduction to Computational Fluid Dynamics: The Finite Volume Method*. Pearson Education Limited, 2007.

[70] D.C. Wilcox. Multiscale model for turbulent flows. *AIAA 24th Aerospace Sciences Meeting. American Institute of Aeronautics and Astronautics*, 26(122):1311–1320, 1988.

[71] Salim .M. Salim and S.C. Cheah. Wall y^+ strategy for dealing with wall-bounded turbulent flows. *Proceedings of the International MultiConference of Engineers and Computer Scientists*, pages 2165–2170, 3 2009.

[72] E. Naudascher and D. Rockwell. *Flow-Induced Vibrations: An Engineering Guide*. Dover Civil and Mechanical Engineering. Dover Publications, 2005.

[73] Asmund Huser and Sedat Biringen. Direct numerical simulation of turbulent flow in a square duct. *J. Fluid Mech.*, 257:65 – 95, 1993.

[74] L. C. Hoagland. *Fully developed turbulent flow in straight rectangular ducts : secondary flow, its cause and effect on the primary flow*. PhD thesis, Massachusetts Institute of Technology, 1962.